



TECHNISCHE
UNIVERSITÄT
MÜNCHEN



WALTHER - MEISSNER -
INSTITUT FÜR TIEF -
TEMPERATURFORSCHUNG



BAYERISCHE
AKADEMIE DER
WISSENSCHAFTEN

Quantum Process Tomography of a 3D Quantum Memory

Master's Thesis
Michael Renger

Supervisor: Prof. Dr. Rudolf Gross
Garching, October 16, 2018

Contents

1	Introduction	1
2	Theory	3
2.1	Superconducting qubits: the transmon qubit	3
2.2	Reconstruction of a quantum state	8
2.2.1	Coupling of qubit and cavity	8
2.2.2	Qubit control	10
2.2.3	Quantum state tomography	12
2.3	Reconstruction of quantum processes	15
2.3.1	Quantum processes	15
2.3.2	Quantum process tomography	19
2.4	Characterizing QST and QPT	22
2.4.1	Distance measures	23
2.4.2	Distance limits	25
2.4.3	Loyalty	26
2.5	Quantum master equations	27
2.6	Quantum memory theory	28
3	Setup and experimental techniques	31
3.1	Sample description	31
3.2	Measurement setup	32
3.2.1	Cryogenic setup	32
3.2.2	Room temperature setup	32
3.2.3	Pulse shaping	34
3.3	Qubit characterization	36
3.4	Memory characterization	41
4	Benchmarking a 3D quantum memory	45
4.1	Single qubit benchmarking for QST	45
4.2	QPT for single qubit operations	51
4.3	QST for the quantum memory	58
4.4	QPT for the quantum memory	62
4.5	Time-resolved tomography of the memory	67
5	Summary and outlook	75

Appendices	77
A QST and QPT	77
A.1 Density matrix for QST	77
A.2 Maximum likelihood estimation for QST	78
A.3 Basis change for QPT	78
A.4 Maximum likelihood estimation for QPT	79
B Distance measures	81
B.1 Diamond norm for the identity process	81
B.2 Quantum memory fidelity	82
C RO phase fluctuations	85
C.1 Thermal photons in the cavity	85
C.2 Thermal expansion of the cavity	86
C.3 Thermal radiation by the antennas	87
D Master equation	89
Bibliography	91
Acknowledgment	103

List of Figures

2.1	Transmon circuit	4
2.2	Transmon energy dispersion	4
2.3	Classical bit	5
2.4	Bloch sphere	6
2.5	Circuit QED setup	8
2.6	Transmon design	9
2.7	Jaynes-Cummings energy scheme	10
2.8	Rabi oscillations	11
2.9	Illustration of MLE	13
2.10	Single qubit QST	14
2.11	Rotation about the y -axis: Bloch sphere	16
2.12	Energy relaxation: Bloch sphere	17
2.13	Dephasing: Bloch sphere	18
2.14	Depolarization: Bloch sphere	18
2.15	Single qubit QPT	22
2.16	Trace distance: Bloch sphere	24
2.17	FEM simulation for the cavity modes	29
2.18	Quantum memory protocol	29
3.1	Technical drawing of the cavity	32
3.2	Cryostat and cryogenic electronics	33
3.3	Schematic illustration of the time domain setup	34
3.4	Pulse shaping and pulse area	35
3.5	Transmission measurement for the cavity	37
3.6	Dispersive shift	37
3.7	Measured Rabi oscillations	38
3.8	π -pulse length depending on the phase angle	39
3.9	Measured T_1 decay of the qubit	39
3.10	Ramsey oscillations of the qubit population	40
3.11	BSB transition and AC Stark shift	41
3.12	Realized pulse pattern of the memory protocol	42
3.13	T_1 decay for the memory	42
3.14	Ramsey experiment for the memory	43
4.1	QST for single qubit states	48
4.2	Benchmarking of QST for different amount of averages	49

4.3	Benchmarking of the phase sensitivity of QST	50
4.4	QPT for the identity, a π pulse about the y -axis and a $\pi/2$ -pulse about the y -axis	53
4.5	QPT for a $\pi/2$ -pulse about the x -axis and the CDP	54
4.6	Discrete Rabi oscillations for the RO phase using Gaussian pulses	58
4.7	Reconstruction of $ g\rangle$ and $ e\rangle$ -state after retrieval from the memory	59
4.8	Reconstruction of $ +\rangle$, $ -\rangle$, $ o\rangle$ and $ \square\rangle$ after retrieval from the memory	60
4.9	QST for the BSB transition	61
4.10	QPT for the memory protocol	62
4.11	Categories of measurement results for the χ -matrix of the memory protocol	65
4.12	QPT for a rotation by $\pi/2$ about the x -axis followed by the memory process	66
4.13	Schematic illustration of the simulation of the memory protocol	68
4.14	Exponential decay of the measured fidelity compared with a master equation simulation	69
4.15	Comparison of the simulated and the measured process matrix for $t_s = 0$	70
4.16	Simulated and reconstructed process matrix for $t_s = 5.12 \mu s$	71
4.17	Simulated distance measures depending on the time t_s	72
4.18	Fidelity of the reconstructed process, depending on the time t_d between the memory protocol and the QST pulses	73

List of Tables

2.1	Theoretical distance limits for QST and QPT	26
4.1	Distance measures for QST benchmarking	47
4.2	Experimental verification of the distance limits derived in Sec. 2.4.2	47
4.3	Distance measures for QPT benchmarking	52
4.4	Distance limits for QPT	55
4.5	Distance measures for $ g\rangle$, $ e\rangle$, $ +\rangle$, $ -\rangle$, $ \circ\rangle$ and $ \square\rangle$ after storage and retrieval . .	59
4.6	Distance measures for the reconstructed memory process	63
4.7	Distance measures for a rotation by $\pi/2$ about the x -axis followed by the memory protocol.	66
4.8	Distance measures for the comparison of the reconstructed and the simulated process matrix for $t_s = 5.12 \mu s$	71
4.9	Distance limits for the comparison of the ideal memory process and T_1 decay for timescales $t \rightarrow \infty$	72
4.10	Distance measures for the simulated process matrices after $t_s = 25 \mu s$ and $t_d = 25 \mu s$ with respect to the ideal memory process.	72
4.11	Distance measures for the comparison of the reconstructed and the ideal process matrix for $t_d = 4.096 \mu s$	73

Chapter 1

Introduction

The reconstruction of 3D-objects is an important but challenging issue [1], and technologies that solve this task are highly relevant for computer graphics [2], artificial intelligence [3] and virtual reality [4], but also for quality tests in material science [5] and for forensics [6]. One of the most famous applications is probably medical imaging [7], which gives access to 3D-images of the interior of the body, and hence is a crucial tool, e.g. for cancer diagnosis and treatment [8]. In modern applications, these images are obtained by computer aided tomography (CT scan) [9], a procedure that enables us to reconstruct a 3D-object by performing projective measurements.

In quantum information processing (QIP), it is of utmost importance to be able to characterize quantum systems [10], and we exploit the fact that the physics of a quantum two-level-system (TLS) can be described and understood using an auxiliary 3D geometric picture [11]. The quantum state of the system is then uniquely described by a 3D vector, and we obtain full access to the quantum system if we are able to reconstruct this quantity [12]. Since this access is realized, in analogy to the CT scan, by performing projective measurements, the corresponding procedure is called quantum state tomography (QST) [13]. In principle, this technique also succeeds for higher dimensional quantum systems, despite we no longer have an intuitive geometric interpretation [12]. Furthermore, we can generalize this technique and use projective measurements to completely characterize quantum processes on arbitrary quantum systems [14]. This method of reconstructing quantum operations is called quantum process tomography (QPT) [12].

The reconstruction of quantum states and processes has become especially important in recent years, because QIP has gained significant public attention and offers a broad spectrum of applications [15]. Quantum computing, which enables fast prime factorization [16] as well as solving complex optimization problems [17], is just one of them. One reason for this high interest is the fact that there has been significant progress in hardware architectures that allow for the realization of the theoretical concepts of QIP, and which may finally enable us to build scalable QIP devices [18]. One of the most promising platforms are superconducting quantum circuits [19, 20] that are coupled to the electrical modes of a microwave resonator. Superconducting circuits give the opportunity to build artificial atoms with engineered coupling strengths [21].

They replace the natural atoms used in cavity quantum electrodynamics (QED) [22, 23]. In this field, which is called circuit QED [24], a large variety of experiments has been performed with coplanar 2D waveguide resonators, reaching from the detection of topological phase transitions [25] to models for photosynthesis processes [26]. In addition, there are multiple approaches using 3D cavity resonators [27] with enhanced photon lifetimes up to 0.1 ms [28, 29]. The latter allow us to build scalable architectures [30] and give access to various different physical phenomena [31–33].

One crucial step necessary for realizing QIP devices is an adequate coherence time of the quantum system, i.e., we have to be able to store quantum states sufficiently long [34]. In our experiment, we propose and build an architecture that can serve as a quantum memory [35]. Our setup consists of a superconducting qubit placed in a 3D cavity resonator, and we exploit the enhanced coherence time of the cavity to store the qubit state as a Fock state in one of its long-lived electrical modes. This concept has already been realized using shorter-lived 2D resonators [36]. Within this thesis, we use QST and QPT to characterize the system and the quality of the complete memory process. Besides QPT, there are other well known procedures, such as randomized benchmarking [37, 38].

The thesis is structured as follows. First of all, we introduce the concept of the transmon qubit and discuss the physics of a driven two-level system (TLS) in Chapter 2. We develop the theory for QST and QPT and describe how we can compare quantum states and quantum processes, respectively. After that, we deal with the theoretical ideas behind our memory experiment and understand the pulse protocol that is necessary for storage and retrieval of a quantum state. Chapter 3 deals with the realization of the quantum memory experiment. We explain the sample as well as the cryogenic setup. In addition, we discuss the microwave electronics at room temperature and explain the qubit control in detail. We show the results from qubit characterization measurements. Subsequently, we characterize the actual quantum memory. In Chapter 4, we implement the pulse schemes necessary for QST and QPT and test the resulting protocols by reconstructing known single qubit states and processes. We then use QST to reconstruct stored states after retrieval. We use QPT to characterize the quantum memory process and investigate the decoherence processes induced by the memory protocol. We perform time-resolved QPT and compare the outcome with a master equation simulation of the memory process. A summary of the main results, as well as an outlook, is given in Chapter 5.

Chapter 2

Theory

2.1 Superconducting qubits: the transmon qubit

A quantum bit (qubit) forms the elementary building block for most quantum computing architectures [39] and can be regarded as the quantum mechanical generalization of the classical bit [12]. It represents the basic logic module in digital electronics and for classical information processing [40]. From a physical point of view, every TLS can act as a qubit, and the physics of a general TLS is explained in detail within this section and in Sec. 2.4.

We find a large variety of physical realizations of a qubit, and many of them are directly provided by nature: ions that can be trapped in optical lattices [41, 42], but also, spin 1/2 fermions [11] such as electrons, NV centers in diamond [43, 44] or the polarization of photons [45].

Using artificial atoms as qubits has the big advantage that many of their properties, such as the coupling strength or the energy splitting, are not fixed by nature. Instead, they can be engineered in a desired manner. There is a large amount of artificial atom implementations, such as quantum dots [46], and also superconducting circuits [24, 47, 48]. The crucial element of all superconducting qubits is the Josephson junction, as depicted in Fig. 2.1. A Josephson junction consists of two superconductors separated by a thin insulating barrier [49], which allows the tunneling of Cooper pairs [50]. The physics of this element is governed by the two Josephson equations [51], which inter alia imply that a Josephson junction can be regarded as a nonlinear inductance $L_J = \Phi_0/2\pi I_c \cos \varphi$ [52] with the flux quantum $\Phi_0 = h/2e \simeq 2.06782 \cdot 10^{-15}$ Wb, the critical current I_c of the junction and the phase difference φ between the macroscopic wave functions Ψ_1 and Ψ_2 describing the superconducting charge carriers in the respective superconducting electrodes. Additionally, a Josephson junction forms a capacitance C_J between the electrodes according to classical electrodynamics.

For our quantum memory experiment, we use one of the most promising designs of a superconducting qubit: the transmission line shunted plasma oscillation (transmon) qubit [19, 53]. It is derived from the Cooper Pair Box (CPB) [54, 55] and is used for modern implementations of quantum computing devices (currently up to 72 qubits [56]). In the following, we give a brief explanation of the physics behind the transmon qubit. The nonlinear Josephson inductance leads to a non-equidistant spacing of the energy levels of the quantized transmon circuit, in

contrast to an ordinary quantized LC-circuit, which can be described as a harmonic quantum oscillator [57]. If we have a sufficiently large detuning, the lowest two energy levels can serve as a qubit.

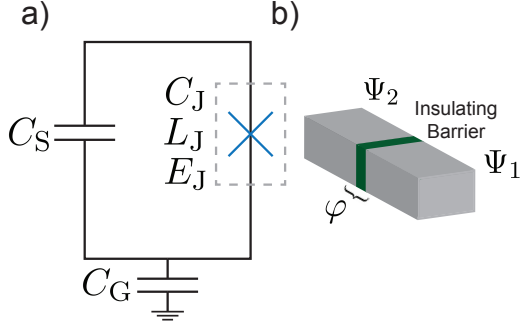


Figure 2.1: Circuit diagram of a transmon qubit.

The JJ is marked as a blue cross and forms an inductance L_J , a capacitance C_J and has an energy E_J . C_S is the shunt capacitance, C_G labels the coupling capacitance. On the right, a JJ is illustrated schematically.

The transmon circuit consists of a Josephson junction shunted by a sufficiently large capacitance C_S [53]. The system possesses an additional coupling capacitance C_G with respect to the resonator. Figure 2.1 shows the circuit representation of the transmon. We define the Josephson energy $E_J \equiv I_c \Phi_0 / 2\pi$ and the capacitive energy $E_C \equiv e^2 / 2C_\Sigma$, where $C_\Sigma = (C_J C_S + C_G C_J + C_G C_S) / (C_G C_J + C_G C_S)$ is the total capacitance of the system. The Hamiltonian of the circuit reads

$$\hat{H} = 4E_G(\hat{n} - n_g)^2 - E_J \cos \hat{\varphi}. \quad (2.1)$$

where \hat{n} denotes the number operator for the Cooper pairs on the superconducting island that is formed by the JJ, C_G and C_S , $\hat{\varphi}$ denotes the phase operator for the Josephson junction and n_g represents the charge offset.

If we work in the phase basis with $\hat{n} = -i \frac{\partial}{\partial \varphi}$, the Schrödinger equation for the transmon is equivalent to Mathieu's differential equation [58]. The eigenenergies can be expressed in terms of Mathieu's characteristic values $a_\nu(n_g)(-E_J/2E_C)$ [59] and their shape strongly depends on the ratio E_J/E_C .

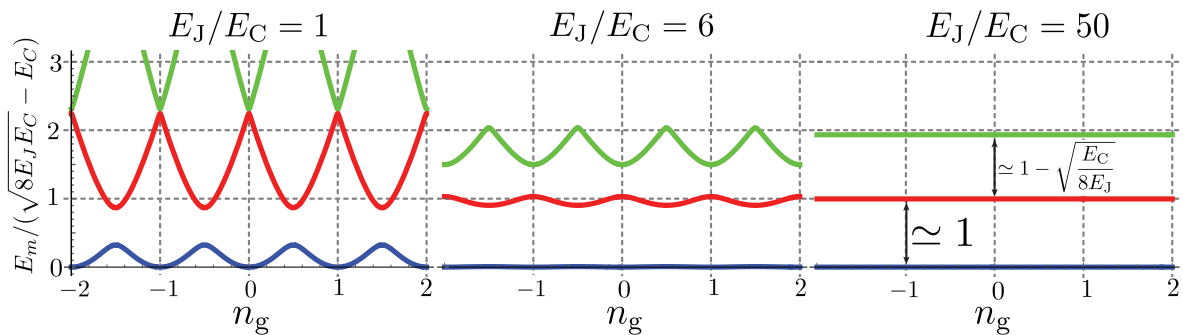


Figure 2.2: Energy dispersion of the transmon qubit for different ratios of E_J/E_C , normalized to the asymptotic qubit energy. For $E_J/E_C \simeq 1$, the energy levels oscillate with “sweet spots” at $n_g = k + 1/2$, $k \in \mathbb{Z}$. The oscillation amplitude decreases exponentially with E_J/E_C , whereas the anharmonicity between the approximately constant energy levels decreases polynomially.

In Fig. 2.2, we plot the lowest three energy levels as a function of n_g . For $E_J/E_C \gg 1$, the

peak-to-peak value of the oscillation of the m th energy level can be approximated as [60]

$$E_m(n_g = 1/2) - E_m(n_g = 0) \simeq (-1)^m E_C \frac{2^{4m+5}}{m!} \sqrt{\frac{2}{\pi}} \left(\frac{E_J}{2E_C} \right)^{\frac{m}{2} + \frac{3}{4}} e^{-\sqrt{8E_J/E_C}}. \quad (2.2)$$

As a result, the energy dispersion flattens exponentially with increasing E_J/E_C . A large ratio of E_J/E_C can be realized by increasing the value of the shunt capacitance. For sufficiently large E_C , the spacing between the energy levels becomes independent of n_g , which implies that the system becomes insensitive to charge noise (fluctuations in n_g), which yields a significant improvement in quantum coherence (this term describes the lifetime of quantum superpositions and is defined more rigorously later in this chapter). We write $E_{ij} \equiv E_j - E_i$ and expand $\cos \varphi = 1 - \varphi^2/2! + \varphi^4/4! + \mathcal{O}(\varphi^6)$, thus, Eq. (2.1) approximately describes an anharmonic Duffing oscillator [61]. The asymptotic energy difference for the lowest levels can be quantized as [53]

$$E_{10} \simeq \sqrt{8E_J E_C} - E_C \quad E_{21} \simeq E_{10} - E_C. \quad (2.3)$$

We define the anharmonicity $\alpha \equiv -E_C/h$ and the relative anharmonicity $\alpha_r = \alpha h/E_{10} \simeq -\sqrt{E_C/8E_J}/h$. As a result, with increasing E_C , the anharmonicity only decreases with a power law, which means there is a regime of E_J/E_C in which we have a flat energy dispersion, but keep a sufficiently large α_r . This transmon regime is characterized by $20 \lesssim E_J/E_C \ll 5 \cdot 10^4$, and typical transmons are operated at $E_J/E_C \simeq 50$.

However, due to the comparatively small anharmonicity, higher energy levels can induce undesired effects, such as state leakage, which may lead to certain limitations in the experiment.

In order to understand how the transmon qubit can be used for QIP, we discuss a general TLS [11, 52]. Thus, we consider that our system consists of a ground state level $|g\rangle = (1,0)^T$ and an excited state level $|e\rangle = (0,1)^T$ separated by an energy difference $E_q = E_{10} = \hbar\omega_q$. In contrast to a classical bit, which can only take either state $|g\rangle$ or $|e\rangle$, a qubit can be in any superposition of $|g\rangle$ and $|e\rangle$ (cf. Fig. 2.1)

$$|\psi\rangle = a|g\rangle + b|e\rangle \quad (2.4)$$

with complex numbers a and b that satisfy the normalization condition $|a|^2 + |b|^2 = 1$.

If we measure the qubit state, $|a|^2$ ($|b|^2$) is the probability to obtain the outcome $|g\rangle$ ($|e\rangle$). The normalization condition allows us to project the qubit state onto the surface of a unit sphere

$$|\psi\rangle = \cos\left(\frac{\theta}{2}\right) |g\rangle + \sin\left(\frac{\theta}{2}\right) e^{i\varphi} |e\rangle \quad (2.5)$$

with $0 \leq \theta \leq \pi$ and $0 \leq \varphi < 2\pi$.

The qubit state is described by the Bloch vector $\mathbf{a} = (a_x, a_y, a_z)^T \equiv (\sin \theta \cos \varphi, \sin \theta \sin \varphi, \cos \theta)^T$. This intuitive description is called the Bloch sphere representation and it is schematically depicted in Fig. 2.4 [62]. The entire physics of an ideal qubit can be understood in the Bloch sphere picture, and it has been studied in detail especially within spin 1/2 nuclear magnetic resonance

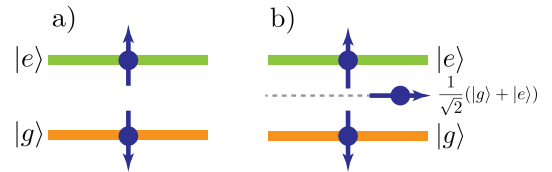


Figure 2.3: A classical bit, can take the discrete states $|g\rangle$ or $|e\rangle$, whereas a qubit can take a continuum of states between $|g\rangle$ and $|e\rangle$

(NMR) [63, 64].

Consequently, we use this picture throughout this work in order to interpret experimental results. Due to interaction of the qubit with the environment, the excited state $|e\rangle$ decays exponentially on a timescale T_1 (energy relaxation). Furthermore, the phase information in the xy -plane of the Bloch sphere is lost on a timescale T_φ (pure dephasing) [12]. The loss of information due to energy relaxation and dephasing is then usually characterized by the qubit T_1 time and the decoherence time T_2 , where

$$\frac{1}{T_2} = \frac{1}{2T_1} + \frac{1}{T_\varphi}. \quad (2.6)$$

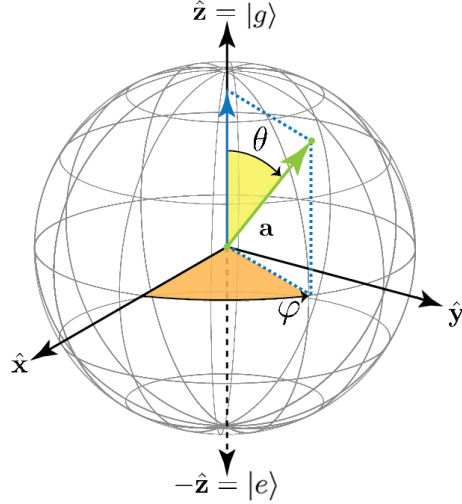


Figure 2.4: Bloch sphere representation of a pure qubit state characterized by its Bloch vector $\mathbf{a}(\theta, \varphi)$

Density matrix formalism The Hilbert-vector representation in Eq. (2.4) is only possible if the quantum system is in a pure state [12, 65]. Coupling of the qubit to the environment yields a loss of the statistical information of the qubit state, which means that we can no longer find a commuting and complete set of observables for the quantum system [66]. For this reason, we make use of the density operator formalism, which allows us to describe arbitrary qubit states by the density matrix ρ . For a physical system, ρ is normalized ($\text{Tr}\rho = 1$) and positive-semidefinite ($\langle\psi|\rho|\psi\rangle \geq 0$). If ρ describes a pure state, we have $\text{Tr}\rho^2 = 1$. For mixed states, we always find $\text{Tr}\rho^2 < 1$ [12]. For a qubit, ρ is given by

$$\rho = \frac{1}{2} \begin{pmatrix} 1 + a_z & a_x - ia_y \\ a_x + ia_y & 1 - a_z \end{pmatrix}. \quad (2.7)$$

This notation enables us to calculate the Bloch vector as $\mathbf{a} = (2\rho_{11} - 1, (\rho_{12} + \rho_{21})/2, -i(\rho_{21} - \rho_{12})/2)^T$. Every operator for single qubit operations can be written as a Hermitian (2×2) matrix. It is common to use the (2×2) identity matrix I together with the Pauli matrices $\{\hat{\sigma}_i\}$ as an operator basis [66]. The Pauli matrices are defined as [67]

$$\hat{\sigma}_1 = \hat{\sigma}_x = \begin{pmatrix} 0 & 1 \\ 1 & 0 \end{pmatrix} \quad \hat{\sigma}_2 = \hat{\sigma}_y = \begin{pmatrix} 0 & -i \\ i & 0 \end{pmatrix} \quad \hat{\sigma}_3 = \hat{\sigma}_z = \begin{pmatrix} 1 & 0 \\ 0 & -1 \end{pmatrix}. \quad (2.8)$$

$\hat{\sigma}_x$, $\hat{\sigma}_y$ and $\hat{\sigma}_z$ correspond to the measurement operators of the qubit state with respect to the x -, y - or z - axis of the Bloch sphere. The single qubit Hamiltonian can be expressed in the Pauli basis as [52]

$$\hat{H}_q = \frac{\hbar\omega_q}{2} \hat{\sigma}_z. \quad (2.9)$$

We define the vector of the Pauli matrices as $\boldsymbol{\sigma} \equiv (\hat{\sigma}_x, \hat{\sigma}_y, \hat{\sigma}_z)^T$. The Pauli matrices obey the relations [12]

$$\rho = \frac{1}{2}(I + \mathbf{a} \cdot \boldsymbol{\sigma}) = \frac{1}{2}(I + \text{Tr}(\rho \hat{\sigma}_x) \hat{\sigma}_x + \text{Tr}(\rho \hat{\sigma}_y) \hat{\sigma}_y + \text{Tr}(\rho \hat{\sigma}_z) \hat{\sigma}_z) \quad (2.10)$$

and

$$\hat{\sigma}_j \hat{\sigma}_k = \delta_{jk} I + i \sum_{l=1}^3 \epsilon_{jkl} \hat{\sigma}_l. \quad (2.11)$$

with the Kronecker delta δ_{jk} and the Levi-Civita symbol ϵ_{jkl} . An important quantum state is the completely mixed state (CMS) and denoted with ρ_* . In the single qubit case, this state corresponds to the center of the Bloch sphere [52], $\rho_* = I/2$. For a quantum system of dimension d , we obtain $\rho_* = I/d$ [68].

2.2 Reconstruction of a quantum state

In Sec. 2.1, we state that we can describe the physics of a qubit entirely by considering its density operator ρ , however, we may ask how we can get experimental access to the qubit state and how we can manipulate our system. These questions will be our guidelines throughout this section, and we will see that we can solve this problem by coupling our transmon qubit to electrical field modes [69]. First of all, we discuss how this setup can be used to measure the qubit state with respect to the quantization axis (z -axis) in Sec. 2.2.1. After that, we point out how the same setup can be used for qubit control by applying pulsed microwave radiation. Finally, we explain how to perform QST, which enables us to reconstruct the total density matrix of the qubit.

2.2.1 Coupling of qubit and cavity

Within this section, we show how a detuned resonator can serve for readout (RO) purposes [24, 52]. The schematic setup is depicted in Fig. 2.5. The qubit is coupled to the cavity in such

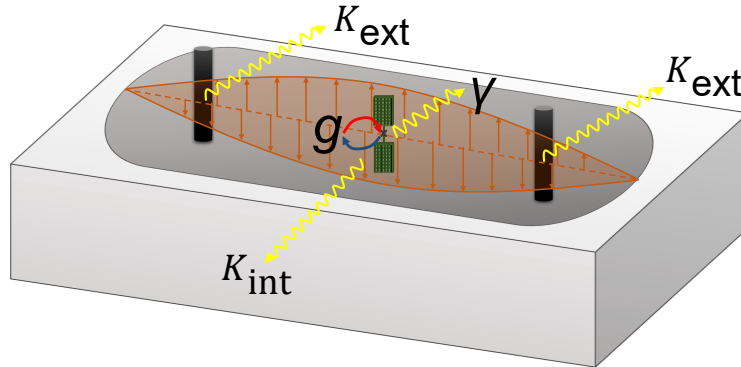


Figure 2.5: Circuit QED setup: the qubit (green) is placed inside a 3D cavity resonator (gray). The coupling to the electrical field (orange) is characterized by g . The quantity $\kappa = \kappa_{int} + \kappa_{ext}$ characterizes the resonator decay by internal and external channels, such as the antennas (black). γ denotes the qubit decay rate.

a way that it interacts with the transversal standing wave pattern of the electrical field. For a rectangular cavity with length L , width W and height H , we obtain the frequency of the mnl th transversal electric mode (TE_{mnl}) as [70]

$$\omega_{mnl} = \frac{\pi c}{\sqrt{\epsilon_r \mu_r}} \sqrt{\left(\frac{m}{L}\right)^2 + \left(\frac{n}{W}\right)^2 + \left(\frac{l}{H}\right)^2} \quad (2.12)$$

with the electric (magnetic) permittivity ϵ_r (μ_r) and the speed of light $c = 2.99792 \cdot 10^8 \text{ m s}^{-1}$.

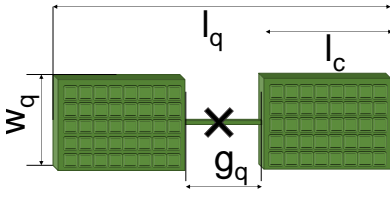


Figure 2.6: Conceptual design of our transmon qubit. The shunt capacitance is formed by two paddles with a length l_c and a width w_c . The total length l_q determines the dipolar coupling strength.

Our transmon design shown in Fig. 2.6 has the advantage that the shunt capacitor C_S can be simultaneously used as a dipolar antenna. Hence the coupling constant g depends on the dipole moment and reads $g = -l_q e \sqrt{2\omega_r / \varepsilon_0 \hbar V}$, where $e = 1.602 \cdot 10^{-19}$ C labels the elementary charge and $\varepsilon_0 = 8.854 \cdot 10^{-12}$ A s V $^{-1}$ m $^{-1}$. We recognize that g can be varied by engineering the transmon length l_q or the resonator volume V . The cavity is physically described as a harmonic quantum oscillator with a multimode structure.

Driving the system with a classical microwave signal induces a coherent state $|\alpha\rangle$, which is a superposition of the eigenstates of the photon number operator $\hat{a}^\dagger \hat{a}$ (Fock states) that obeys a Poissonian distribution [71]. \hat{a}^\dagger and \hat{a} denote the photon creation and annihilation operator, respectively.

We operate the system in the strong coupling regime, which means that the coupling strength g for qubit-resonator coupling satisfies $g \gg \gamma, \kappa$, where γ and κ denote the decay rates for the qubit and the resonator respectively [24]. κ is directly related to the loaded Q -factor Q_L of the resonator via $\kappa = 2\pi\omega_r / Q_L = 2\pi\Delta\omega$, with the resonance frequency ω_r and the linewidth $\Delta\omega$ of the Lorentzian resonator peak [72]. Furthermore, we let $g \ll \omega_q, \omega_r$, which implies that the interaction strength is weak in comparison to the eigenenergies of the system. The physics of the total system consisting of cavity and qubit is then described by the Jaynes-Cummings Hamiltonian [24, 73]

$$\hat{H}_{\text{JC}} = \hbar\omega_r \left(\hat{a}^\dagger \hat{a} + \frac{1}{2} \right) + \frac{\hbar\omega_q}{2} \hat{\sigma}_z + \hbar g (\hat{a} \hat{\sigma}_+ + \hat{a}^\dagger \hat{\sigma}_-) \quad (2.13)$$

where $\hat{\sigma}_+$ and $\hat{\sigma}_-$ label the creation and annihilation operator for qubit excitations, respectively. In the special case of dispersive circuit QED, the detuning of resonator and qubit is much larger than the coupling strength $|\Delta| \equiv |\omega_q - \omega_r| \gg g$. Hence, the direct energy exchange is prohibited. By applying the canonical transformation $\hat{U} = \exp(g/\Delta (\hat{a} \hat{\sigma}_+ - \hat{a}^\dagger \hat{\sigma}_-))$ [24, 52] to \hat{H}_{JC} and expanding up to second order in g , considering terms up to g^2/Δ , we obtain the dispersive Hamiltonian

$$\hat{H}_{\text{disp}} = \hat{U} \hat{H}_{\text{JC}} \hat{U}^\dagger = \hbar \left(\omega_r + \underbrace{\frac{g^2}{\Delta}}_{\text{AC Stark shift}} \hat{\sigma}_z \right) \hat{a}^\dagger \hat{a} + \frac{\hbar}{2} \left(\omega_q + \underbrace{\frac{g^2}{\Delta}}_{\text{Lamb shift}} \right) \hat{\sigma}_z + \mathcal{O}\left(\frac{g^2}{\Delta^2}\right). \quad (2.14)$$

We define the dispersive shift as $\chi = g^2/\Delta$ [47] and we observe that the qubit modifies the resonance frequency. Moreover, we observe that the resonator frequency shifts monotonically from $\omega_r + \chi$ to $\omega_r - \chi$ with the qubit population in $|e\rangle$, which means that we can use the resonator transmission as a direct measure for the qubit state. The AC Stark effect [64] implies that every

photon in the cavity causes an additional frequency shift of χ . However, we must state that Eq. (2.14) and the resulting dispersive shift is just an approximation. The energy ladder for the dispersive system is shown in Fig 2.7. For a transmon qubit, the low anharmonicity can yield a population of higher levels, which causes additional shifts $\chi_{ij} = g_{ij}/(\omega_{ij} - \omega_r)$ [19, 53]. Let $|f\rangle$ denote the third energy level of the transmon (cf. Fig. 2.2). The $|g\rangle \leftrightarrow |f\rangle$ transition can cause an effect because $\omega_{gf}/2$ is close to ω_q and the transition can be induced as a second order process. We denote the resulting effective shift for the transmon qubit with $\chi' = \chi_{ge} - \chi_{ef}/2$. Furthermore, we neglect higher order effects, such as the Kerr shift [74, 75], that scales with the square of the photon number ($\hat{a}^\dagger \hat{a}^\dagger \hat{a} \hat{a}$) and which is characterized by its coupling constant K . Moreover, coupling to additional cavity modes is neglected in Eq. (2.14), which would yield additional shifts.

2.2.2 Qubit control

In order to investigate the qubit dynamics induced by a coherent microwave drive, we write down the driven qubit Hamiltonian in the lab-frame [52],

$$\hat{H}_d = \frac{\hbar\omega_q}{2}\hat{\sigma}_z + \hbar\Omega_d \cos(\omega_d t + \varphi_d)\hat{\sigma}_x, \quad (2.15)$$

with the drive amplitude Ω_d , the drive frequency ω_d and the phase φ_d . From an intuitive point of view, we expect periodic population exchange, because the drive couples $|g\rangle$ and $|e\rangle$ via the off-diagonal elements of \hat{H}_d . Similar to Larmor precession of a magnetic moment [76], the Bloch vector precesses about the z -axis with ω_d . We get rid of these dynamics by transforming to a

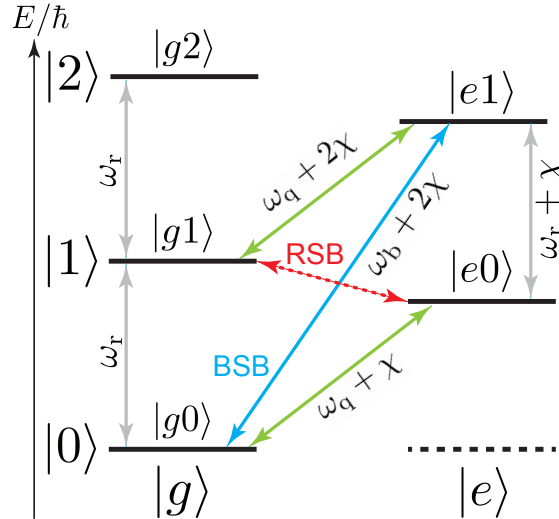


Figure 2.7: Energy levels resulting from the Jaynes-Cummings model. The left (right) ladder depicts the energy levels for Fock states in the cavity if the qubit is in state $|g\rangle$ ($|e\rangle$). The energy spacing of the cavity modes depends on the qubit state and differs by a term χ . The AC Stark effect yields a shift of χ in ω_q for each photon in the cavity. The nonlinear Kerr shift is neglected, which means that the cavity is treated as a harmonic quantum oscillator

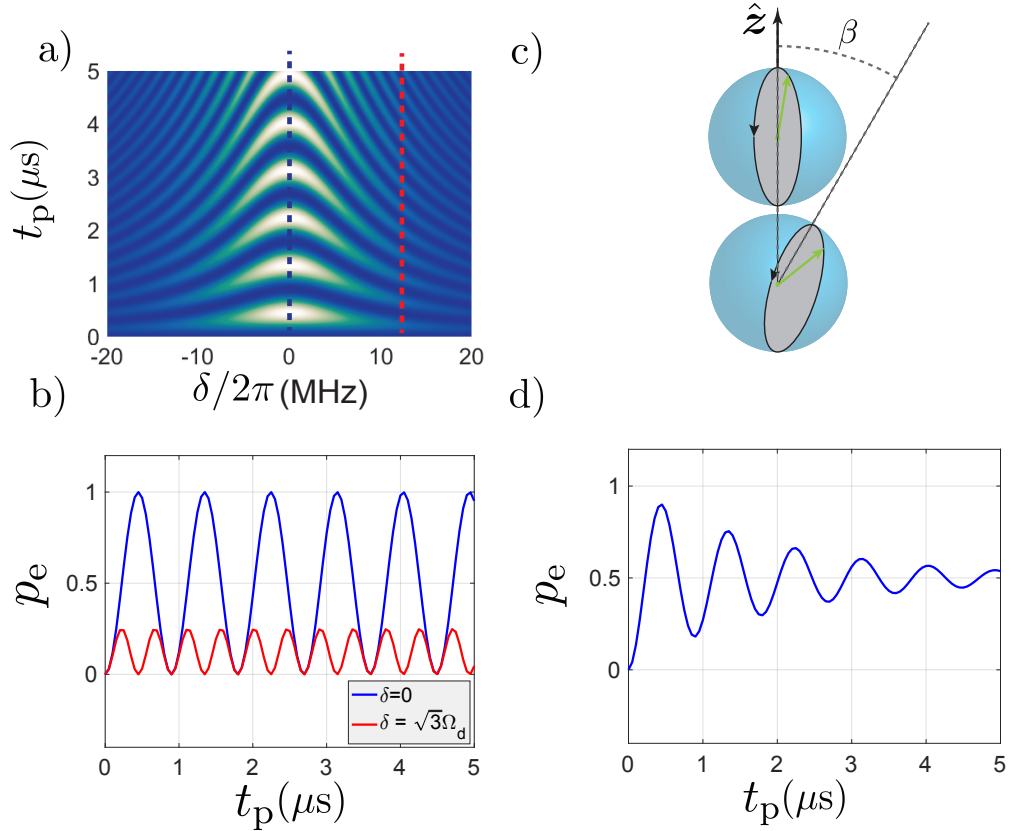


Figure 2.8: a) Qubit Rabi oscillations for $\Omega_d/2\pi = 7$ MHz. b) Slices for a detuning of $\delta = 0$ and $\delta = \sqrt{3}\Omega_d$. With increasing detuning, the amplitude decreases whereas the Rabi frequency increases hyperbolically. c) Geometric picture for detuned Rabi oscillations. With increasing δ , the rotation plane gets tilted away from the z -axis. We depict the case $\beta = -30^\circ$, corresponding to $\delta = \Omega_d/\sqrt{3}$. d) Rabi oscillations, including depolarization with a decay time $T_1 = 2 \mu\text{s}$. For $t \gg T_1$, the steady state is the CMS

coordinate system that rotates with the drive frequency via $\psi = U\psi'$ with $U = e^{i\frac{\omega_d t}{2}\hat{\sigma}_z}$ [52]. The Hamiltonian in the rotating frame after applying the rotating wave approximation (RWA) then reads

$$\hat{H}'_d = U^\dagger \hat{H} U - i\hbar U^\dagger \frac{\partial U}{\partial t} = \frac{\hbar\delta}{2}\hat{\sigma}_z + \frac{\hbar\Omega_R}{2}(\cos\varphi_d\hat{\sigma}_x + \sin\varphi_d\hat{\sigma}_y) \quad (2.16)$$

with $\delta \equiv \omega_q - \omega_d$ the Rabi frequency [77] $\Omega_R = \sqrt{\Omega_d^2 + \delta^2}$. Equation (2.16) implies that the qubit population is modulated between $|g\rangle$ and $|e\rangle$ with frequency Ω_R . The amplitude of this modulation depends on the detuning δ . We usually drive the system with $\delta = 0$, which means that the Rabi frequency is equal to the drive amplitude. Theory plots for these Rabi oscillations are depicted in Fig 2.8 a) and Fig 2.8 b). A Rabi oscillation can be interpreted as a rotation movement of the Bloch vector about an axis that is defined by the phase φ_d of the microwave drive [11]. The rotation plane is tilted by an angle β with $\sin\beta = \delta/\Omega_R$ [cf. Fig. 2.8 c)]. We rotate about the y -axis for $\varphi_d = 0$ and about the x -axis for $\varphi_d = \pi/2$. For experimental purposes, we define the θ -time t_θ for a rotation by an angle θ at resonance and we find $t_\theta = \theta/\Omega_R$. We

define a θ -pulse as a microwave pulse with duration t_θ . Important types of pulses for QIP protocols are the π -pulse [64], which swaps the $|g\rangle$ and $|e\rangle$ population, i.e., we reach the first maximum of the Rabi oscillation, and the $\pi/2$ -pulse [64], that creates superposition states in the xy -plane from $|g\rangle$ or $|e\rangle$.

Sideband transitions In Fig. 2.7, we see that it is possible to obtain transitions between the left and the right energy ladder, called sideband transitions [47, 78]. For our memory protocol, we need the blue sideband (BSB) transition $|g0\rangle \leftrightarrow |e1\rangle$, which is induced by a simultaneous excitation of the qubit and the resonator. Conservation of parity requires a two photon (second order) process in order to drive the BSB. The interaction Hamiltonian for the BSB then reads [78]

$$\hat{H}_{\text{BSB}} = \frac{\hbar g^3 \Omega_d^2}{(\omega_m - \omega_b/2)^2 (\omega_q - \omega_b/2)^2} (\hat{a}^\dagger \hat{\sigma}^+ + \hat{a} \hat{\sigma}^-) = A (\hat{a}^\dagger \hat{\sigma}^+ + \hat{a} \hat{\sigma}^-) \quad (2.17)$$

with the mode frequency ω_m and the BSB frequency $\omega_b = \omega_m + \omega_q + \sum_i \chi'_i$, where we have to correct the sum frequency of resonator and qubit with dispersive shifts χ'_i of the respective cavity modes, which also depend on photon population n . We label the prefactor of the Hamiltonian that depends on the coupling strength g and the respective frequencies as A . We observe that Eq. (2.17) couples only states $|n, g\rangle$ and $|n+1, e\rangle$, hence the system decouples to doublets similar to the Jaynes-Cummings model [52, 79]

$$\hat{H}_{\text{BSB},n} \begin{pmatrix} |n, g\rangle \\ |n+1, e\rangle \end{pmatrix} = \begin{pmatrix} 0 & A \sqrt{n+1} \\ A \sqrt{n+1} & 0 \end{pmatrix} \cdot \begin{pmatrix} |n, g\rangle \\ |n+1, e\rangle \end{pmatrix}. \quad (2.18)$$

2.2.3 Quantum state tomography

A measurement projects the state onto the quantization axis, which implies that all information about the φ -angle of the Bloch vector is lost. In order to reconstruct the Bloch vector \mathbf{a} , we need to prepare the state two more times¹ and detect its projections onto the x - and y -axis respectively [80], which can be realized by rotating the x - and y -components with $\pi/2$ -pulses. This technique is called quantum state tomography (QST) [12, 81]. For the single qubit case, we aim for finding the evolution coefficients in Eq. (2.10). We reconstruct the density matrix ρ by using a quantity μ that can be obtained by measuring the qubit state with respect to the z -axis. μ should uniquely identify the probabilities for the qubit to be in the $|g\rangle$ or in the $|e\rangle$ state. This means that the system is in $|e\rangle$ if we measure μ_e and in state $|g\rangle$ for μ_g . The probability $p_e(\mu)$ for finding the system in $|e\rangle$ should be a monotonic function of μ with $\min(\mu_g, \mu_e) \leq \mu \leq \max(\mu_g, \mu_e)$ and $p_e(\mu_e) = 1$ and $p_e(\mu_g) = 0$, which allows us to uniquely identify the projection of the qubit state onto the quantization axis. QST is then performed as follows:

1. Measure the projection of the qubit state onto the z -axis in order to obtain μ_z
2. Measure the projection of the qubit state onto the x -axis. To do that, we apply a $\frac{\pi}{2}$ -pulse with 0° phase and obtain μ_x

¹Despite the loss of geometrical intuition, this procedure can be generalized for arbitrarily large systems of dimension d , requiring $\mathcal{O}(d^2)$ projections [12], which results from the fact that any d -dimensional density matrix can be written as a linear combination of d^2 basis matrices.

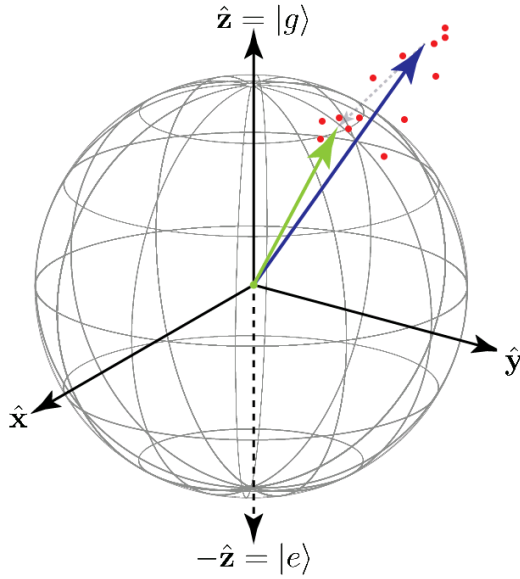


Figure 2.9: Schematic illustration of the effect of the MLE. The red dots denote several measurement outcomes of the same state affected by noise in the experiment. The Bloch vector (blue) is calculated from the raw data. Unphysical states correspond to $|\mathbf{a}| > 1$ and are reprojected onto the surface of the Bloch sphere (green)

3. Measure the projection of the qubit state onto the y -axis, which means we apply a $\frac{\pi}{2}$ pulse with 90° . This yields μ_y

This information, together with the known functional behavior $p_e(\mu)$, is sufficient to reconstruct the density matrix using Eq. (2.7).

Maximum-likelihood-estimation for QST Although it is apparent that ρ is already normed and Hermitian, in experiment, there can be unphysical reconstructed states which show $\text{Tr}\rho^2 > 1$, caused e.g. by noise. We enforce physicality by using a maximum-likelihood-estimation (MLE) [82]. Intuitively, unphysical reconstructed states correspond to Bloch vectors \mathbf{a} with $|\mathbf{a}| > 1$, and the MLE can be regarded as a reprojecting of these states onto the Bloch sphere, as illustrated in Fig. 2.9. A detailed discussion can be found in Sec. A.2 in the appendix. We parametrize an arbitrary physically valid state $\tilde{\rho}(\{\tilde{\mu}_i\})$ with $\tilde{\rho} = T^\dagger T / \text{Tr}(T^\dagger T)$ with

$$T = \begin{pmatrix} t_1 & 0 \\ t_3 + it_4 & t_2 \end{pmatrix} \quad (2.19)$$

where $t_1, t_2, t_3, t_4 \in \mathbb{R}$ [81]. We repeat the experiment for N times, which enables us to calculate the standard deviations $\sigma_{x,y,z}$ of the outcomes, assuming a normal distribution. The probability that t_1, t_2, t_3 and t_4 describe the state of the physical system is then given by

$$P(t_1, t_2, t_3, t_4) = \mathcal{N} \prod_{i=x,y,z} \prod_{j=1}^N e^{-\frac{(\mu_i^{(j)} - \bar{\mu}_i)^2}{2\sigma_i^2}} \quad (2.20)$$

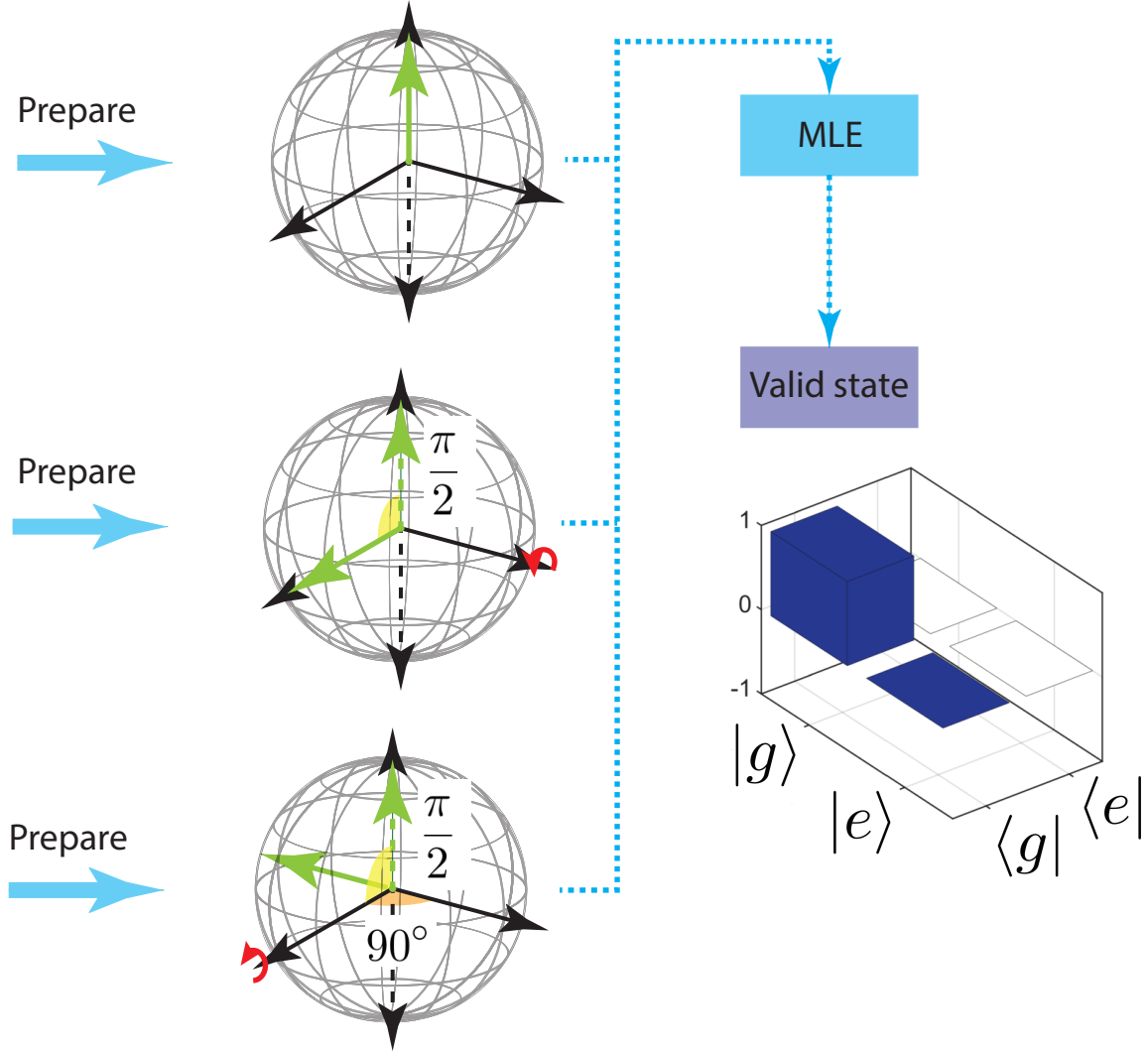


Figure 2.10: Schematic illustration of single qubit QST. The state is prepared for 3 times and projected onto the z -, x - and y -axis. After that, the MLE is applied in order to obtain the density matrix, which is plotted as a 3D bar graph. This example depicts the ground state reconstruction.

where \mathcal{N} is a normalization constant. From Eq. (2.20), it can be directly derived that we maximize the probability that $\tilde{\rho}$ is the physical state of the qubit by considering the minimum of the likelihood-functional

$$\mathcal{L}(t_1, t_2, t_3, t_4) = \sum_{i=x,y,z} \frac{1}{2\sigma_i^2} (\tilde{\mu}_i - \mu_i)^2 \quad (2.21)$$

where μ_i is the average of the N values $\mu_i^{(j)}$. Our QST routine including MLE is summarized in Fig. 2.10

2.3 Reconstruction of quantum processes

Within this section, we introduce the concept of a quantum process (QP), which can be regarded as a transition from a quantum state ρ to another quantum state ρ' [12]. This allows us to investigate the effect of controlled manipulations of our system, but also effects induced by energy relaxation, dephasing or general noise. In order to reconstruct quantum processes experimentally, we introduce quantum process tomography (QPT) in Sec. 2.3.2. We make use of the standard QPT approach, a procedure that uses a set of prepared input states in order to get full access to the QP [14]. We discuss this technique for an arbitrary quantum system of dimension d , after that, we focus on the single qubit system with $d = 2$.

2.3.1 Quantum processes

If we consider a quantum system on a d -dimensional Hilbert space \mathcal{H} , a quantum process \mathcal{E} is a linear map $\mathcal{E} : \mathcal{H} \rightarrow \mathcal{H}'$ and $\rho' = \mathcal{E}(\rho)$. \mathcal{E} is often referred to as a “superoperator” since it takes a density operator as input argument and maps it onto another density operator. Throughout this thesis, we deal with Markovian quantum processes (QP’s) [83], which implies that \mathcal{E} is completely positive (CP)

[12]. For a physically valid QP, we can find a Kraus representation [84], which means there are operators $\{E_i\}$ such that

$$\mathcal{E}(\rho) = \sum_{i=1}^{d^2} E_i \rho E_i^\dagger. \quad (2.22)$$

The Kraus operators satisfy the trace-preserving (TP) condition

$$\sum_{i=1}^{d^2} E_i E_i^\dagger = I. \quad (2.23)$$

This means that the identity I is a fixed point of \mathcal{E} . An important result for QP’s on a d -dimensional system is the Choi-Jamiolkowski isomorphism [85] that maps the space $\mathcal{L}(\mathcal{H}_d)$ of linear operators on the Hilbert space \mathcal{H}_d onto the Hilbert space $\mathcal{H}_d \otimes \mathcal{H}_d$ [86]. This means that there exists a bijection between the quantum process \mathcal{E} in $\mathcal{L}(\mathcal{H}_d)$ and the quantum states $\rho_{\mathcal{E}}$ in \mathcal{H}_{d^2}

$$\rho_{\mathcal{E}} = \frac{1}{d} \sum_{i,j=1}^d (I_d \otimes \mathcal{E}) |ii\rangle \langle jj| \quad (2.24)$$

with an orthonormal qubit basis $|j\rangle$ and the d -dimensional identity matrix I_d . $\rho_{\mathcal{E}}$ can be regarded as an auxiliary d^2 dimensional density matrix. Thus, all concepts introduced for quantum state can be used for quantum processes [87]. This is especially important for the distance measures that are discussed in Sec. 2.4 For the single qubit case ($d = 2$), a quantum process can be regarded as an affine map for the Bloch vector, which means that \mathcal{E} maps \mathbf{a} onto \mathbf{a}' via [88]

$$\mathbf{a}' = M \cdot \mathbf{a} + \mathbf{c} \quad (2.25)$$

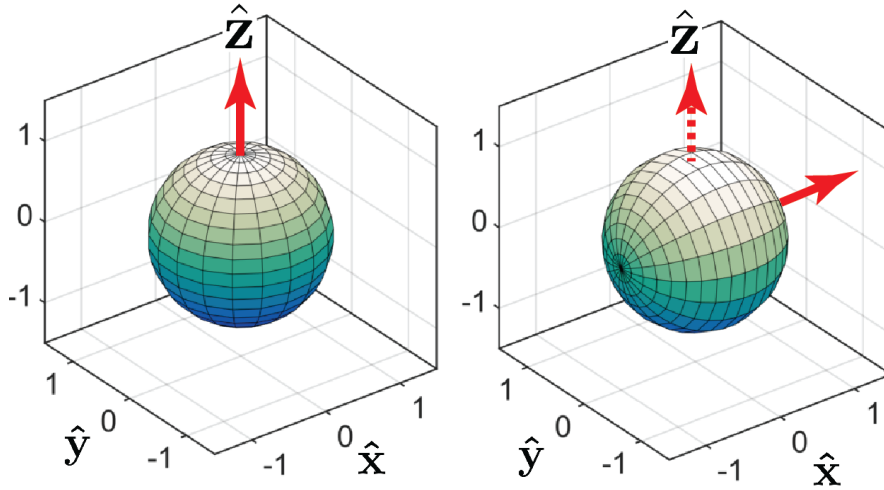


Figure 2.11: Rotation about the y -axis. This operation is induced by applying a $\pi/2$ -pulse with a phase of 0° to the $|g\rangle$ state. The quantization axis $\hat{\mathbf{z}}$ is rotated onto the x -axis.

with a 3×3 matrix M which, in an intuitive picture, causes deformations and rotations of the Bloch sphere and a translation \mathbf{c} [12]. We expand the Kraus operators in the Pauli basis

$$E_i = \alpha_i I + \sum_{k=1}^3 a_{ik} \hat{\sigma}_k. \quad (2.26)$$

The coefficients α_i and a_{ik} can be obtained by multiplying Eq. (2.26) with I and with each Pauli matrix $\hat{\sigma}_m$, respectively, using Eq. (2.11) and taking the trace. It can then be derived that we can calculate the mapping matrix M and the translation \mathbf{c} as [12]

$$M_{jk} = \sum_{l=1}^4 \left\{ a_{lj} a_{lk}^* + a_{lj}^* a_{lk} + \left(|\alpha_l|^2 - \sum_{p=1}^3 a_{lp} a_{lp}^* \right) \delta_{kj} + i \sum_{p=1}^3 \epsilon_{jpk} (\alpha_l a_{lp}^* - \alpha_l^* a_{lp}) \right\} \quad (2.27)$$

$$c_k = 2i \sum_{l=1}^4 \sum_{j,p=1}^3 \epsilon_{jpk} a_{lj} a_{lp}^*. \quad (2.28)$$

In order to get an intuition, we want to discuss some categories of quantum processes that are relevant for our experiments and their effect on the Bloch sphere, namely rotations, energy relaxation, dephasing and the depolarizing process. We observe that the simplest process is given by $\mathcal{E}(\rho) = \rho$, with the identity as the only Kraus operator. This process also describes an ideal quantum memory, as it is desired that the regained state is preserved during the memory storage time.

Rotations A rotation about an axis \mathbf{n} by an angle α is described by the operator [12]

$$\hat{R}_{\mathbf{n}}(\alpha) \equiv e^{-i\frac{\alpha}{2}\mathbf{n}\cdot\boldsymbol{\sigma}} = \cos\frac{\alpha}{2}I - i\sin\frac{\alpha}{2}\mathbf{n}\cdot\boldsymbol{\sigma}. \quad (2.29)$$

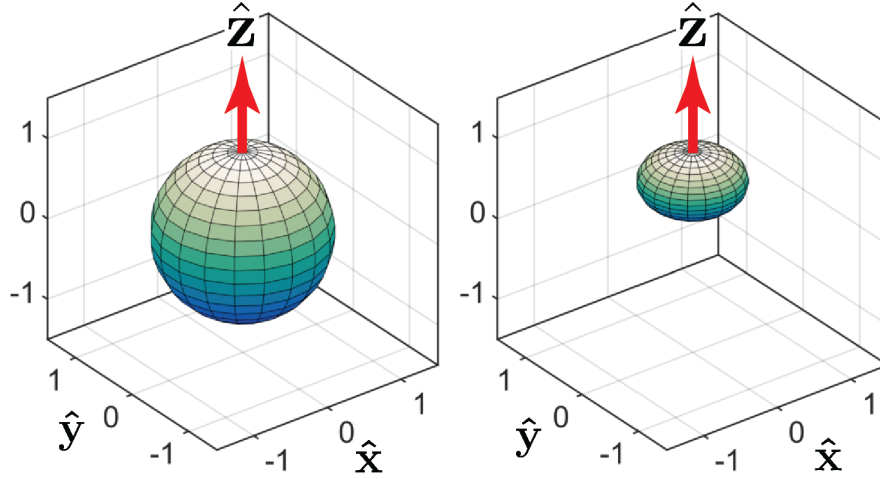


Figure 2.12: Effect of energy relaxation. The Bloch sphere shrinks towards the north pole, which represents the ground state. For $t \rightarrow \infty$, the Bloch sphere contracts to a single point. The $|e\rangle$ -state decays with e^{-t/T_1}

We especially obtain for rotations about the x -, y - and z -axis [89]

$$\hat{R}_x(\alpha) = \begin{pmatrix} \cos \frac{\alpha}{2} & -i \sin \frac{\alpha}{2} \\ -i \sin \frac{\alpha}{2} & \cos \frac{\alpha}{2} \end{pmatrix} \quad \hat{R}_y(\alpha) = \begin{pmatrix} \cos \frac{\alpha}{2} & -\sin \frac{\alpha}{2} \\ \sin \frac{\alpha}{2} & \cos \frac{\alpha}{2} \end{pmatrix} \quad \hat{R}_z(\alpha) = \begin{pmatrix} e^{-i\frac{\alpha}{2}} & 0 \\ 0 & e^{i\frac{\alpha}{2}} \end{pmatrix}. \quad (2.30)$$

As $\rho' = \hat{R}_n(\alpha)\rho\hat{R}_n(\alpha)^\dagger$, $\hat{R}_n(\alpha)$ is the only Kraus operator. Figure 2.11 shows the transformation of the Bloch sphere Eq. (2.25) for a $\pi/2$ rotation about the y -axis.

Energy relaxation Intuitively, energy relaxation maps every quantum state to $|g\rangle$ for $t \gg T_1$, which means the Bloch sphere shrinks to a single point located at its north pole. This process possesses two Kraus operators [12]

$$E_0 = \begin{pmatrix} 1 & 0 \\ 0 & \sqrt{1-\gamma} \end{pmatrix} \quad E_1 = \begin{pmatrix} 0 & \sqrt{\gamma} \\ 0 & 0 \end{pmatrix} \quad (2.31)$$

and is depicted in Fig. 2.12 for $t = T_1$.

Dephasing Dephasing can be modelled by considering “random-walk” rotations about the z -axis. If we consider a phase flip with probability p , we obtain two Kraus operators $E_0 = \sqrt{p}I$ and $E_1 = \sqrt{1-p}\hat{\sigma}_z$ [12]. If we apply this process multiple times assuming Markovian behavior, we project the Bloch sphere to the z -axis. We illustrate the process in Fig. 2.13 for $p = 0.75$

Depolarizing process The depolarizing process is characterized by a loss of statistical information about the system. This will always be the case during the time we drive our system. We model the process again with a Markov assumption and state that we loose all statistical

information (that means, we end up in ρ_*), with probability p . That means, we have [12]

$$\mathcal{E}(\rho) = p\rho_* + (1-p)\rho. \quad (2.32)$$

The Kraus operators for the system are then given by $E_0 = \sqrt{1-3p/4}I$, $E_1 = \sqrt{p}\hat{\sigma}_x/2$, $E_2 = \sqrt{p}\hat{\sigma}_y/2$ and $E_3 = \sqrt{p}\hat{\sigma}_z/2$. We depict the process in Fig. 2.14 for $p = 0.5$. The asymptotic behavior for long times is modelled by $p = 1$. We label this process the “completely depolarizing process” (CDP) and denote it \mathcal{E}_* with

$$\mathcal{E}_*(\rho) = \frac{1}{4}(\rho + \sum_{i=1}^3 \hat{\sigma}_i \rho \hat{\sigma}_i). \quad (2.33)$$

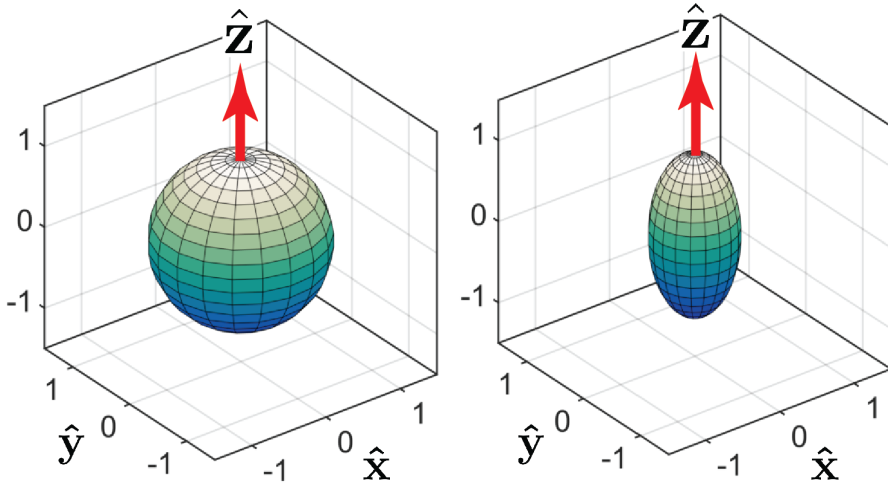


Figure 2.13: Bloch sphere representation of the pure dephasing process. The loss of phase coherence in the xy -plane leads to a shrinkage of the Bloch sphere towards the quantization axis. For $t \rightarrow \infty$, the Bloch sphere contracts completely to the quantization axis.

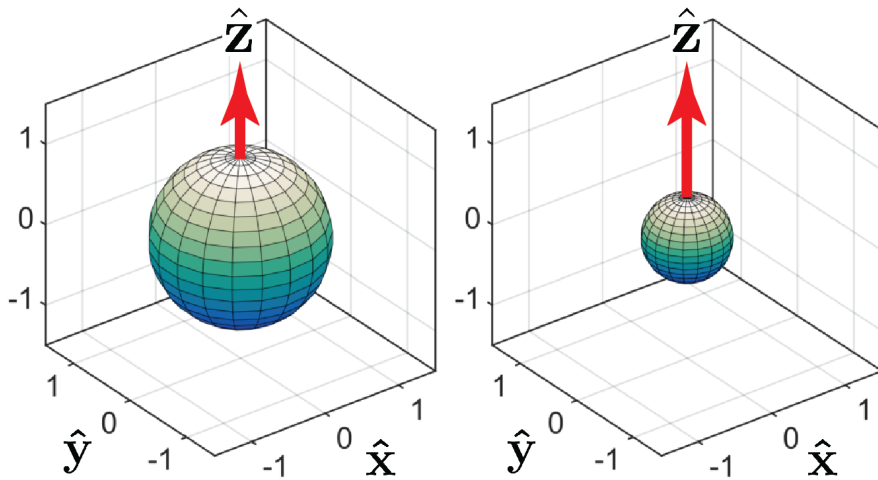


Figure 2.14: Effect of the depolarizing channel. Depolarization leads to a mixing of the qubit state. The Bloch sphere contracts symmetrically and continuously towards the CMS ρ_* .

2.3.2 Quantum process tomography

In this section, we show how we can obtain the Kraus representation experimentally by using QPT. Since this technique works for quantum systems with arbitrary dimension d , we initially discuss QPT for this general case and after that, we deal with single qubit QPT. The first idea is to choose d^2 fixed operators $\{B_m\}$ which form an operator basis, in which we evolve \mathcal{E} [90]

$$\mathcal{E}(\rho) = \sum_{m,n} B_m \rho B_n^\dagger \chi_{mn} \quad (2.34)$$

with the positive and Hermitian quantum process matrix χ of dimension $(d^2 \times d^2)$, which encodes all information of the superoperator \mathcal{E} [12]. This means that our goal of reconstructing the QP is achieved if an expression for the χ -matrix in terms of experimentally available data can be found. To do so, we need to apply the process under investigation to d^2 independent quantum states ρ_i of the system [14]. The ρ_i then form a basis for the space of the complex Hermitian $(d \times d)$ matrices. We apply \mathcal{E} to the input states and reconstruct the outcome ρ_i with QST. We decompose the result in the ρ_i -basis

$$\mathcal{E}(\rho_i) = \sum_j \lambda_{ij} \rho_j. \quad (2.35)$$

Furthermore, we use the ρ_i -basis to write

$$B_m \rho_i B_n^\dagger = \sum_j \beta_{ji}^{mn} \rho_j. \quad (2.36)$$

If χ is reshaped into a column vector $\boldsymbol{\chi}$ and the d^2 coefficients λ_{ij} are reordered in a column vector $\boldsymbol{\lambda}$, the β_{ji}^{mn} can be interpreted as the entries of a matrix β with $\beta_{ji, mn} = \beta_{ji}^{mn}$ and the problem can be rewritten as

$$\boldsymbol{\lambda} = \beta \cdot \boldsymbol{\chi}. \quad (2.37)$$

This means that $\boldsymbol{\chi}$ can be obtained by multiplying $\boldsymbol{\lambda}$ with the (pseudo-)inverse of β and reshaping $\boldsymbol{\chi}$ [12]. After that, χ can be diagonalized $\chi = UDU^\dagger$ with $D = \text{diag}(q_1, \dots, q_{d^2})$ and the Kraus operators E_i can be calculated by using [88]

$$E_i = \sqrt{q_i} \sum_m U_{mi} B_m. \quad (2.38)$$

If χ represents a physical process matrix, it must be positive Hermitian, which implies that there are no negative eigenvalues: $q_i \geq 0$. Additionally, χ should be trace-preserving according to Eq. (2.23)

$$\sum_{m,n} B_m B_n^\dagger \chi_{mn} = I. \quad (2.39)$$

In the same manner as for QST, it can happen that the reconstructed χ is not positive or that Eq. (2.39) is not satisfied. In order to deal with these unphysical outcomes [91], we again employ an MLE approach [92, 93]. We thus parametrize an arbitrary physical process matrix $\tilde{\chi}(\mathbf{t})$ and minimize the distance $\Delta(\mathbf{t})$ to the reconstructed χ under the constraint Eq. (2.39) [88]. We

discuss this procedure in detail in Sec. A.4 in the appendix. The optimization problem then reads

$$\Delta(\mathbf{t}) = \|\tilde{\chi}(\mathbf{t}) - \chi\|_F^2 + \lambda \|\mathcal{B} \cdot (\tilde{\chi}(\mathbf{t}) \otimes I) \cdot \mathcal{B}^\dagger - I\|_F^2 \quad (2.40)$$

where $\mathcal{B} \equiv (B_1^\dagger \dots B_{d^2}^\dagger)$ is a $(d \times d^3)$ block matrix consisting of the conjugated basis matrices and $\|\cdot\|_F$ denotes the Frobenius norm². λ is introduced as a Lagrangian multiplier. We obtain $\tilde{\chi}(\mathbf{t}_{\min})$ with $\mathbf{t}_{\min} = \arg \min_{\mathbf{t}} \Delta(\mathbf{t})$. We have to state that the optimization problem is not convex in general, implying that it can happen that we do not converge to the global minimum. We can avoid that we get stuck in a local solution by starting from a proper initial guess [88] (cf. Sec. A.4 in the appendix).

Basis change The χ -matrix depends on the chosen operator basis. The following statement describes the change of a general $(d^2 \times d^2)$ χ -matrix under basis transformations: Let χ be the process matrix in the $\{B_m\}$ basis and χ' be the process matrix in the $\{A_m\}$ basis respectively. Then the transformation yields $\chi'_{mn} = \bar{\lambda}_{mn} \chi_{mn}$ where $\bar{\lambda}_{mn}$ is the arithmetic or geometric mean of the eigenvalues of the matrix $M_m M_n^\dagger$ with $M_k = A_k^{-1} B_k$. The proof can be found in Sec. A.3 the appendix.

Single qubit QPT For the single qubit case, we have $d^2 = 4$ and we choose the basis $\{I, \hat{\sigma}_x, -i\hat{\sigma}_y, \hat{\sigma}_z\}$ [12]. We need 4 distinct input states and we choose [12] $|g\rangle, |e\rangle, |+\rangle \equiv (|g\rangle + |e\rangle)/\sqrt{2}$ and $|-\rangle \equiv (|g\rangle + i|e\rangle)/\sqrt{2}$, which are simple in experimental realization. The quantum process \mathcal{E} is applied to each of these states. The states and the outcomes $\mathcal{E}(|g\rangle\langle g|)$, $\mathcal{E}(|e\rangle\langle e|)$, $\mathcal{E}(|+\rangle\langle +|)$ and $\mathcal{E}(|-\rangle\langle -|)$ are reconstructed using QST. The calculation is simplified if we use the states $\rho_1 = |g\rangle\langle g|$, $\rho_2 = |g\rangle\langle e|$, $\rho_3 = |e\rangle\langle g|$ and $\rho_4 = |e\rangle\langle e|$ as input. These ρ_i are often referred to as the ‘‘computational basis states’’. We reconstruct the process using $\mathcal{E}(\rho_i) = \rho'_i$ [12], where each computational basis state ρ_i is mapped to the yet unknown state ρ'_i by \mathcal{E} , respectively. The transformation from the chosen input states to the computational basis states reads

$$\rho'_1 = \mathcal{E}(|g\rangle\langle g|) \quad (2.41)$$

$$\rho'_2 = \mathcal{E}(|+\rangle\langle +|) + i\mathcal{E}(|-\rangle\langle -|) - \frac{(1+i)}{2}(\mathcal{E}(|g\rangle\langle g|) + \mathcal{E}(|e\rangle\langle e|)) \quad (2.42)$$

$$\rho'_3 = \mathcal{E}(|+\rangle\langle +|) - i\mathcal{E}(|-\rangle\langle -|) - \frac{(1-i)}{2}(\mathcal{E}(|g\rangle\langle g|) + \mathcal{E}(|e\rangle\langle e|)) \quad (2.43)$$

$$\rho'_4 = \mathcal{E}(|e\rangle\langle e|). \quad (2.44)$$

We state that $\beta = \Lambda \otimes \Lambda$ with

$$\Lambda = \frac{1}{2} \begin{pmatrix} I & \hat{\sigma}_x \\ \hat{\sigma}_x & -I \end{pmatrix} \quad (2.45)$$

and obtain a closed expression for χ [12]

$$\chi = \Lambda \cdot \begin{pmatrix} \rho'_1 & \rho'_2 \\ \rho'_3 & \rho'_4 \end{pmatrix} \cdot \Lambda. \quad (2.46)$$

² $\|X\|_F = \sqrt{\text{Tr}(X^\dagger X)} = \sqrt{\sum_{i,j} (X_{ij})^2}$

We can obtain the Kraus operators as described for the general case, from which we can reconstruct the Bloch sphere after the process using Eq. (2.27) and Eq. (2.28). We give a schematic description of single qubit QPT in Fig. 2.15. The experimental implementation of QPT is straightforward, however, it can be shown that in order to reconstruct a QP on a d -dimensional system, we need at least $d^4 - d^2$ projective measurements [94]. The number of measurements grows very fast, as for a single qubit, we require 12 projections, but for QPT on two qubits, 240 measurements are required. In practice, the MLE requires additional averaging n_a for each measurement. Characterizing the initial states requires an additional factor of 2, which increases the amount of operations to $2n_a(d^4 - d^2)$. For a system with n_q qubits, we have $d = 2^{n_q}$, hence QPT shows a complexity of $\mathcal{O}(n_a e^{4n_q \ln 2})$ scaling exponentially with the number of qubits [12, 38]. This means the method may become impractical for large qubit systems. Another disadvantage of QPT is that the process is treated as a black box [14], which means that we can only compare input with output, knowing nothing about the time evolution of the system during the process. In order to get access to the system's dynamics, we need to apply a master equation approach [88, 95, 96] as described in Sec. 2.5.

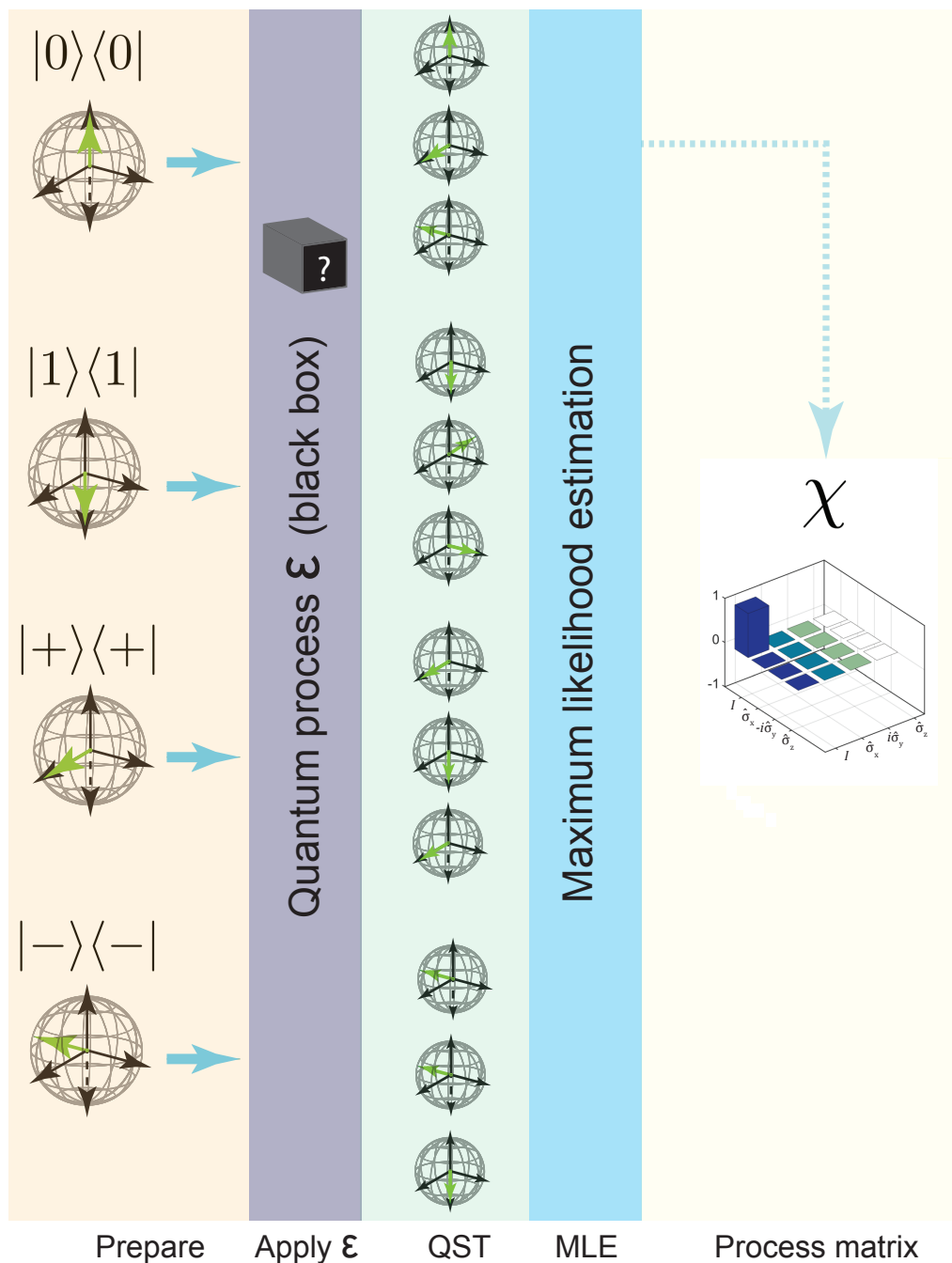


Figure 2.15: Illustration of single qubit QPT for the identity process. Four independent input states are prepared, after that, the quantum process is applied to each input state. The resulting output states are reconstructed using QST. This gives access to the raw process matrix. The physical process matrix is then calculated with an MLE.

2.4 Characterizing QST and QPT

For benchmarking our QST and QPT protocols, we need certain measures on the space of density matrices that quantify the distance between two quantum states [87]. This mathematical

tool can then be used to compare tomography results with the ideal predicted outcome. Thus, we obtain access to omnipresent errors caused by decoherence and avoidable errors such as inaccurate state preparation. The Choi-Jamiolkowski isomorphism described in Sec. 2.3.1 allows us to generalize these distance measures also for QP's [86]. If the process matrix χ is expressed in the basis of the computational basis states, the isomorphism yields $\rho_{\mathcal{E}} = \chi/2$ [87]. We further derive distance limits that can be used as an indicator whether our protocol is dominated by decoherence processes. We introduce the loyalty as a measure for the randomness of our protocol.

2.4.1 Distance measures

Within this thesis, we make use of the intuitive trace distance [12] and the less intuitive, but commonly used fidelity [97]. In contrast to the trace distance, the fidelity is not a metric on the space of quantum states, but it directly yields several metrics. As a general measure for the distance between two QP's, we introduce the diamond norm [98] and derive an explicit expression that allows us to calculate this norm for our quantum memory protocol.

Trace distance The trace distance between two quantum states ρ_1 and ρ_2 is defined as

$$D(\rho_1, \rho_2) = \frac{1}{2} \text{Tr}|\rho_1 - \rho_2| = \frac{1}{2} \|\rho_1 - \rho_2\|_1 \quad (2.47)$$

where $|X| \equiv \sqrt{X^\dagger X}$. $\|X\|_1 \equiv \text{Tr}|X|$ is called the trace norm. $D(\rho_1, \rho_2)$ fulfills the requirements for a metric on the space of density matrices. This implies especially that $D(\rho_1, \rho_2) = 0$ if and only if $\rho_1 = \rho_2$. Furthermore, $D(\rho_1, \rho_2)$ is invariant under unitary transformations and $D(\mathcal{E}(\rho_1), \mathcal{E}(\rho_2)) \leq D(\rho_1, \rho_2)$ for any physically valid quantum process \mathcal{E} . This especially denies the existence of quantum processes that increase the distinguishability of two quantum states [87]. There are two important interpretations of the trace distance. We consider a single qubit system and define \mathbf{a}_1 as the Bloch vector for ρ_1 and \mathbf{a}_2 as the Bloch vector for ρ_2 . The trace distance between the states then obeys the relation [12]

$$D(\rho_1, \rho_2) = \frac{1}{2} |\mathbf{a}_1 - \mathbf{a}_2| \quad (2.48)$$

which is just half the Euclidian distance of the corresponding Bloch vectors, as depicted in Fig. 2.16. Another interpretation of the trace distance is based on the distinguishability of two quantum states. A measurement with outcomes “1” or “2” is performed and we state that the system is in ρ_1 for “1” and in state ρ_2 for “2”. The probability p that our guess is correct is then given by [12, 87]

$$p = \frac{1}{2} [1 + D(\rho_1, \rho_2)]. \quad (2.49)$$

This means that the trace distance can be regarded as a measure on how well we can discern ρ_1 and ρ_2 using measurement outcomes.

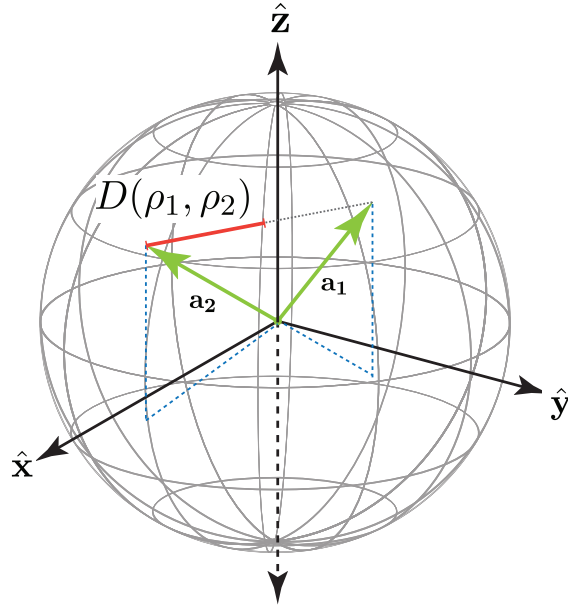


Figure 2.16: Bloch sphere representation for two qubit states ρ_1 and ρ_2 . The trace distance is given by half the Euclidean distance of the Bloch vectors

Fidelity A second and widely used measure for comparing two quantum states ρ_1 and ρ_2 is the fidelity f [97]. For our purposes, f is defined as [12]

$$f(\rho_1, \rho_2) \equiv \text{Tr} \sqrt{\sqrt{\rho_1} \rho_2 \sqrt{\rho_1}}. \quad (2.50)$$

The cyclicity of the trace implies that $f(\rho_1, \rho_2)$ is invariant under unitary transformations. Furthermore, it can be shown that $0 \leq f(\rho_1, \rho_2) \leq 1$ and that $f(\rho_1, \rho_2) = 1$ if and only if $\rho_1 = \rho_2$. $f(\rho_1, \rho_2)$ can be seen as a “monotonically increasing” function with respect to the deviation of ρ_1 from ρ_2 . Moreover, the fidelity obeys $f(\rho_1, \rho_2) = f(\rho_2, \rho_1)$. For the single qubit case, it can be derived that [68]

$$f(\rho_1, \rho_2) = \sqrt{\text{Tr}(\rho_1 \rho_2) + 2 \sqrt{\det(\rho_1) \det(\rho_2)}} \quad (2.51)$$

which simplifies the practical evaluation of the fidelity. In some cases, we prefer using the infidelity $1 - f(\rho_1, \rho_2)$ [99], since it equals zero if and only if $\rho_1 = \rho_2$, which is also the case for the other distance measures which we use in this thesis. In contrast to the trace distance, the fidelity only has physical interpretation if one of the states is pure. Consider the pure state $|\Psi\rangle\langle\Psi|$ and an arbitrary state ρ , which might be an imperfect experimental implementation of $|\Psi\rangle\langle\Psi|$. The fidelity then reduces to $f(|\psi\rangle\langle\psi|, \rho) = \sqrt{\langle\psi|\rho|\psi\rangle}$ [87], directly measuring the state overlap. $f(\rho_1, \rho_2)$ does not satisfy the requirements to be a metric [87]. However, we can use the fidelity to define the commonly used Bures distance [88, 100]

$$B(\rho_1, \rho_2) \equiv \sqrt{2(1 - f(\rho_1, \rho_2))}. \quad (2.52)$$

For pure states, the Bures metric equals their Euclidian distance [87]. A metric directly related to quantum computing is given by the \mathcal{C} -distance [87, 88]

$$\mathcal{C}(\rho_1, \rho_2) \equiv \sqrt{1 - f(\rho_1, \rho_2)^2}. \quad (2.53)$$

If we use the computational basis states as an operator basis for the process and consider that we want to evaluate a function $f(x)$ (e.g. factoring) using a quantum operation $\mathcal{E}(|x\rangle\langle x|)$, and $\mathcal{E}_{\text{id}}(|x\rangle\langle x|)$ denotes the ideal process which succeeds in evaluating $f(x)$ with probability one, the average probability p that \mathcal{E} fails obeys $p \leq \mathcal{C}(\rho_{\mathcal{E}}, \rho_{\mathcal{E}_{\text{id}}})^2$ [87].

Diamond norm In quantum information, a frequently used measure for the distance between two quantum processes \mathcal{E}_1 and \mathcal{E}_2 is the diamond norm [98] which is defined as [101]

$$\|\mathcal{E}_1 - \mathcal{E}_2\|_{\diamond} \equiv \sup_{\rho} \|(\mathcal{E}_1 \otimes I_k)(\rho) - (\mathcal{E}_2 \otimes I_k)(\rho)\|_1. \quad (2.54)$$

Where I_k is the identity for a k -dimensional state space. In contrast to the previously discussed metrics, which allow to assert average properties of the quantum process (cf. average overlaps, average probabilities), the fact that we take the supremum in Eq. (2.54) enables us to perform worst case estimations [87]. Intuitively, the diamond norm generalizes the trace norm by applying \mathcal{E} to systems of arbitrary large dimension and taking its maximum value. The additional k -dimensional part can be regarded as an ancilla for the system and we maximize over all states $\rho = \rho_{\text{system}} \otimes \rho_{\text{ancilla}}$. Although Eq. (2.54) is not practical for direct evaluation, we can derive a simple expression for the case of a quantum memory if we express \mathcal{E} in the Pauli basis $\{I, \hat{\sigma}_x, \hat{\sigma}_y, \hat{\sigma}_z\}$. We exploit the fact that the ideal memory process \mathcal{E}_{id} is an identity. In this case, the diamond norm can be calculated as

$$\|\mathcal{E}_{\text{id}} - \mathcal{E}\|_{\diamond} = \sqrt{\text{Tr}(\chi^2) - (\chi^2)_{11}} = \|P\chi\|_F \quad (2.55)$$

where \mathcal{E} denotes the non-ideal reconstructed process, χ is the measured process matrix and $P \equiv \text{diag}(0,1,1,1)$ is a projector (cf. Sec. B.1 in the appendix). We use the convention that we calculate the trace distance, the fidelity and the resulting metrics in the basis $\{I, \hat{\sigma}_x, -i\hat{\sigma}_y, \hat{\sigma}_z\}$ and the diamond norm in the Pauli basis.

2.4.2 Distance limits

In this section, we derive some specific values of the previously discussed distance measures for our quantum memory process. To this end, we gain a better intuition for the quality of our process. Since our distance measures are monotonic functions of our process quality, we obtain limits by considering the CMS ρ_* for QST and the CDP \mathcal{E}_* for QPT. In the single qubit case, \mathcal{E}_* maps every initial quantum state ρ to the center of the Bloch sphere. For a d -dimensional quantum system, we have $\rho_* = 1/d \cdot I_d$ and $\chi_* = 1/d^2 \cdot I_{d^2}$ for the process matrix of \mathcal{E}_* ³. If we

³ I_d and I_{d^2} denote the identity matrix of dimension d and d^2 respectively

aim for reconstructing a pure state ρ_p , we can compare it to ρ_* and obtain

$$f(\rho_p, \rho_*) = \frac{1}{\sqrt{d}}. \quad (2.56)$$

This is obvious for $\rho_p = |g\rangle\langle g|$ and holds for arbitrary pure states [68]. For the single qubit state, this can be intuitively understood by the spherical symmetry of the Bloch sphere. We state that our tomography procedure only makes sense if we measure a fidelity above this limit. If χ_{id} is the process matrix for the identity process, we obtain a similar limit for our memory protocol:

$$f(\chi_{\text{id}}, \chi_*) = \frac{1}{d}. \quad (2.57)$$

Thus, if we measure a process fidelity $f(\chi_{\text{id}}, \chi_*) \leq 1/d$, our reconstructed process is dominated by decoherence, assuming that there are no avoidable errors such as inaccurate state preparation. A similar discussion can be performed for the other distance measures discussed in Sec. 2.4.1. We derive upper limits for our distance measures in a way that values above this bound indicate that our process does not provide any value compared to \mathcal{E}_* . For the single qubit case, these limits can be derived in a straightforward way using the expressions from the last section. The results for both QST and QPT are listed in Tab. 2.1

Distance measure	d	$d = 2$	$d = 4$
Trace distance	$1 - 1/d$	$1/2$	$3/4$
1-Fidelity	$1 - 1/\sqrt{d}$	$1 - 1/\sqrt{2} \simeq 0.293$	$1/2$
Bures-metric	$\sqrt{2}(1 - 1/\sqrt{d})^{1/2}$	$\sqrt{2} - \sqrt{2} \simeq 0.765$	1
\mathcal{C} -metric	$\sqrt{1 - 1/d}$	$1/\sqrt{2} \simeq 0.707$	$\sqrt{3}/2 \simeq 0.866$
Diamond norm	$\sqrt{d-1}/d$	$1/2$	$\sqrt{3}/4 \simeq 0.433$

Table 2.1: Theoretical distance limits for QST and QPT

2.4.3 Loyalty

If we take a set of randomly chosen pure or mixed state for a d -dimensional quantum system and compare it to the CMS, we obtain an average fidelity of [68, 102, 103]

$$\langle f \rangle = \sqrt{2} \frac{\Gamma(5/4)}{\Gamma(3/4)\Gamma(5/2)} + \mathcal{O}(1/d^{3/2}) = \frac{2\sqrt{2}G}{3} + \mathcal{O}(1/d^{3/2}) \quad (2.58)$$

where $G = 0.834\dots$ is Gauss's constant. The underlying assumption is that the states are distributed according to the Bures measure [104]. This means that the average fidelity takes the limit $\langle f \rangle = 0.787$ for $d \rightarrow \infty$. If we measure the process χ matrix for the memory process for multiple times and compare each outcome to χ_* , we obtain a measure on whether our protocol produces "random" or well-defined outcomes. For single qubit processes, we have $d = 4$, hence we can assume that the error in Eq. (2.58) is lower than $1/4^{3/2} = 12.5\%$, this method is not very accurate for such a system. However, it is well suited for systems with multiple qubits, since the

deviation from the limit value decreases with $\mathcal{O}(1/8^{n_q})$ where n_q is the number of qubits. We calculate the corrected fidelity f_*^c of the process matrix with the χ_* -matrix for the CDP and define the loyalty ξ of the protocol as

$$\xi \equiv \lim_{N \rightarrow \infty} \left| \frac{1}{N} \sum_{i=1}^N f_{*i}^c - \frac{2\sqrt{2}G}{3} \right|. \quad (2.59)$$

We approximate this number by increasing the number of measurements N . If ξ is bigger than a certain tolerance ε , we conclude that the protocol returns non-random output values. We choose ε of the magnitude $\mathcal{O}(1/d^{\frac{3}{2}})$, which means 10% in our case.

2.5 Quantum master equations

For an ideal quantum system, the dynamical behavior is described by the Schrödinger equation [11], which is suited for calculating the unitary time evolution of pure states for our system. However, for a realistic system there are non-unitary contributions [14], such as energy relaxation and dephasing, induced, e.g., by spontaneous emission, (electronic) noise contributions, the Purcell effect [105] or, in general, due to coupling to the environment. This means that we have to consider $\rho = \rho_{\text{sys}} \otimes \rho_{\text{env}}$ on a Hilbert space $\mathcal{H} = \mathcal{H}_{\text{sys}} \otimes \mathcal{H}_{\text{env}}$ where “sys” denotes our quantum system and “env” the environment. Throughout this whole thesis, we assume Markovian behavior and when applying the Born-Markov approximation [106], we obtain the Lindblad master equation for the system [95]

$$\frac{d\rho}{dt} = \underbrace{-\frac{i}{\hbar}[\hat{H}, \rho]}_{\text{Unitary}} + \underbrace{\sum_{j=1}^{d^2-1} \left(2\hat{L}_j \rho \hat{L}_j^\dagger - \{\hat{L}_j^\dagger \hat{L}_j, \rho\} \right)}_{\text{Non-Unitary}} \quad (2.60)$$

where $\{\cdot, \cdot\}$ denotes the anticommutator. The Lindblad operators \hat{L}_j describe the time evolution that lead to CMS's, and the Lindblad term yields a loss of the “quantumness” of our system on large timescales. If the Lindblad term vanishes, Eq. (2.60) reduces to the von Neumann equation [11], which is equivalent to the Schrödinger equation. We use Eq. (2.60) in order to simulate our quantum memory protocol. The T_1 -decay is modelled as annihilation of excitations with decay rate $\gamma_1 = 2\pi/T_1$, which yields the Lindblad operator $\hat{L}_1 = \sqrt{\gamma_1} \hat{\sigma}^-$ [12]. We model dephasing as rotation about the z -axis with rate $\gamma_\varphi = 2\pi/T_\varphi$ [107] leading to $\hat{L}_\varphi = \sqrt{\gamma_\varphi} \hat{\sigma}_z$. We reshape ρ into a column vector $\boldsymbol{\rho} \equiv (\rho_{11}, \rho_{12}, \rho_{21}, \rho_{22})^T$ and rewrite Eq. (2.60) as an ordinary differential equations (ODE) system

$$\dot{\boldsymbol{\rho}} = \left(-\frac{i}{\hbar} \hat{\mathcal{H}} + \hat{\mathcal{L}} \right) \cdot \boldsymbol{\rho} \quad (2.61)$$

which can be solved numerically. For the driven qubit including energy relaxation and dephasing, we obtain (cf. Chap. D in the appendix)

$$\mathcal{H} = \frac{\hbar\Omega_d}{2} \begin{pmatrix} 0 & i \cos \varphi_d - \sin \varphi_d & -i \cos \varphi_d - \sin \varphi_d & 0 \\ i \cos \varphi_d - \sin \varphi_d & -2i \frac{\delta}{\Omega_d} & 0 & -i \cos \varphi_d - \sin \varphi_d \\ -i \cos \varphi_d + \sin \varphi_d & 0 & 2i \frac{\delta}{\Omega_d} & i \cos \varphi_d - \sin \varphi_d \\ 0 & -i \cos \varphi_d + \sin \varphi_d & i \cos \varphi_d + \sin \varphi_d & 0 \end{pmatrix} \quad (2.62)$$

and

$$\hat{\mathcal{L}} = \begin{pmatrix} 0 & 0 & 0 & 2\gamma_1 \\ 0 & -4\gamma_\varphi - \gamma_1 & 0 & 0 \\ 0 & 0 & -4\gamma_\varphi - \gamma_1 & 0 \\ 0 & 0 & 0 & -2\gamma_1 \end{pmatrix}. \quad (2.63)$$

Given the initial state of our system, Eq. (2.61) describes the time evolution of our system including dissipative effects.

2.6 Quantum memory theory

Within this section, we describe how we can use a long-lived resonator mode [35] as a quantum memory for our qubit. We discuss the theoretical concepts and ideas behind the experiment, which were also realized using 2D transmission line resonators [36].

Injection of the microwave signals We drive the microwave field in the cavity with two antennas, and the decay rate of the electric field sensitively increases with the dipolar coupling strength of the mode to the antennas, $\kappa_{\text{ext}} \propto \mathbf{p} \cdot \mathbf{E}(x, y, z)$. If we assume that the antenna points in the y -direction, the external decay rate κ_{ext} of mode (cf. Fig 2.5) reads [108]

$$\kappa_{\text{ext}} = \frac{C_x}{\hbar} \left(\int_{-\infty}^{l_a} E_{\parallel, a}(x, y, z) dy \right)^2 \quad (2.64)$$

with the parallel electric field $E_{\parallel, a}$, the antenna length l_a and the coupling capacitance C_x . Figure 2.17 shows the result of a finite element (FEM) simulation for the TE101, the TE201 and the TE102 modes of the cavity.

Antenna positioning The cavity is physically described as a harmonic quantum oscillator with a multimode structure. For the readout mode (ROM), a good assumption is $E_{\parallel, a}(y) = E_0 / (\exp(y/r) + 1)$ with a suitable constant r , which depends on the arperature, and we obtain [108]

$$\kappa_{101, \text{ext}} = \frac{C_x E_0^2 r^2}{\hbar} \ln^2 \left(e^{\frac{l_a}{r}} + 1 \right). \quad (2.65)$$

The antennas are placed in a way that their position matches with the node of the TE201 mode, suppressing decay induced by coupling to the antennas. If we assume that we have linear field dependence close to the node, with vanishing field exactly at the node position, we obtain

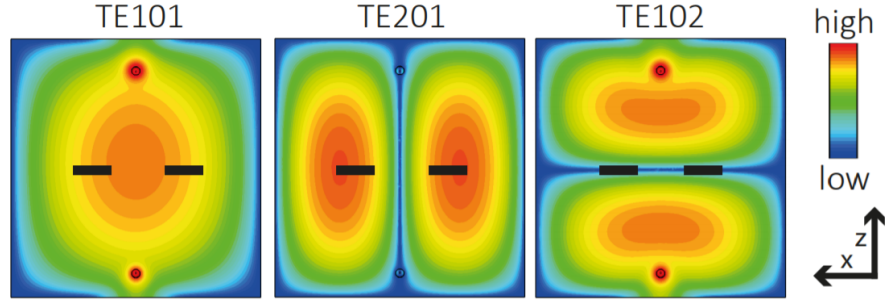


Figure 2.17: FEM simulation of the TE101, the TE201 and the TE102 mode. The black bars denote the qubit position. The antenna position is denoted by the circles on the top and the bottom. The antenna is placed in a way that the TE201 mode does not couple, whereas we have strong coupling to the TE101 mode. We place the qubit in the node of the TE102 mode, implying that this mode does not couple at all. Figure taken with friendly permission from E. Xie [108]

$\kappa_{201,\text{ext}} \propto r_a^2 l_a^2$ indicating that we have sensitive dependence on the antenna radius r_a and the antenna length l_a . We still maintain strong coupling to the qubit for the TE201 mode. Due to $\kappa_{101,\text{ext}} \gg \kappa_{201,\text{ext}}$, we expect a significantly longer lifetime for the TE201 mode, which we call the storage time T_s in the following.

Qubit positioning We place the qubit and the antennas close to the antinode of the TE101 mode, which means we have strong qubit coupling to this mode and simultaneously fast decay. Thus, this mode is suitable for fast qubit readout, hence we call it readout mode (ROM) in the following. We call the TE201 mode the “storage mode” (SM) [35].⁴ If we manage to engineer

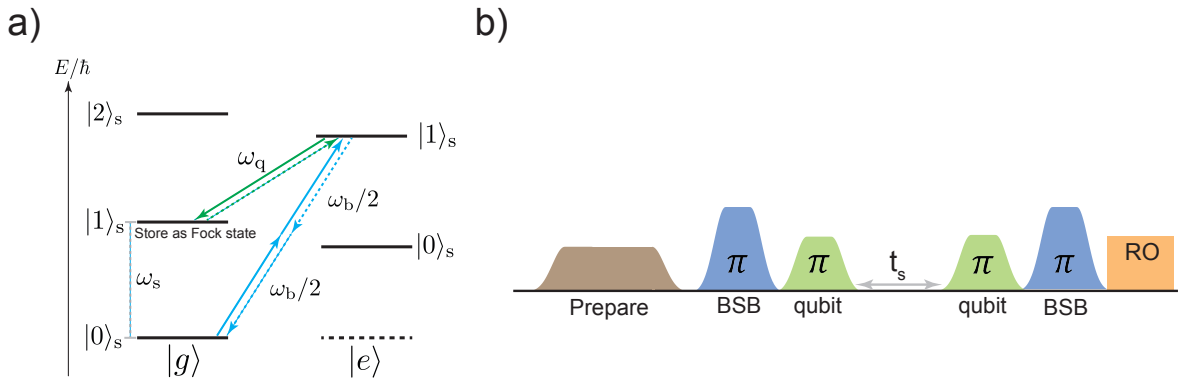


Figure 2.18: a) Energy levels for the Jaynes-Cummings model. Starting from $|g0\rangle$ the BSB transition (straight blue line) is induced as a second order process. After that, the qubit is deexcited (straight green line). As a result, $|g\rangle$ is stored as Fock state $|1\rangle_s$ in the cavity mode. The stored qubit state is retrieved by driving transitions in a reversed order (blue and green dashed lines). b) Pulse sequence for the quantum memory. The first pulse prepares the state to be stored. The state is stored by driving the BSB transition and finally flipping the qubit population. After a waiting time t_s , the reverted pulse scheme is applied to retrieve the stored state. The ROM is pulsed in order to measure the qubit population.

the system in a way that $T_s \gg T_1$, where T_1 denotes the decay time of the qubit, we are able to significantly enhance the decay time of the information encoded in the qubit by transferring it into the storage mode as a superposition of Fock states [108]. For these purposes, we reconsider the Jaynes-Cummings energy scheme from Fig. 2.7 and drive the transitions depicted in Fig. 2.18 a). This is realized with the pulse sequence depicted in Fig. 2.18 b). In the following, we discuss the effect of this protocol. We assume that we are initially in state $|g0\rangle$. The first π -pulse with frequency $\omega_b/2$ drives the BSB with a two photon process simultaneously exciting qubit and resonator, yielding $|g0\rangle \rightarrow |e1\rangle$ [78]. The second π -pulse with frequency ω_q deexcites the qubit, which implies $|e1\rangle \rightarrow |g1\rangle$. This means that in the ideal case, we store the ground state of the qubit as Fock state $|1\rangle_s$ in the cavity. We observe that if the qubit is initially in $|e\rangle$, the drive on the BSB transition has no effect, hence we keep Fock state $|0\rangle_s$. The third and the fourth pulse in Fig. 2.18 b) revert the procedure described above, which enables us to retrieve the qubit state back from the SM. For an arbitrary superposition state characterized by the coefficients a and b , the effect of the quantum memory protocol, neglecting decoherence, can be summarized as follows:

$$a|g\rangle + b|e\rangle \xrightarrow{\text{Transfer to SM}} a|1\rangle_s + b|0\rangle_s \longrightarrow \text{Store for time } t_s \xrightarrow{\text{Retrieve}} a|g\rangle + b|e\rangle \quad (2.66)$$

The memory enhancement then results from the fact that $a|g\rangle + b|e\rangle$ decays on a timescale T_1 , whereas $a|1\rangle_s + b|0\rangle_s$ decays with a decay time $T_s \gg T_1$.

⁴The qubit is positioned in a way that the TE102 mode, which can be regarded as a “twin” mode of TE201, does not couple to the qubit.

Chapter 3

Setup and experimental techniques

In order to realize the theoretical concepts of our quantum memory architecture described in Sec. 2.6, we need a high-Q 3D cavity resonator and a suitable transmon qubit. In order to avoid thermal photons in the cavity and thermal qubit excitations, we need to perform our experiments at millikelvin temperatures. This will be further explained in the second section, which deals with the cryogenic setup. We discuss the time domain microwave setup and explain how we manipulate our quantum system with microwave pulses. We point out how we engineer the shape of the control pulses and discuss the advantages and disadvantages of different pulse shapes. Subsequently, we characterize our qubit-resonator system in the third section, and we briefly discuss the procedures and protocols that are necessary to measure the coupling and decay constants of the qubit. We realize the quantum memory protocol in the fourth section and measure the respective decay times.

3.1 Sample description

Within this section, we give details on the design of cavity and the transmon qubit. For our experiment, we use a cavity milled from aluminum with an Al purity of 99.5% [109]. The cavity is engineered in a way that the frequency $\nu_{101} = \omega_{101}/2\pi$ of the ROM is compatible with the microwave setup [108]. We are especially limited by the bandwidth (4 – 8 GHz) of the cryogenic high electron mobility transistor (HEMT) amplifiers. The technical drawing in Fig. 3.1 illustrates the cavity design, and the dimensions are chosen in a way that $\nu_{101} \simeq 5.6$ GHz. In order to enhance the external Q -factor, a 0.1 mm Au wire serves as an antenna. In practice, we achieve a loaded Q factor of $Q_L \simeq 3.7 \cdot 10^5$ [108].

The transmon qubit is fabricated onto an Si chip (6 mm \times 10 mm \times 0.52 mm) and fixed with indium, improving thermalization. Our single-junction transmon qubit sample has the dimensions $l_C = 355 \mu\text{m}$, $w_q = 305 \mu\text{m}$ and a gap value of $g_q = 50 \mu\text{m}$ (cf. Fig. 2.6), yielding $C_\Sigma \simeq 105$ fF [108].

We measure a qubit frequency of $\omega_q/2\pi = 6.226$ GHz, yielding $I_c \simeq 52.8$ nA.

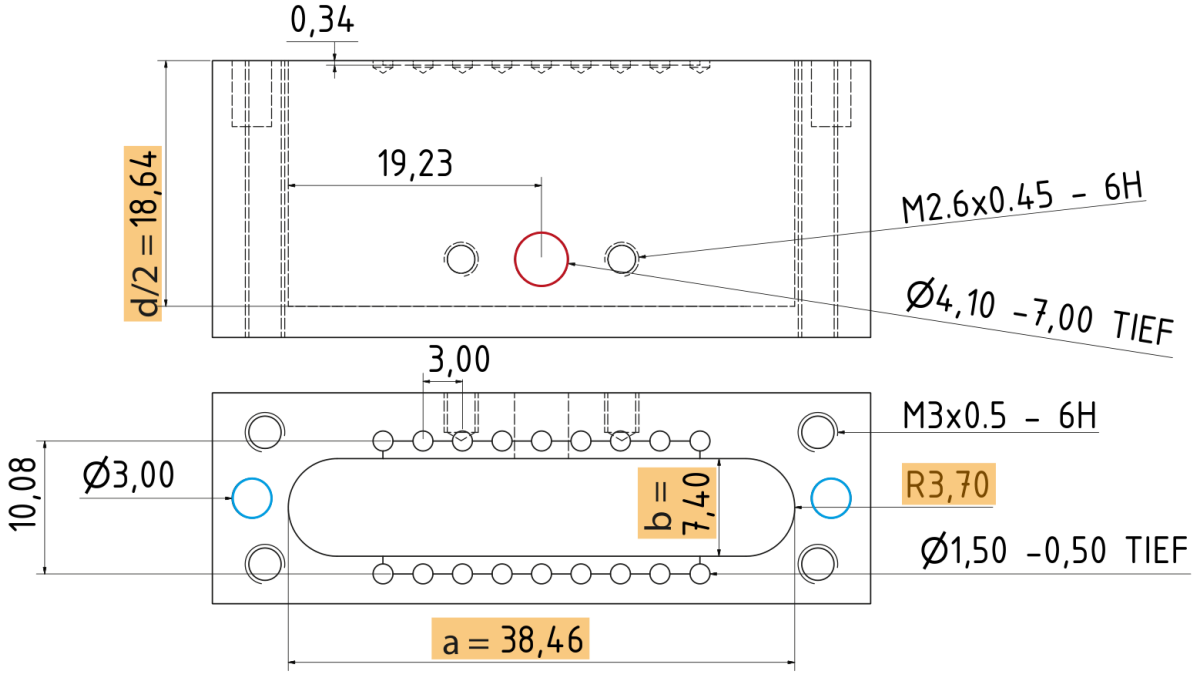


Figure 3.1: Technical drawing of one cavity half. The cavity has a length of $a = 38.46$ mm, a width of $d = 37.28$ mm and a total height of $b = 7.4$ mm. Figure taken with friendly permission from E. Xie [108].

3.2 Measurement setup

3.2.1 Cryogenic setup

We need $k_B T \ll \hbar \omega_q$ in order to prevent that the qubit gets thermally populated. We can fulfill these conditions by performing the experiments at temperatures below 100 mK. This is realized by mounting the cavity in a home built wet $^3\text{He}/^4\text{He}$ dilution refrigerator [110]. The detailed operation principle as well as the technical data of this machine is discussed in Ref. [111]. A picture of the inside of the cryostat, as well as an illustration of the cryogenic electronics is given in Fig. 3.2.

3.2.2 Room temperature setup

The quantum memory protocol requires time domain measurements. The complete time domain setup is depicted in Fig. 3.3 and explained in the following. In principle, a pulsed microwave setup consists of an RF source, which gives out a continuous microwave signal at a specific frequency and power, and an arbitrary waveform generator (AWG), which modulates a desired pulse envelope onto the microwave signal¹. However, in order to control the qubit phase φ , which is necessary for characterizing the whole Bloch sphere, we need an additional wideband IQ control [108]. The underlying working principle is explained in the following. In Sec. 2.2.2, we derive that the qubit phase φ in the xy -plane matches with the phase φ_d of the microwave drive in the rotating frame. We characterize the microwave signal $A \cos(\omega_d t + \varphi_d)$ into a 0°

¹We use Agilent 81160A AWG's

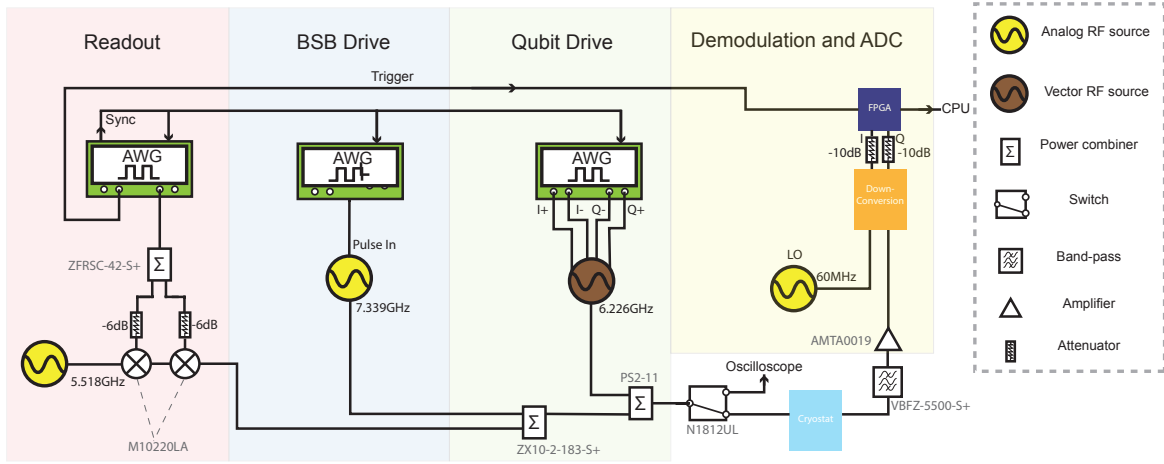


Figure 3.3: Schematic illustration of the time domain setup, consisting of a pulse generation part and a part responsible for down conversion and data acquisition. The BSB and the RO pulse are generated by analog RF sources. The on/off ratio of the RO source is modulated with two mixers that are controlled by an AWG. The BSB source is controlled by an AWG via the PulseIn port. For the qubit, a vector RF source with an external differential IQ input is used. I and Q are controlled with the two channels of an another AWG. The signal is converted to the IF regime using a local oscillator. The data is recorded and processed with an FPGA that is triggered by the RO AWG. The devices are synchronized with a frequency reference.

mixers that is controlled by an AWG. One mixer has an insertion loss of 7 dBm, and we use 2 mixers in order to push the on/off ratio to approximately 40 dBm. A 10 MHz reference⁶ serves for synchronization and pulse timing purposes. The pulsed drive signal leads to modifications of the qubit state, which are picked up by the RO pulse [111]. The RO signal is amplified by a HEMT amplifier before it is demodulated from GHz to MHz and then further processed by an FPGA-enhanced analog-to-digital converter card. Within each measurement cycle, we average over about 10^6 values. The FPGA then calculates the moments $\langle I^m Q^m \rangle$. For our experiment, we only need $\langle I \rangle$ and $\langle Q \rangle$ and we can use the second order moments for calculating the variance $\text{Var}(s) = \langle s^2 \rangle - \langle s \rangle^2$ and the standard deviation $\sigma = \sqrt{\text{Var}(s)}$. However, in practice, we estimate the standard deviation by repeating the experiment for 10-50 times from the respective first order moments. From $\langle I \rangle$ and $\langle Q \rangle$, we are able to calculate the amplitude and phase of the readout signal in order to draw conclusions on the qubit state.

3.2.3 Pulse shaping

The shape of the envelope of the control pulses is a crucial aspect regarding the fidelity of quantum operations [108]. The reason for that is the the sensitivity of the transmon to parasitic frequencies due to its low anharmonicity. Hence, we need narrow pulses in frequency space, which can be challenging for short pulses due to the Fourier reciprocity $\Delta t \propto 1/\Delta\omega$. The relation

⁶We use a Stanford Research FS725 atomic clock

between time- and frequency space is given by the Fourier transform [115]

$$P(t) \circ\text{---} \tilde{P}(\omega) = \frac{1}{\sqrt{2\pi}} \int_{-\infty}^{\infty} P(t) e^{-i\omega t} dt. \quad (3.2)$$

The simplest possible pulse shape is provided by rectangular pulses, which show the big advantage that the t_θ -time increases linearly with the pulse area A , $t_\theta \propto A \propto \tau$, yielding sinusoidal Rabi oscillations as a function of the pulse length τ . However, rectangular pulses follow a sinc-function in frequency space (cf. Fraunhofer diffraction [116]), $\text{rect}(t/\tau) \circ\text{---} \tau/\sqrt{2\pi} \cdot \text{sinc}(\tau\omega/2\pi)$. This gives an undesired broad frequency spectrum.

Another possibility is given by Gaussian pulses $P(t) = \exp(-t^2/2\tau^2\sigma^2)$. We also obtain a Gaussian shape in frequency space

$$P(t) \circ\text{---} \tilde{P}(\omega) = \frac{1}{\sqrt{2\pi}} \int_{-\infty}^{\infty} e^{-\frac{t^2}{2\sigma^2\tau^2} - i\omega t} dt = \sqrt{2}\sigma\tau e^{-\omega^2\tau^2\sigma^2} \quad (3.3)$$

which possesses a narrower frequency spectrum. The relative anharmonicity α_r of the qubit gives a constraint for the FWHM (full width half maximum) of the pulse length and for the pulse time: $\tau \geq 4\hbar \sqrt{\ln 2}/|\alpha_r|\omega_q\sigma$, implying that we have a lower bound for τ of the magnitude of nanoseconds for typical α_r . A big disadvantage of Gaussian pulses is that we have $A = \sqrt{\pi}\sigma\tau/2$, yielding longer pulses compared to rectangular pulses, implying that the qubit is affected more by depolarization in comparison with rectangular pulses. In order to combine the advantages of both pulse shapes, we define flat-top Gaussian pulses [108], which are rectangular pulses with a Gaussian ramp, as illustrated in Fig. 3.4 a). If t_r denotes the ramp time, we distinguish $\tau \leq 2t_r$

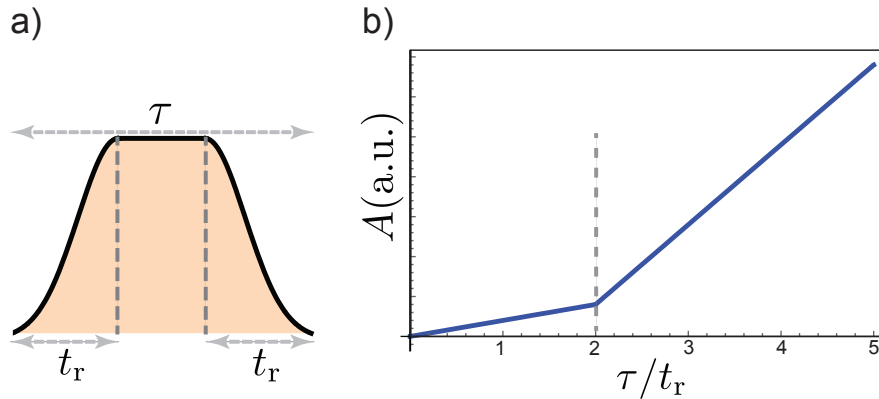


Figure 3.4: a) Flat-top Gaussian pulse envelope with pulse length τ and ramp time t_r . b) Pulse area dependig on the pulse length. For $\tau > 2t_r$, the pulse area increases faster with τ than for $\tau < 2t_r$, resulting in a kink at $\tau = 2t_r$

and $\tau > 2t_r$. In the first case, we choose a Gaussian pulse, since the total pulse length is not

sufficient for the given ramp up and ramp down time. In the second case, we define

$$P(t) = \begin{cases} e^{-\left(\frac{t-t_r}{2\sigma t_r}\right)^2} & \text{if } 0 \leq t \leq t_r, \\ 1 & \text{if } t_r \leq t \leq \tau - t_r, \\ e^{-\left(\frac{t-\tau-t_r}{2\sigma t_r}\right)^2} & \text{if } \tau - t_r \leq t \leq \tau \\ 0 & \text{else} \end{cases}. \quad (3.4)$$

Due to the fact that we smooth the edges of the rectangular pulse, the pulses are much narrower in the frequency domain. A minor drawback of this technique is that we obtain a discontinuous function of the pulse length and the pulse area

$$A(\tau) = \begin{cases} \sqrt{\pi} \cdot \operatorname{erf}\left(\frac{1}{2\sigma}\right)\sigma\tau & \text{if } 0 \leq \tau \leq 2t_r \\ 2(\sqrt{\pi}\sigma \cdot \operatorname{erf}\left(\frac{1}{2\sigma}\right) - 1)t_r + \tau & \text{if } 2t_r \leq \tau \end{cases}. \quad (3.5)$$

This is exemplary depicted in Fig. 3.4 (b) and implies that we have a lower Rabi frequency for $\tau < 2t_r$ and hence $2t_{\pi/2} \neq t_\pi$. We can try to choose σ in a way that the kink vanishes. This requires $\operatorname{erf}(x) = 2x\sqrt{\pi}$ with $x \equiv 1/2\sigma$, which has the only solution $x = 0$, which means σ has to be infinitely large, giving an infinitely large slope. It is not possible to “smooth” the curve in Fig. 3.4 b) for an arbitrarily smooth ramp $f(t)$ since this requires $f(t) = 1$, which is a contradiction. In practice, we choose $t_r = 20$ ns and $\sigma = 0.2$, and estimate $t_{\pi/2} = t_\pi/2 + t_r(1 - \sqrt{\pi}\sigma)$, which yields

$$t_{\pi/2}[\mu\text{s}] = \frac{t_\pi[\mu\text{s}]}{2} + 0.0129. \quad (3.6)$$

As a consequence, we need to take into account the deviation in pulse lengths for π - and $\pi/2$ -pulses.

3.3 Qubit characterization

In this section, we explain step by step how we can get experimental access to all the relevant parameters of the qubit and the resonator. We work through a characterization strategy protocol that is capable of determining these quantities [108]. First of all, we measure the cavity transmission with a vector network analyzer (VNA) [117]⁷ and sweep the drive frequency ω . We obtain a Lorentzian profile for the transmission amplitude $P(\omega)$ and an arctan profile for the transmission phase $\varphi(\omega)$ near the cavity transmission frequency $\omega_0/2\pi = 5.519$ GHz [70]

$$P(\omega) = \frac{1}{2} \left(\frac{G}{1+G} \right)^2 \frac{\kappa/2}{(\omega - \omega_0) + (\kappa/2)^2} \quad \varphi(\omega) = -\arctan(2/\kappa(\omega - \omega_0)). \quad (3.7)$$

Here, G is a measure for the external cavity coupling strength. The results of the transmission measurement are depicted in Fig. 3.5. As explained in Sec. 2.2.1, the AC-Stark shift modulates the cavity resonance frequency depending on the qubit state. Hence, we can determine the dispersive shift χ by considering the shift of the transmission peak [52]. We perform frequency

⁷We use a Rhode & Schwarz ZVA8 with 2 ports

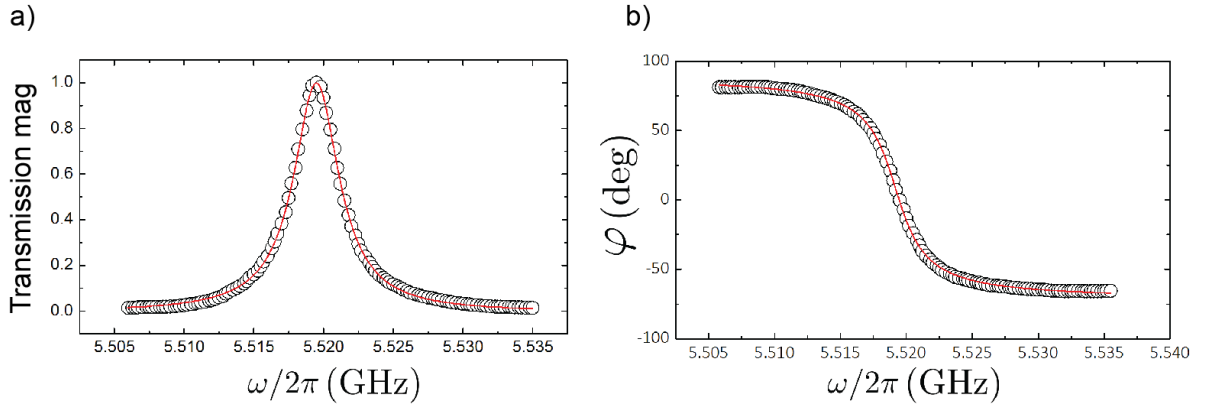


Figure 3.5: a) Transmission amplitude of the cavity. We observe a Lorentzian profile and measure a transmission peak at $\omega_0/2\pi = 5.519$ GHz b) Readout phase for a transmission measurement. The data points follow an arctan-function. $\varphi = 0$ corresponds to the cavity resonance frequency $\omega_0/2\pi$

sweeps around the cavity resonance frequency and simultaneously sweep the drive power. The results are shown in Fig. 3.6. For low powers, the qubit has negligible $|e\rangle$ state population,

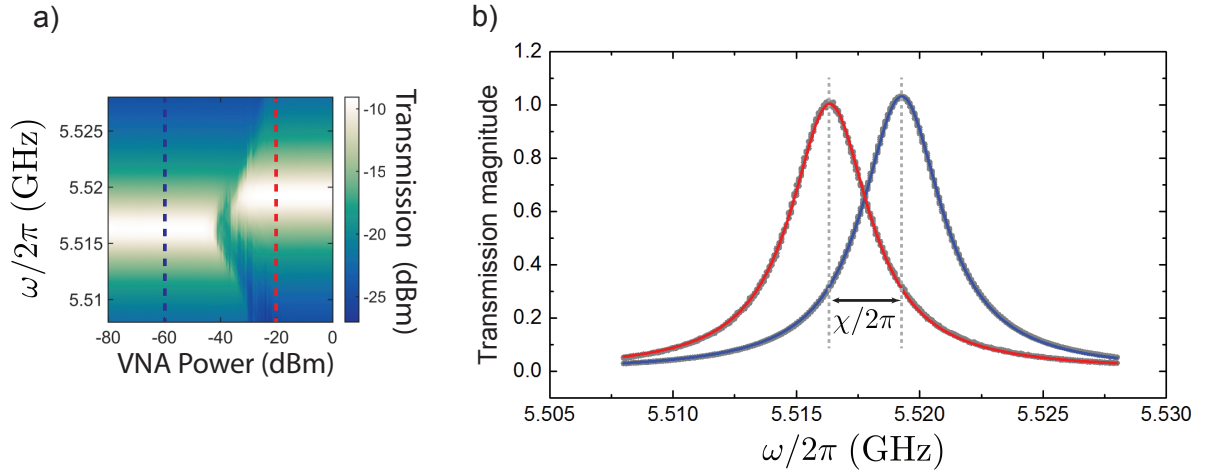


Figure 3.6: a) Transmission magnitude depending on the drive frequency and the drive power, measured with a VNA. At a VNA power of about -40 dBm, the transmission peak shifts. b) Dispersive shift for the RO phase b) Transmission peak for -60 dBm (blue) and for -20 dBm (red). The peaks are separated by $\chi/2\pi$

whereas beyond some threshold power P_{\max} , the qubit saturates in a steady mixed state with an excited state population of $p_e = 1/2$ yielding a shift of χ [108]. We measure $\chi/2\pi = 3.41$ MHz. We use the resonator readout phase φ_{RO} as indicator for the qubit state and choose a readout frequency of $\omega_{\text{RO}}/2\pi = 5.518$ GHz (cf. Fig. 3.5). Due to this particular choice, we detect the dispersive shift as the linear ramp of the arctan-function [53] and obtain the relation

$$\varphi_{\text{RO}} = -\frac{2}{\kappa}(\omega_{\text{RO}} - \omega_0) + \mathcal{O}(\omega_{\text{RO}} - \omega_0)^3. \quad (3.8)$$

Furthermore, we gauge the setup in a way that $\varphi_{\text{RO}} = 0$ corresponds to the $|g\rangle$ state. Since the RO power has to be so low that we have negligible population in $|e\rangle$, we choose it to be -40 dBm. The qubit frequency can be determined to be $\omega_q/2\pi = 6.226$ GHz. We are then able to calculate the detuning $\Delta/2\pi = 0.707$ GHz and the coupling strength $g/2\pi = \sqrt{\chi\Delta}/2\pi \simeq 49.1$ MHz. The anharmonicity is determined to be $\alpha_r = (E_{20} - 2E_{10})/2E_{10} \simeq -2.63\%$. In the following, we describe how we obtain the necessary pulse duration times and the qubit decay times with a time resolved setup. .

Rabi oscillations For tomography experiments, we need the π - and the $\pi/2$ -times. We determine these times with Rabi experiments, which means that we vary the pulse duration time τ and measure the coherent population exchange of the qubit from $|g\rangle$ to $|e\rangle$ via φ_{RO} . For the following experiments, we fix the drive power P_d to -40 dBm. Since the Rabi frequency is an approximately linear function of $\sqrt{P_d[\text{W}]}$, we calibrate our pulse lengths for a specific power. The result of such a measurement is shown in Fig. 3.7. The first maximum corresponds to the π -pulse length. We measure a π -pulse length of $t_\pi = 0.087 \mu\text{s}$. The $t_{\pi/2}$ time can then be obtained by Eq. (3.6), however, it turns out that is more accurate to simultaneously sweep the lengths of two equal successive pulses and measure the first maximum of the corresponding Rabi oscillations [108]. The $\pi/2$ -pulse length is then given by the length of one of these pulses. For the parameters above, we measure $t_{\pi/2} = 0.049 \mu\text{s}$. For QST and QPT experiments, we need drive pulses with $\varphi_d = 0^\circ$ and with $\varphi_d = 90^\circ$. Hence, it is important to know that it can happen that the π -pulse length is dependent on the qubit phase angle. This implies that there are asymmetries in the Bloch sphere, e.g., induced by electronic noise. Figure 3.8 shows a polar plot of the π -pulse length for various phase angles. In order to account asymmetries, we can measure the π -pulse length for $\varphi = 0^\circ$ [$t_\pi(0^\circ)$] and for 90° [$t_\pi(90^\circ)$], respectively. Assuming that $t_\pi(0^\circ)$ and $t_\pi(90^\circ)$ for the

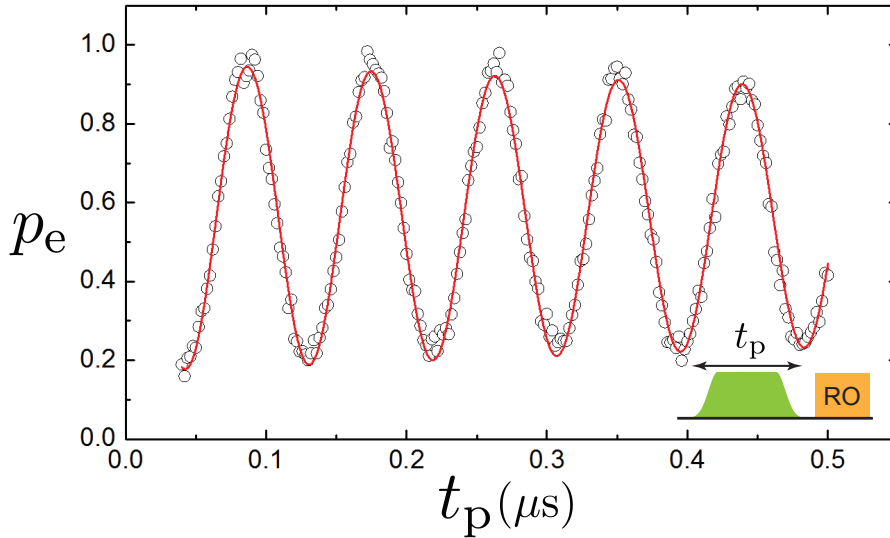


Figure 3.7: a) Population exchange manifested as Rabi oscillations. The inset shows the applied pulse pattern, The length t_p of the qubit drive pulse is increased.

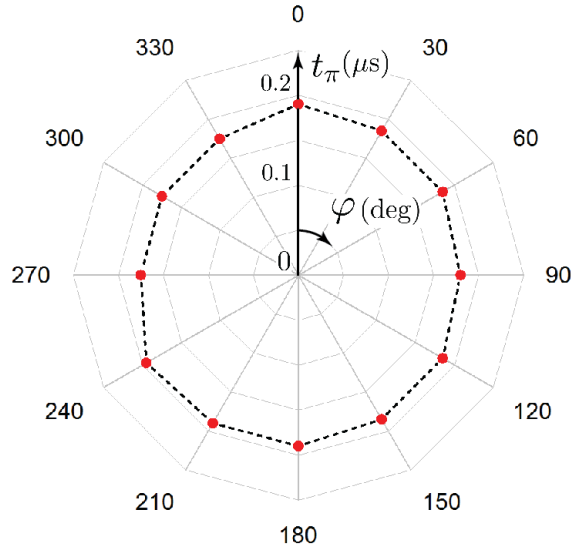


Figure 3.8: π -pulse length depending on the phase angle, which is realized with the external IQ -control.

semi axes of an ellipse, we can correct for this ellipticity and calculate $t_\pi(\varphi)$.

T_1 measurement The energy relaxation time T_1 is measured by exciting the qubit with a π -pulse and directly measuring the exponential decay. This is realized by sending a continuous RO tone after the excitation, which allows us to directly detect the time evolution of the dispersive shift [108]. We measure $T_1 = 1.76 \pm 0.06 \mu\text{s}$, and we observe fluctuations in T_1 up to 40%, as shown in Fig. 3.9. These fluctuations are probably a result from coupling to microscopic two level-fluctuators [118, 119]. We also state that there are big variations in T_1 from cooldown to cooldown. During the cooldown within which we perform our quantum memory experiment, we measure a T_1 time of $1.21 \pm 0.09 \mu\text{s}$. This reduced energy relaxation time is possibly an

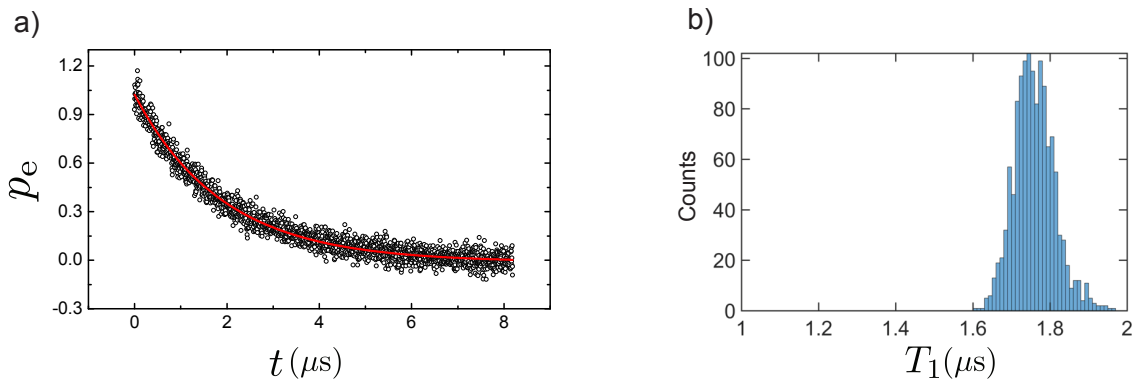


Figure 3.9: a) T_1 decay of the qubit state after excitation with a π -pulse. The qubit population p_e and decays exponentially with a decay time $T_1 = 1.9 \mu\text{s}$ b) T_1 -statistics that is recorded by repeating the measurement from a) for about 300 times. The T_1 -times are normal distributed with a maximum at $1.76 \mu\text{s}$ and standard deviation of $0.06 \mu\text{s}$

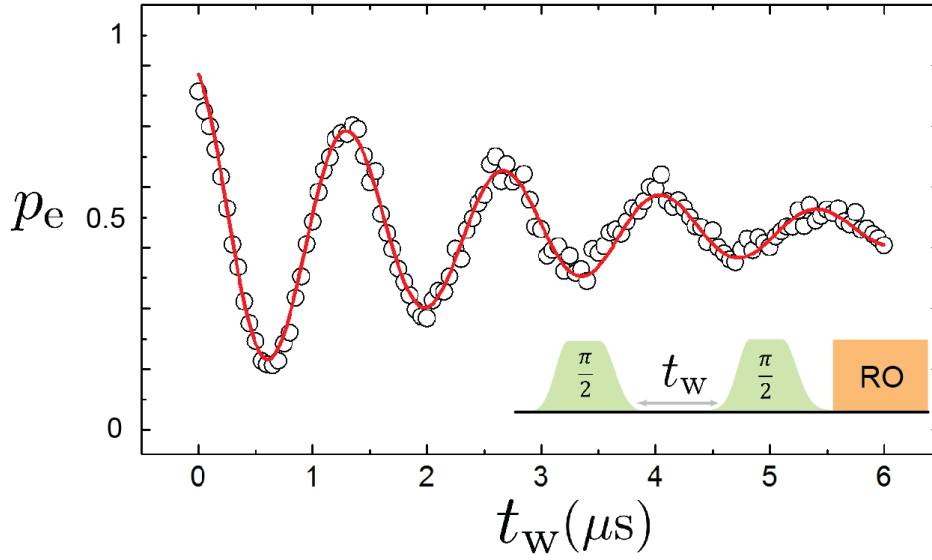


Figure 3.10: Ramsey oscillations for a detuning $\Delta/2\pi = 700$ kHz. Fitting an exponentially damped sin-function yields a decoherence time $T_2 = 2.66 \pm 0.10 \mu\text{s}$. The inset shows the Ramsey pulse scheme.

artifact from the aging process of the sample or from trapped flux during the cooldown.

Ramsey fringes In order to measure the decoherence time T_2 , we need more advanced measurement techniques, such as the Ramsey protocol [120], which consists of two $\pi/2$ -pulses separated by a variable delay time t_w . The first pulse creates the $|+\rangle$ superposition in the xy -plane. During t_w , the system loses phase coherence on the timescale T_φ and the $|e\rangle$ -population of the state (ideally $1/2$) decays on the timescale T_1 , yielding a total energy decay time of $2T_1$ for the state. Thus, regarding Eq. (2.6), the total decay time is given by T_2 . If we drive with a small detuning $\Delta = \omega_q - \omega_d$, we observe exponentially damped oscillations with frequency Δ , as depicted in Fig. 3.10. We find that the qubit is T_1 -limited, i.e., the overlap of the uncertainties contains $T_2 = 2T_1$. We estimate $T_\varphi \geq 0.33$ ms where $T_\varphi = 0.33$ ms is the worst-case estimation within the error bounds.

3.4 Memory characterization

The memory protocol consists of qubit and BSB pulses. Hence, we need to perform a similar characterization procedure as described in Sec. 3.3 for the BSB transition. We search for the BSB by sweeping ω_d in the time domain setup. We drive the system at half the BSB frequency $\omega_b/2$ in order to induce a two photon process. Furthermore, we sweep the drive power from 16 dBm to 23 dBm at the RF source. The BSB has a narrow FWHM, but broadens with increasing power. For a drive power of 21 dBm, it is on the order of 10 MHz, hence we need a relatively good initial guess. We use $\omega_{\text{init}}/2\pi = (\omega_q + \omega_m)/4\pi \simeq 7.565$ GHz, neglecting the Kerr shift and the AC Stark shift. Especially the latter one is actually relevant because it drags ω_b down to lower frequencies with increasing photon numbers. The measurement results are depicted in Fig. 3.11. We especially observe that the transition frequency decreases linearly with the drive power in microwatts. This is a characteristic property for the BSB transition [78], allowing us to differentiate this transition from, e.g., bare cavity excitations, which do not shift. We understand this behavior by considering the AC Stark shift as a function of the photon number $\omega_b(n) = \omega_0 + n\chi$ and $P[\text{W}] \propto n$. For our memory experiment, we choose a drive power of 21 dBm and determine $\omega_b/2\pi = 7.339$ GHz. Again, we determine the BSB π -pulse time with a Rabi experiment, yielding t_π^{BSB} . We can determine T_1^{BSB} in the same manner as in the qubit case, and expect $T_1^{\text{BSB}} < T_1^{\text{q}}$ due to multiple decay channels. This can be understood by a rate equation $1/T_1^{\text{BSB}} = \alpha/T_1^{\text{g}0} + \beta/T_1^{\text{g}1}$ where $T_1^{\text{g}0}$ ($T_1^{\text{g}1}$) is the decay time to $|g0\rangle$ ($|g1\rangle$) and α and β are constants. We measure $T_1^{\text{BSB}} = 0.77 \pm 0.15 \mu\text{s}$. The BSB T_2^{BSB} time is again determined with a Ramsey experiment, which yields $T_2^{\text{BSB}} = 1.83 \pm 0.19 \mu\text{s}$. Although $T_2^{\text{BSB}} > 2T_1^{\text{BSB}}$, the $2T_1^{\text{BSB}}$ limit still lies within the overlap of the error bounds of $2T_1^{\text{BSB}}$ and T_2^{BSB} . As a consequence, we can conclude that the dephasing time T_φ^{BSB} is large compared to the energy relaxation time, implying that we are T_1^{BSB} -limited. In order to optimize the pulse lengths and the frequencies for the qubit and the BSB pulses, we use an optimization procedure that is embedded into the

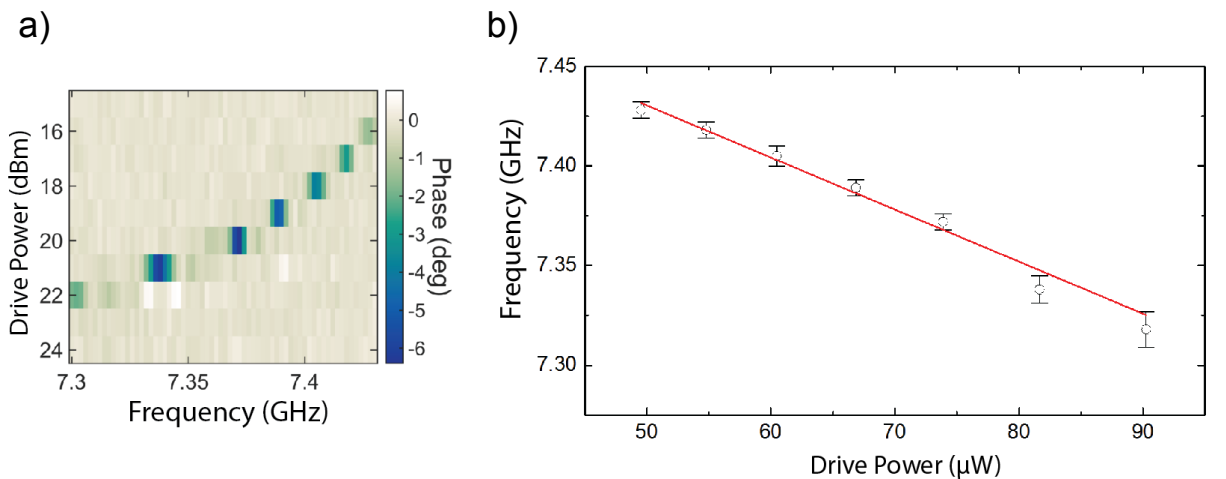


Figure 3.11: a) BSB transition for different drive powers. We observe an exponential shift to lower frequencies if we increase the drive power b) AC Stark shift for the BSB transition. We express the drive power in linear units to visualize the linear relation between power (photon number) and transition frequency.

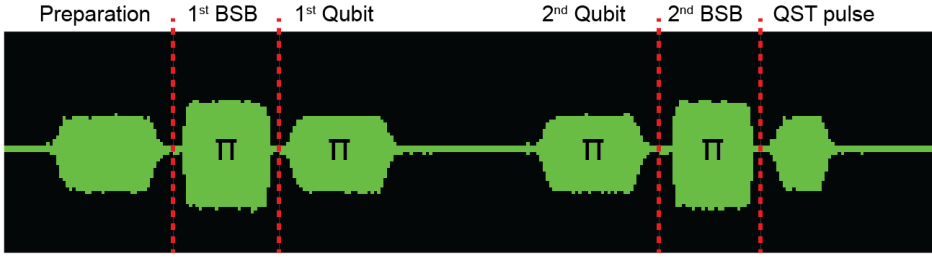


Figure 3.12: Realized pulse pattern of the memory protocol, consisting of a preparation pulse, followed by the first BSB π -pulse and a qubit π -pulse for storage. After that, we drive another qubit π -pulse and apply a second BSB π -pulse, which allows state retrieval. The last pulse is necessary for QST. The RO pulse is not depicted.

LabView control code and explained in Ref. [108].

After that, the memory pulse sequence can be realized. Due to the fact that we use different kinds of RF sources for the pulses and in order to correct the delay due to different cable lengths, we adjust the pulse timing using an oscilloscope⁸. We detect a delay of 67 ns for the qubit pulses, which we correct for in the actual memory pulse sequence. The resulting pulse pattern is depicted in Fig. 3.12. In the next step, we measure the storage time by applying the memory protocol for the $|g\rangle$ -state and varying the time between the two qubit π -pulses [108]. The resulting exponential decay is depicted in Fig. 3.13 and we extract a storage time

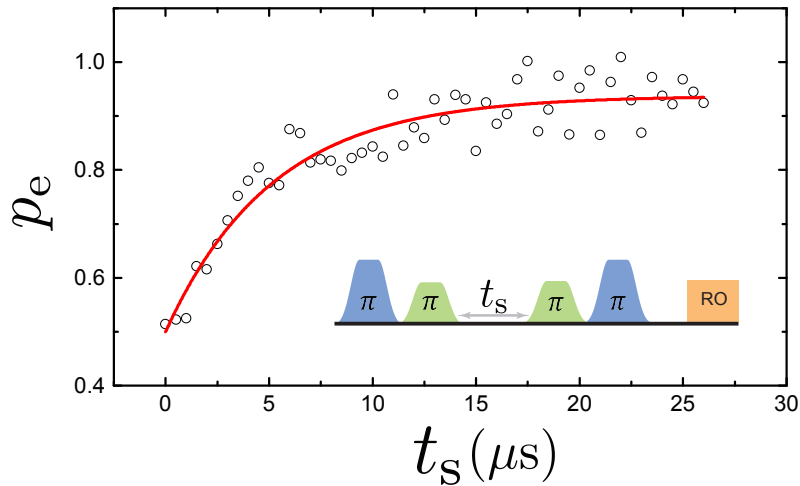


Figure 3.13: Exponential decay of the qubit population that has been transferred into the storage mode. Ideally, the curve describes the decay of the Fock state $|1\rangle_s$. We measure a decay time $T_1^s = 5.19 \pm 0.79 \mu\text{s}$

$T_s = 5.19 \pm 0.79 \mu\text{s}$, yielding an improvement factor of $T_s/T_1^q \simeq 4.3$ regarding information preservation. For the ROM, we measure a decay time of $T_1^{\text{RO}} = 0.08 \mu\text{s}$. This means that due to the special qubit and antenna positioning, we are able to perform fast readout, whereas we have

⁸We use a LeCroy WaveMaster 8600A oscilloscope

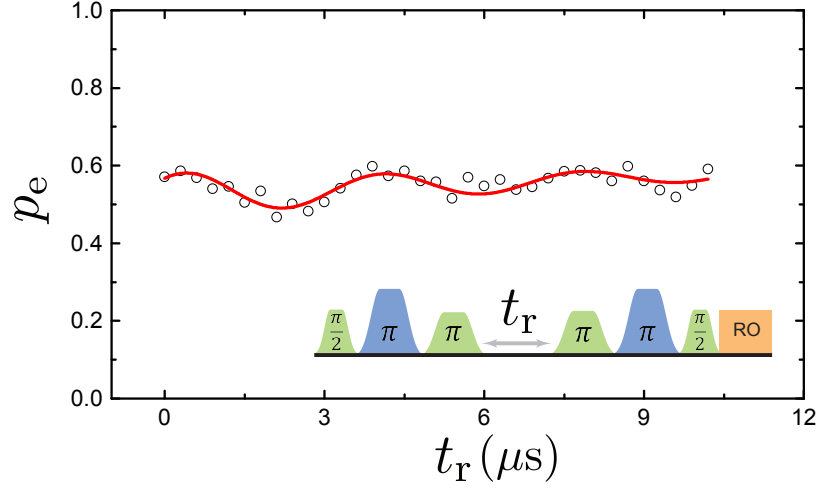


Figure 3.14: Ramsey measurement for the quantum memory. A $\pi/2$ -pulse creates a superposition state that is stored and retrieved after some time t_r . After the state regain, another $\pi/2$ -pulse is applied. We measure a decoherence time $T_2^s = 7.6 \pm 2.8 \mu\text{s}$

a slowly decaying storage mode. If we directly drive the storage mode, we have a decay on the timescale $T_1^m = 9.2 \mu\text{s}$, which is higher than T_1^s . Reasons for this deviation may be non-ideal π -pulses, decoherence during the pulse preparation, statistical T_1 fluctuations of the qubit or residual $|e\rangle$ population for the initial state.

We check whether our measured decay times are consistent. We do this by using a simplified rate equation model for the system, yielding the relation $T_s = T_1^q T_1^{\text{BSB}} / (T_1^q - T_1^{\text{BSB}})$ where we assume $T_s \gg T_1^q$. We conclude that the storage time T_s increases with increasing T_1^{BSB} and decreasing T_1^q . Within the error bounds of our measurement, we find $T_1^q = 1.12 \mu\text{s}$ and $T_1^{\text{BSB}} = 0.92 \mu\text{s}$, yielding $T_s \leq 5.15 \mu\text{s}$, which is close to the measured value. We then measure the dephasing time for the stored state again with an adopted Ramsey protocol, as illustrated in Fig. 3.14 [108]. We prepare $|+\rangle$ with a $\pi/2$ -pulse, store this resulting state, vary again the storage time, retrieve the state back and apply another $\pi/2$ pulse. Since the damped oscillation seems to be superimposed with an increasing linear trend, we fit the data using $p_e(t) = y_0 + A \sin\left(\frac{\pi(t-t_c)}{w}\right) e^{-t/T_2^s} + m \cdot t$, where y_0, A, t_c, w, T_2^s and m denote fit parameters. We find $T_2^s = 7.6 \pm 2.8 \mu\text{s}$. We extract a dephasing time $T_\phi^s = 28.6 \mu\text{s}$ of the storage mode.

Chapter 4

Benchmarking a 3D quantum memory

In this chapter, we discuss the main results of this thesis, which is the setup of a QST and a QPT protocol in order to characterize the quality of our quantum memory. Based on the theory described in Sec. 2.2.3 and in Sec. 2.3.2, we realize the respective pulse patterns with our arbitrary pulse software. We use a Matlab[®] routine ¹ for data analysis and the MLE for QST and QPT, respectively. In the first section, we introduce the implementation of QST and test our protocol by reconstructing well known single qubit states. After that, we are able to realize a QPT protocol, which is discussed in the second section. We benchmark QPT with single qubit processes [38], i.e., specific rotations and decoherence. We reconstruct the Bloch sphere for each process and discuss the reasons for deformations. With this toolbox at hand, we are able to apply it to the quantum memory process. In the third section, we use QST in order to reconstruct quantum states that have been stored in the memory mode. Finally, in the fourth section, we obtain the quantum process fidelity of our quantum memory process, which can be regarded as the main result of this thesis. We discuss observations and possible reasons regarding fidelity limitations. We face the remaining problem that QPT is a blackbox by using a master equation approach that models the process matrix in a time-resolved manner [88].

4.1 Single qubit benchmarking for QST

For implementing and testing QST, a few preliminary experimental requirements have to be fulfilled. As described in Sec. 2.2.3, we need a measure μ that contains information about the qubit state with respect to the quantization axis and that is easy to access in experiment. For our purposes, we choose the readout phase φ_{RO} of the cavity TE101 mode [108]. Since the dispersive shift is small compared to the linewidth of the resonator, we are still in the linear regime as indicated by Eq. (3.8). Furthermore, our working point is chosen such that $\varphi_e \leq \varphi_{\text{RO}} \leq \varphi_g$, where φ_e (φ_g) denotes the RO phase for $|e\rangle$ ($|g\rangle$). This implies that we can reconstruct the

¹We use MATLAB R2016a

density matrix as

$$\rho(\{\varphi_i\}) = \frac{1}{\varphi_g - \varphi_e} \begin{pmatrix} \varphi_z - \varphi_e & \bar{\varphi} - \varphi_x - i(\bar{\varphi} - \varphi_y) \\ \bar{\varphi} - \varphi_x + i(\bar{\varphi} - \varphi_y) & \varphi_g - \varphi_z \end{pmatrix} \quad (4.1)$$

with $\bar{\varphi} \equiv (\varphi_g + \varphi_e)/2$. A derivation can be found in Sec. A.1 in the appendix. For the MLE, we parametrize $\tilde{\varphi}_{x,y,z}(\{t_i\})$ from Eq. (4.1):

$$\tilde{\varphi}_{x,y,z}(\{t_i\}) = \bar{\varphi} - \frac{\text{Tr}(\tilde{\rho}\hat{\sigma}_{x,y,z})}{2}(\varphi_g - \varphi_e) \quad (4.2)$$

where $\tilde{\rho} = \tilde{\rho}(\{t_i\})$ is defined as described in Sec. 2.2.3. Equation (4.1) allows us to directly calculate the fidelity as a function of the RO phases, which is necessary for calculating the uncertainty in fidelity from the measurement uncertainties. Consider that we measure $\rho \in \{|g\rangle\langle g|, |e\rangle\langle e|, |+\rangle\langle +|, |-\rangle\langle -|\}$ and compare the result with the respective theoretical density matrix ρ_t . We use Eq. (2.51) and obtain a fidelity $f(\rho, \rho_t) = \sqrt{\text{Tr}\rho\rho_t}$. This yields

$$f_{|g\rangle\langle g|} = \sqrt{\frac{\varphi_z - \varphi_e}{\varphi_g - \varphi_e}} \quad f_{|e\rangle\langle e|} = \sqrt{\frac{\varphi_g - \varphi_z}{\varphi_g - \varphi_e}} \quad f_{|+\rangle\langle +|} = \sqrt{\frac{\varphi_x - \varphi_e}{\varphi_g - \varphi_e}} \quad f_{|-\rangle\langle -|} = \sqrt{\frac{\varphi_y - \varphi_e}{\varphi_g - \varphi_e}}. \quad (4.3)$$

These analytic expressions allow us to calculate the propagation of the error [121]. For $|g\rangle$, we obtain

$$\Delta f_{|g\rangle\langle g|} = \frac{1}{2f_{|g\rangle\langle g|}(\varphi_g - \varphi_e)} \sqrt{\left(\frac{\varphi_z - \varphi_g}{\varphi_g - \varphi_e}\right)^2 (\Delta\varphi_e)^2 + (\Delta\varphi_z)^2}. \quad (4.4)$$

We obtain similar results for the other states in Eq. (4.3). For the CMS, we obtain from Eq. (2.51) and Eq. (4.1) that

$$f_* \equiv f(\rho_*, \rho_t) = \sqrt{\frac{1}{2} + \frac{1}{\varphi_g - \varphi_e} \sqrt{(\varphi_z - \varphi_e)(\varphi_g - \varphi_z) - (\bar{\varphi} - \varphi_x)^2 - (\bar{\varphi} - \varphi_y)^2}}. \quad (4.5)$$

We perform error propagation [121], which yields

$$\Delta f = \frac{1}{4f_*(\varphi_g - \varphi_e)^2(2f_*^2 - 1)} \times \sqrt{((2f_*^2 - 1)(\varphi_g - \varphi_e) + 2(\sum_{i=x,y,z} \varphi_i - 2\varphi_g - \varphi_e)^2(\Delta\varphi_e)^2 + 4 \sum_{i=x,y,z} (\varphi_i - \bar{\varphi})^2(\Delta\varphi_i)^2)}. \quad (4.6)$$

In this case, we neglect effects resulting from the MLE, and we assume for our error estimation that the uncertainties are not affected by the MLE. An alternative approach is the comparison of the phases before and after the MLE and a proper scaling of the measurement uncertainties, under the assumption that the relative uncertainties stay constant. We define in our measurement routine $\varphi_g \equiv 0$, and we determine an average φ_e from a sufficient amount of measurements, where we prepare the qubit with a π -pulse. The small depolarization during the finite π -pulse length is neglected. We observe a decrease of the measured fidelities of 1 – 2% if we use the corrected value $\varphi_e \cdot \exp(t_\pi/T_1)$. With these measures at hand, we are now able to tomographically reconstruct arbitrary qubit states. We test our protocol by measuring the density matrix for

$|g\rangle$, $|e\rangle$, $|+\rangle$ and $|-\rangle$. We choose these particular states because we use them as inputs for our QPT protocol, which means that our benchmarking procedure for QST simultaneously precharacterizes the initial states for QPT. Each projective measurement is repeated for a sufficient number of times, which enables us to accurately approximate the standard deviation. For each reconstructed state, we calculate the distance measures introduced in Sec. 2.4.1 in Tab. 4.1. As an initial test, we measure the density matrix for $|g\rangle$. The result is depicted in Fig. 4.1 a) We obtain a fidelity of $f_{|g\rangle} = 0.966 \pm 0.008$. The other measured density matrices are found in Fig. 4.1 b)-e) and the fidelities and distance measures are summarized in Tab. 4.1.

	$ g\rangle$	$ e\rangle$	$ +\rangle$	$ -\rangle$	CMS	Distance limit
$D(\rho, \rho_t)$	0.0700	0.0512	0.0604	0.0402	0.0267	0.5
$1 - f(\rho, \rho_t)$	0.0338	0.0013	0.0018	0.0161	0.0004	0.293
$B(\rho, \rho_t)$	0.2601	0.0512	0.0605	0.1794	0.0267	0.765
$\mathcal{C}(\rho, \rho_t)$	0.2579	0.0512	0.0604	0.1786	0.0267	0.707

Table 4.1: Distance measures for QST benchmarking for the reconstruction of $|g\rangle$, $|e\rangle$, $|+\rangle$, $|-\rangle$ and the CMS. The distance measures are equal to zero for the ideal case.

In order to measure the density matrix of the CMS, we create the CMS by driving the qubit at ω_q with a pulse length $\tau = 8.7\mu\text{s} \gg T_1$ such that we end up in the CMS. The reconstructed state ρ_* is depicted in Fig. 4.1 e). We calculate a fidelity of $f_* = 0.9996 \pm 0.0034$. For all reconstructed states, we observe that we are way below the distance limits (cf. Tab. 4.1), proving that we are able to perform single qubit QST.

Distance limits for QST The QST benchmarking measurements allow us to verify the distance limits derived in Sec. 2.4.2. We realize this by calculating $\text{dist}(\rho_{|g\rangle}, \rho_{*,t})$ and $\text{dist}(\rho_*, \rho_{|g\rangle,t})$, where $\rho_{*,t}$ ($\rho_{|g\rangle,t}$) denotes the theoretical density matrix of the CMS ($|g\rangle$), and $\rho_{|g\rangle}$ (ρ_*) is the respective reconstructed density matrix. $\text{dist}(\cdot, \cdot)$ denotes the trace distance, the infidelity, the Bures distance and the \mathcal{C} -distance respectively. The results are listed in Tab. 4.2

	$\text{dist}(\rho_{ g\rangle}, \rho_{*,t})$	$\text{dist}(\rho_*, \rho_{ g\rangle,t})$	Distance limit
D_{lim}	0.4740	0.5018	0.5
$1 - f_{\text{lim}}$	0.2747	0.2936	0.293
B_{lim}	0.7413	0.7663	0.765
\mathcal{C}_{lim}	0.6885	0.7079	0.707

Table 4.2: Experimental verification of the distance limits derived in Sec. 2.4.2

We observe that all distance measures are close to their theoretical limit. Deviations can be attributed to slight temporal fluctuations in φ_e , which are not taken into account by the calibration. We especially observe that we are slightly above the limits when we compare the reconstructed ρ_* with $\rho_{|g\rangle,t}$, which is not expected since the limits are considered as an upper bound. We explain this behavior with a residual population in $|e\rangle$ due to thermal excitations, which breaks the symmetry between $|g\rangle$ and $|e\rangle$ for the CMS. Let p_e denote the

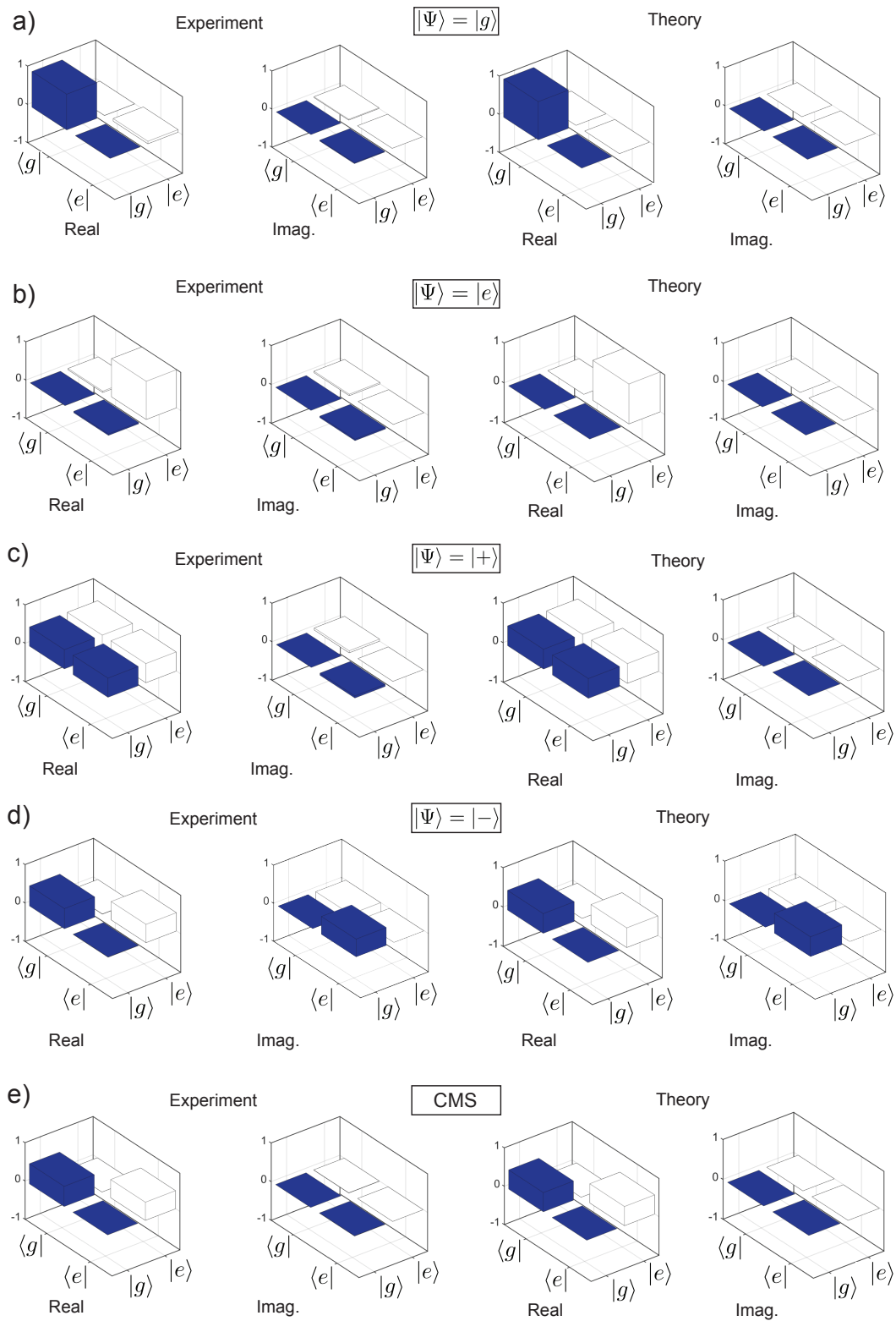


Figure 4.1: QST of a) the $|g\rangle$ -state, b) the $|e\rangle$ -state, c) the $|+\rangle$ -state, d) the $|-\rangle$ -state and e) the CMS.

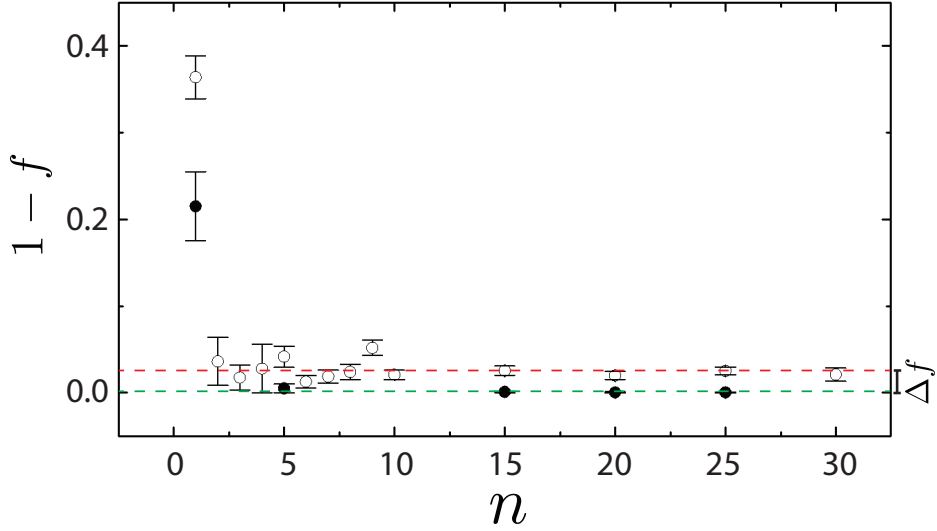


Figure 4.2: Absolute (white dots) and relative (black dots) fidelity for the reconstructed $|-\rangle$ -state for different amounts of averages n . The fidelity measures converge for $n \gtrsim 10$. We extract an asymptotic difference of $\Delta f = 3\%$

residual population of $|e\rangle$. We then expect to measure $\rho_{*,11} = 1/2(1 - p_e)$ and $\rho_{*,22} = 1/2(1 + p_e)$ and obtain $p_e = 1 - 2f^2$, where f is measured fidelity. Hence, we estimate $p_e = 0.2\%$, which is consistent with the result found in Ref. [108].

Influence of averaging A limiting factor for the time expenditure of QST is the amount of averages that we have to consider, i.e. the number of repetitions for each measurement cycle. In our specific setup described in Sec. 3.2.2 to record and process a single φ_{RO} -value, we need to spend approximately 5s. This measurement time already includes a number of 2×10^7 averages [108, 111]. Our QST routine consists of 3 projective measurements, hence we need a total measurement time of $15\text{s} \times n$, where n denotes the number of repetitions of each projection measurement. As an example, we reconstruct the $|-\rangle$ -state for varying n . Let ρ_n denote the measured density matrix after n repetitions. We reconstruct ρ_n for $1 \leq n \leq 50$ and calculate the fidelity $f^{(n)} \equiv f(\rho_n, \rho_t)$, where ρ_t denotes the theoretically expected result. Furthermore, we calculate the relative fidelity $f_{\text{rel}}^{(n,m)} \equiv f(\rho_{n+m}, \rho_n)$ (cf. Ref. [122]) for $m = 5$ and $n \in \{0, 5, 10, 15, 20, 25\}$. In contrast to the absolute fidelity, the relative fidelity is a measure for the influence of statistics and depends only on n . Both quantities are depicted Fig. 4.2 as a function of n . If $f_{\text{rel}}^{(n,m)} \rightarrow 1$, we know that additional averaging does no longer improve the result, as ρ_{n+m} and ρ_n become indistinguishable. The quantity $\mathcal{Q}^{(n,m)} \equiv |f_{\text{rel}}^{(n,m)} - f^{(n)}|$ is a measure for losses in fidelity due to decoherence, inaccurate state preparation, non-ideal pulse lengths and higher levels resulting from the low anharmonicity and we define the fidelity deviation $\Delta f \equiv \lim_{n \rightarrow \infty} \mathcal{Q}^{(n,5)}$. From Fig. 4.2, we obtain $\Delta f = 3\%$. We especially observe that the fidelity is significantly worse for $n = 1$, compared to $n = 2$. An explanation for that is that the MLE needs at least two averages in order to calculate the standard deviation. Then, the MLE significantly improves the result. We notice that we only need to repeat the experiment

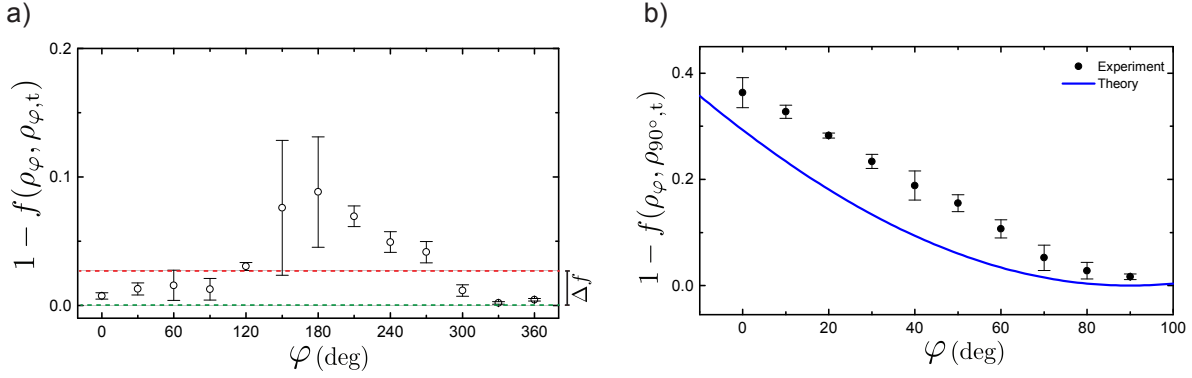


Figure 4.3: a) Infidelities for the reconstructed state ρ_φ in the xy -plane. The infidelity gets significantly worse for $\varphi \rightarrow 180^\circ$. b) Infidelities $1 - f(\rho_\varphi, \rho_{90^\circ, t})$ for reconstructed states ρ_φ with $0^\circ \leq \varphi \leq 90^\circ$. The infidelity decreases monotonically with φ . The blue curve shows the expected fidelity, assuming ideal pulses and neglecting decoherence and the finite anharmonicity.

for about five to ten times in order to get precise results.

Benchmarking the phase control In the next step, we test the phase sensitivity of our QST procedure, which depends on the accuracy of our IQ -control. We investigate this by driving $\pi/2$ -pulses while varying the phase angle φ . This means that we reconstruct states in the xy -plane with discrete steps in phase angle φ . The expected theoretical density matrix $\rho_{\varphi, t}$ can be directly derived from Eq. (2.7),

$$\rho_{\varphi, t} = \frac{1}{2} \begin{pmatrix} 1 & \cos \varphi \\ \cos \varphi & 1 \end{pmatrix} + \frac{i}{2} \begin{pmatrix} 0 & -\sin \varphi \\ \sin \varphi & 0 \end{pmatrix} = \frac{1}{2} (I + \cos \varphi \hat{\sigma}_x + \sin \varphi \hat{\sigma}_y). \quad (4.7)$$

We sweep φ from 0° to 360° in steps of 10° and reconstruct ρ_φ for each angle. In Fig. 4.3 a), we plot the respective infidelities $1 - f(\rho_\varphi, \rho_{\varphi, t})$. We measure an infidelity of approximately $\Delta f = 3\%$ for $\varphi \leq 120^\circ$ and $\varphi \geq 270^\circ$. The infidelity increases towards $\varphi = 180^\circ$. We assign this to numerical errors due to the fact that $\varphi = 180^\circ$ corresponds to the in-phase quadrature $I = 0$ and we have to divide by I in order to obtain φ [cf. Eq. (3.1)]. We further investigate the φ -range from 0° to 90° in more detail. We choose this range because it is relevant for our QPT protocol. Again, we reconstruct ρ_φ for each phase angle. We calculate the fidelities $f(\rho_{90^\circ, t}, \rho_\varphi)$ and plot the result in Fig 4.3 b). We observe that the infidelity decreases approximately linearly towards 3% for $\varphi = 90^\circ$, which is consistent with the value obtained in Fig. 4.2. We calculate the theoretical fidelity curve from Eq. (4.7) and obtain

$$f_{\varphi, t} \equiv f(\rho_{90^\circ, t}, \rho_{\varphi, t}) = \sqrt{\frac{1 + \sin \varphi}{2}}. \quad (4.8)$$

We observe an offset of 3–4%, compared to the measured data points, which equals approximately the fidelity deviation Δf . Hence, we conclude that we are able to perform QST for arbitrary pure and mixed single qubit with a fidelity limited by the IQ microwave equipment.

4.2 QPT for single qubit operations

Resulting from the fact that we are able to perform QST, we can now implement a protocol for single qubit QPT (cf. Fig. 2.15). We work in the basis $\{I, \hat{\sigma}_x, -i\hat{\sigma}_y, \hat{\sigma}_z\}$ [12] to keep the calculations simple, as described in Sec. 2.3.2. For testing our protocol, we determine the χ -matrix for simple quantum operations, i.e., single qubit rotations and the CDP. We calculate the Kraus representation of the process with Eq. (2.38). Equation (2.27) and equation (2.28) allow us to illustrate the process result with the Bloch sphere.

First, we perform QPT for the identity process. We expect a process matrix

$$\chi_{I,t} = \begin{pmatrix} 1 & 0 & 0 & 0 \\ 0 & 0 & 0 & 0 \\ 0 & 0 & 0 & 0 \\ 0 & 0 & 0 & 0 \end{pmatrix}. \quad (4.9)$$

The measured process matrix, the reconstructed Bloch sphere as well as the theoretical results are depicted in Fig 4.4 a).

We calculate a process fidelity of $f_I = 0.9743$. The respective distance measures (cf. Sec. 2.4.1) are listed in Tab. 4.3.

	I	$\hat{R}_y(\pi)$	$\hat{R}_y(\frac{\pi}{2})$	$\hat{R}_x(\frac{\pi}{2})$	CDP
$D(\chi, \chi_t)$	0.2253	0.1133	0.1941	0.1830	0.1161
$1 - f(\chi, \chi_t)$	0.0257	0.0295	0.0665	0.0897	0.0118
$B(\chi, \chi_t)$	0.2258	0.2430	0.3647	0.4235	0.1533
$\mathcal{C}(\chi, \chi_t)$	0.2253	0.2412	0.3586	0.4139	0.1529
$\ \mathcal{E} - \mathcal{E}_{\text{id}}\ _{\diamond}$	0.0520	-	-	-	-

Table 4.3: Distance measures for QPT benchmarking for the reconstruction of the identity process (I), a rotation by π about the y -axis, a rotation by $\pi/2$ about the y -axis, a rotation by $\pi/2$ about the x -axis and the CDP. The distance measures are equal to zero for the ideal case. The diamond norm is only calculated for the identity process since this is the relevant process for characterizing a quantum memory and we can use Eq. (2.55)

In order to analyze rotation processes, we derive an explicit expression for the process matrix for a rotation about an axis \mathbf{n} by an angle α . Starting with Eq. (2.29) and using $e^{i\alpha A} = \cos \alpha I + i \sin \alpha A$ [12] for quadratic matrices A , we obtain

$$\begin{aligned} \rho' &= \hat{R}_{\mathbf{n}}(\alpha) \rho \hat{R}_{\mathbf{n}}(\alpha)^\dagger \\ &= \left(\cos \frac{\alpha}{2} I - i \sin \frac{\alpha}{2} \sum_{j=1}^3 n_j \hat{\sigma}_j \right) \rho \left(\cos \frac{\alpha}{2} I^\dagger + i \sin \frac{\alpha}{2} \sum_{k=1}^3 n_k \hat{\sigma}_k^\dagger \right) \end{aligned} \quad (4.10)$$

After reordering the terms, we obtain

$$\chi_{\mathbf{n}, \alpha} = \begin{pmatrix} \cos^2 \frac{\alpha}{2} & i \sin \frac{\alpha}{2} \cos \frac{\alpha}{2} n_x & \sin \frac{\alpha}{2} \cos \frac{\alpha}{2} n_y & i \sin \frac{\alpha}{2} \cos \frac{\alpha}{2} n_z \\ -i \sin \frac{\alpha}{2} \cos \frac{\alpha}{2} n_x & \sin^2 \frac{\alpha}{2} n_x^2 & -i \sin^2 \frac{\alpha}{2} n_x n_y & \sin^2 \frac{\alpha}{2} n_x n_z \\ \sin \frac{\alpha}{2} \cos \frac{\alpha}{2} n_y & i \sin^2 \frac{\alpha}{2} n_x n_y & \sin^2 \frac{\alpha}{2} n_y^2 & i \sin^2 \frac{\alpha}{2} n_y n_z \\ -i \sin \frac{\alpha}{2} \cos \frac{\alpha}{2} n_z & \sin^2 \frac{\alpha}{2} n_x n_z & -i \sin^2 \frac{\alpha}{2} n_y n_z & \sin^2 \frac{\alpha}{2} n_z^2 \end{pmatrix} \quad (4.11)$$

We analyze the process incuded by a π -pulse with $\varphi = 0^\circ$, i.e., a 180° rotation about the y -axis. We expect

$$\chi_{\hat{R}_y(\pi)} = \begin{pmatrix} 0 & 0 & 0 & 0 \\ 0 & 0 & 0 & 0 \\ 0 & 0 & 1 & 0 \\ 0 & 0 & 0 & 0 \end{pmatrix}. \quad (4.12)$$

In Fig. 4.4 b), we plot the predicted and the measured results. We obtain a process fidelity $f_{\hat{R}_y(\pi)} = 0.9705$, calculate the remaining distance measures and show the results in Tab. 4.3. An analogue procedure is performed for a rotation by 90° about the y -axis. We extract a fidelity of $f_{\hat{R}_y(\frac{\pi}{2})} = 0.9335$ and depict the results in Fig. 4.4 c) and in Tab. 4.3. The last rotation under investigation is a rotation by 90° about the x -axis. In contrast to the rotation about the y -axis, this rotation contains a finite phase angle of $\varphi = 90^\circ$. We calculate a fidelity of $f_{\hat{R}_x(\frac{\pi}{2})} = 0.9103$.

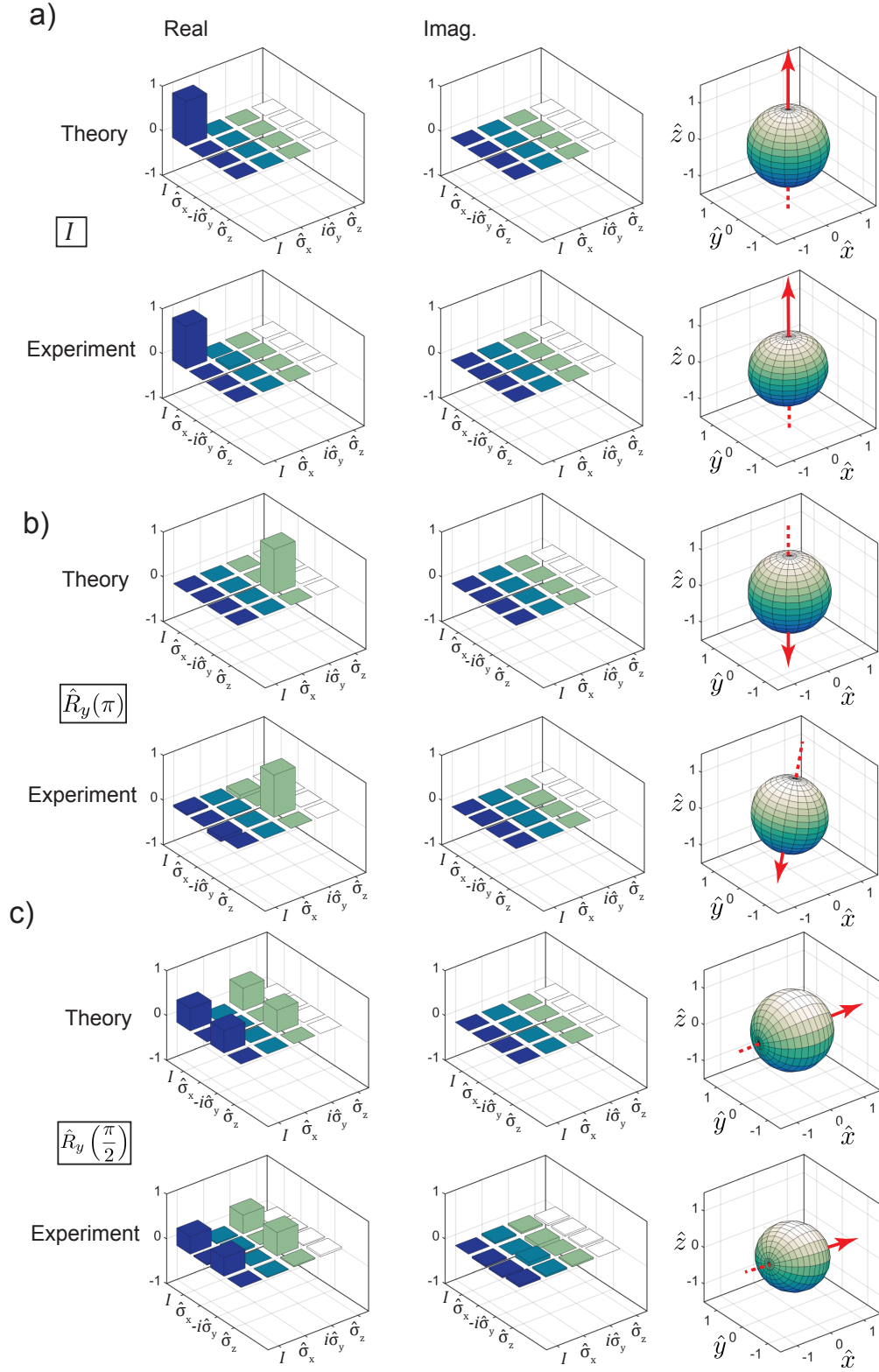


Figure 4.4: Reconstruction of a) the identity process, b) a rotation by π about the y -axis and c) a rotation by $\pi/2$ about the y -axis. The measurement results are compared with the theoretically predicted results, respectively. We observe that the radius of the Bloch sphere shrinks (depolarization). We observe from b) that $\hat{R}_y(\pi)$ does not rotate the Bloch sphere by exactly 180° .

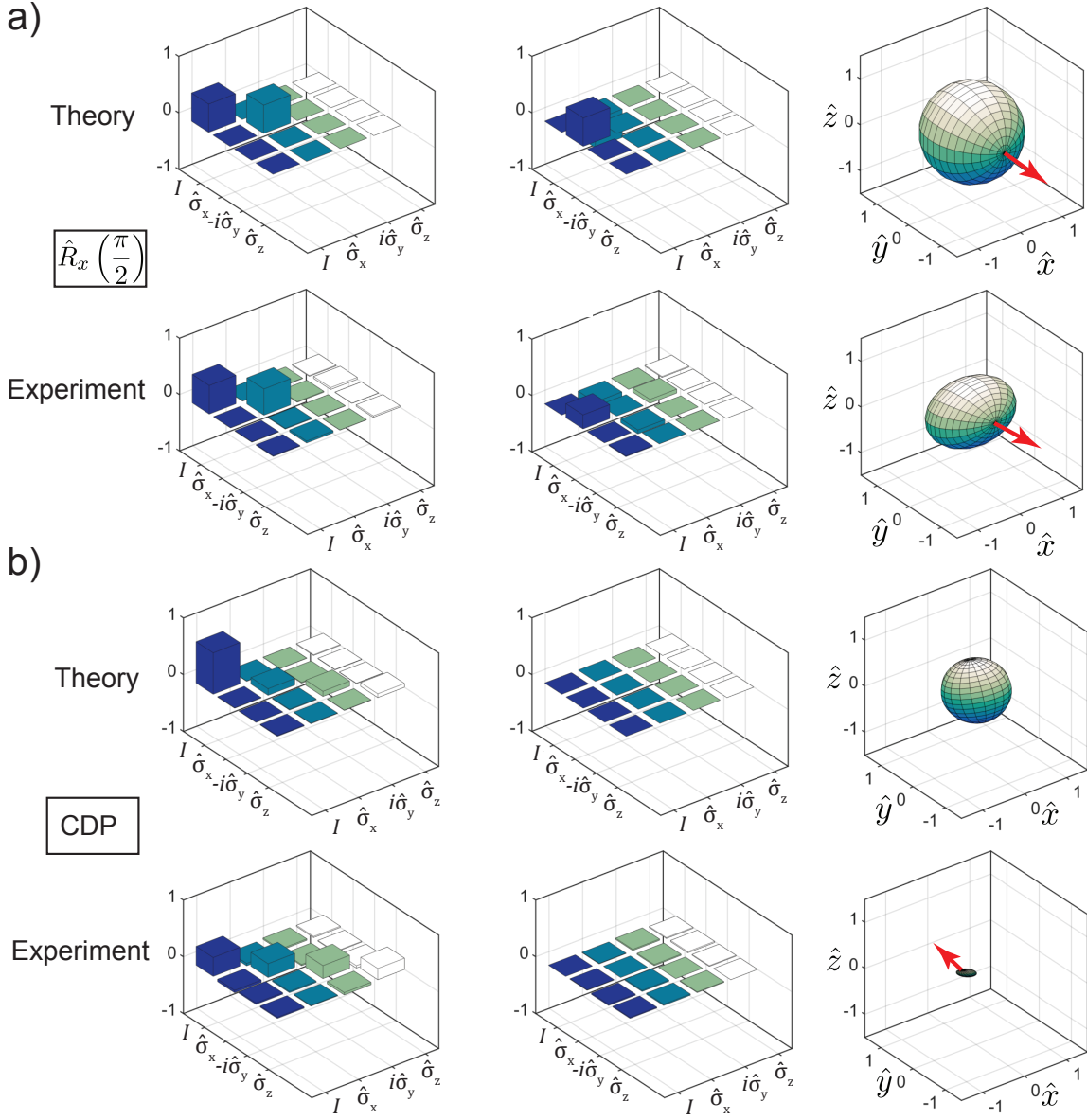


Figure 4.5: Reconstruction of a) a rotation by $\pi/2$ about the x -axis and b) the CDP. The measurement results are compared with the theoretically predicted results, respectively. For the CDP, the Bloch sphere contracts to its center.

For the process matrices, we expect

$$\chi_{\hat{R}_y(\frac{\pi}{2})} = \frac{1}{2} \begin{pmatrix} 1 & 0 & 1 & 0 \\ 0 & 0 & 0 & 0 \\ 1 & 0 & 1 & 0 \\ 0 & 0 & 0 & 0 \end{pmatrix} \quad \chi_{\hat{R}_x(\frac{\pi}{2})} = \frac{1}{2} \begin{pmatrix} 1 & i & 0 & 0 \\ -i & 1 & 0 & 0 \\ 0 & 0 & 0 & 0 \\ 0 & 0 & 0 & 0 \end{pmatrix}. \quad (4.13)$$

We plot the theoretical predictions as well as the reconstructed data in Fig. 4.5 a). We

summarize the distance measures in Tab 4.3. In order to investigate the effect of depolarization, we reconstruct the CDP. We realize this process with a microwave pulse with a length of $\tau = 8.7 \mu\text{s} \gg T_1$. This process maps every single qubit state to the center of the Bloch sphere. We predict

$$\chi_* = \frac{1}{4} \begin{pmatrix} 1 & 0 & 0 & 0 \\ 0 & 1 & 0 & 0 \\ 0 & 0 & 1 & 0 \\ 0 & 0 & 0 & 1 \end{pmatrix} \quad (4.14)$$

and measure a process fidelity of $f_* = 0.9882$. The theoretically expected and the measured results are depicted in Fig. 4.5 b) and the distances are calculated in Tab. 4.3. For the ideal CDP, the Bloch sphere contracts to a single point, implying that its volume is zero after the process. We determine the remaining volume for the reconstructed CDP by calculating the Bloch vectors $\mathbf{a}_{|g\rangle\langle g|} = (0.0518, -0.0351, -0.0121)^T$, $\mathbf{a}_{|+\rangle\langle +|} = (0.0178, -0.0281, -0.0539)^T$ and $\mathbf{a}_{|- \rangle\langle -|} = (0.1761, -0.0663, -0.0604)^T$. We assume that the reconstructed deformed Bloch sphere in Fig. 4.5 b) has an ellipsoidal shape, yielding a Bloch volume $V_{\text{Bloch}} \simeq 4\pi(|\mathbf{a}_{|g\rangle\langle g|}| |\mathbf{a}_{|+\rangle\langle +|}| |\mathbf{a}_{|- \rangle\langle -|}|)/3 \simeq 0.0033$. The high fidelity of the reconstructed single qubit processes is also reflected in the distance limits, which are summarized in Tab. 4.4.

	$\text{dist}(\chi_I, \chi_{*,t})$	$\text{dist}(\chi_*, \chi_{I,t})$	Theoretical limit
D_{lim}	0.6994	0.6720	0.75
$1 - f_{\text{lim}}$	0.4003	0.4241	0.5
B_{lim}	0.8948	0.9209	1
\mathcal{C}_{lim}	0.8002	0.8175	0.866
$\ \cdot\ _{\diamond\text{lim}}$	—	0.3996	0.433

Table 4.4: Distance limits for QPT. The measurement results for the reconstruction of the identity are compared with the ideal CDP and the reconstructed CDP is compared with the ideal identity process. The fourth row shows the theoretically predicted distance limits.

Influence of temperature fluctuations We observe that there may be fluctuations in the RO phase for different measurement cycles. We usually measure $\varphi_e \simeq -8^\circ$ and detect deviations $\Delta\varphi$ between $0.5^\circ - 1^\circ$, i.e. relative fluctuations of about 10%. This is especially important for the calibration of our QST and QPT protocols, since they are based on an accurately measured and constant φ_e , implying that the variations in the RO phase may influence the tomography fidelities. We may ask ourselves whether these phase fluctuations come from changes in temperature or from the used pulse pattern, which can cause excitations of higher levels. Another reason could be variations in ω_q , which tilts the rotation plane as illustrated in Fig. 2.8 c). We discuss the influence of these effects on QPT and QST experiments. Changes in temperature may impact the RO phase in different manners. We analyze effects induced by a temperature modification ΔT , such as [108]

- thermal photons inside the cavity, which shift the qubit away from the working point due to an AC Stark shift,

- thermal expansion of the cavity, which implies changes in the resonance frequencies
- photons induced by the antennas inside the cavity

For the first case, we find a change ΔN_{th} for the thermal photon population N_{th} [123] (cf. Sec. C.1 in the appendix)

$$\frac{\Delta\varphi}{\varphi_{\text{g}} - \varphi_{\text{e}}} = \Delta N_{\text{th}} = N_{\text{th}}(t + \Delta T) - N_{\text{th}}(T) = \frac{6\zeta(3)V}{\pi^2} \left(\frac{k_{\text{B}}}{\hbar c}\right)^3 T^2 \Delta T + \mathcal{O}(\Delta T^2) \quad (4.15)$$

with the cavity volume V , the Boltzmann constant k_{B} , the speed of light c and the Riemann zeta function ζ [115]. The AC Stark shift scales linearly with the photon number, and as described in Sec. 4.1, we assume a linear dependence for the change $\Delta\varphi$ of the RO phase. For the measured temperatures ($T \simeq 30$ mK, $\Delta T \simeq 4$ mK), we estimate that

$$\frac{\Delta\varphi}{\varphi_{\text{g}} - \varphi_{\text{e}}} \simeq 0.2\% \quad (4.16)$$

which is negligible compared to the observed fluctuations.

Furthermore, temperature fluctuations could change the dimensions of the cavity, which changes the frequency ω_0 of the transmission peak and hence the detected readout phase. In Sec. C.2 in the appendix, we derive an expression for the changes in the RO phase induced by this effect. In summary, we obtain

$$\frac{\Delta\varphi}{\varphi_0 - \varphi_1} = \frac{\omega_0}{\chi} \alpha \Delta T. \quad (4.17)$$

With the thermal expansion coefficient α . Since the expansion coefficient decreases at low temperatures, we obtain an upper bound if we take α [124] at room temperature. For aluminum, we have $\alpha_{\text{RT}} = 23.5 \cdot 10^{-6} \text{ K}^{-1}$ [125]. This yields, for $\Delta T = 4$ mK,

$$\frac{\Delta\varphi}{\varphi_0 - \varphi_1} \leq \frac{f_p}{\chi/2\pi} \alpha_{\text{Rt}} \Delta T \simeq 0.01\%, \quad (4.18)$$

which is negligible.

We now discuss the third case. It may occur that the antennas inside the cavity heat up, either by Joule heating from high microwave drive powers or by thermally coupling to upper stages of the cryostat, which are higher in temperature. In order to give a rough estimation for the influence of photons induced by the antennas, we assume that the antennas heat up by ΔT . The resulting change in internal energy is then emitted as photons with a mean wavelength $\bar{\lambda}$ that is calculated from the Planck curve. In Sec. C.3 in the appendix, we find

$$\frac{\Delta\varphi}{\varphi_0 - \varphi_1} = \frac{\rho^2 \gamma d^2 \pi l b}{\underbrace{4M_{\text{mol}} \hbar c}_{\equiv \beta}} \cdot \Delta T \quad (4.19)$$

with the antenna material density ρ , the Sommerfeld coefficient γ [49], the molar mass M_{mol} of the antenna material, the antenna length l , the antenna diameter d , the Planck constant h and a Wien-like constant $b = 0.003\,669\,7 \text{ K m}$ [126, 127]. We find $\beta \simeq 1 \cdot 10^{18} \text{ K}^{-1}$, which

yields large phase fluctuations for small temperature fluctuations. However, we have to take into account that only a small part of the heat is transported via thermal radiation. One reason for that are the low operation temperatures. To show that we assume that radiation is the only channel for heat transfer. The emitted energy in an infinitesimal time interval dt is given by the Stefan-Boltzmann law $dE = \varepsilon\sigma AT^4 dt$ [124] with the emissivity ε and the Stefan-Boltzmann constant $\sigma = 5.67 \cdot 10^{-8} \text{ W m}^{-2} \text{ K}^{-4}$. The cooling of the antenna is then given by $c_a(T)mdT$ and we obtain

$$\varepsilon\sigma AT^4 = \gamma T \frac{\rho}{M_{\text{mol}}} \cdot m \frac{dT}{dt}. \quad (4.20)$$

We solve this equation with the initial condition $T(0) = T_e + \Delta T$, where T_e is the temperature in thermal equilibrium. This allows us to calculate the time t_{rad} after which the system reaches again an equilibrium state. Since the emissivity depends on the surface structure as well as on the temperature of the material, we need to make estimations. Hence, we set ε to one, assuming that the antennas are black-body emitters. Thus, Eq. (4.21) gives us a lower bound for t_{rad} [125]².

$$t_{\text{rad}} = \frac{\rho^2 \gamma d}{8\varepsilon\sigma M_{\text{mol}}} \left(\frac{1}{T_e^2} - \frac{1}{(T_e + \Delta T)^2} \right) \geq 1.9 \cdot 10^{12} \text{ s} \quad (4.21)$$

if we consider $T_e = 50 \text{ mK}$ and $\Delta T = 10 \text{ mK}$. We conclude that only a small part of the heat is transported via thermal radiation, since it is plausible that thermalizing happens on timescales $\ll t_{\text{rad}}$. This effect may be responsible for the fluctuations in the RO phase. In order to investigate the effect of thermal radiation caused by the antennas in a precise way, we need to formulate and solve the complete energy balance equation for the system.

Influence of higher transmon qubit levels Another effect that can cause RO phase fluctuations is a population of higher levels of the transmon qubit. The pulse pattern varies from measurement to measurement, implying that the number of pulse edges is not constant. Thus, the pulse patterns look different in frequency space, which means that we can have different resulting higher level excitations that cause additional dispersive shifts. We investigate this effect experimentally by performing ‘‘discrete’’ Rabi oscillations using sequences of Gaussian pulses with a length of $\tau^{\text{dis}} = 40 \text{ ns}$. As a result, we can measure the RO phase only for discrete times $N \cdot \tau^{\text{dis}}$. We then compare the result with an ordinary Rabi oscillation that is measured directly after the discrete Rabi experiment in order to prevent the system suffering from thermally induced fluctuations in the RO phase. The result for the discrete Rabi experiment is depicted in Fig. 4.6. We measure the lowest RO phase $\varphi_1^{\text{dis}} = -7.129^\circ$ for $t^{\text{dis}} = 200 \text{ ns}$. In order to compare this result to the ordinary Rabi oscillation, we have to take into account that the pulse area increases differently with the pulse length for the discrete Rabi oscillations. If t_θ^{dis} (t_θ^{cont}) denotes the θ -time for the discrete (continuous) Rabi experiment, we find $t_\theta^{\text{cont}} = \sqrt{\pi}\sigma(t_\theta^{\text{dis}} - 2t_r) + 2t_r$ with the ramp time t_r and the standard deviation σ . We find $t^{\text{cont}} \simeq 96.7 \text{ ns}$. This corresponds to a RO phase $\varphi_1^{\text{cont}} = -7.131$. In order to investigate the effect of higher levels, we have to correct for the T_1

²We use $\gamma = 0.729 \text{ mJ mol}^{-1} \text{ K}^{-2}$ [49], $\rho = 19.32 \cdot 10^3 \text{ kg m}^{-3}$, $M_{\text{mol}} = 0.197 \text{ kg}$, $d = 1 \cdot 10^{-4} \text{ m}$ [125] and $l = 1 \cdot 10^{-2} \text{ m}$

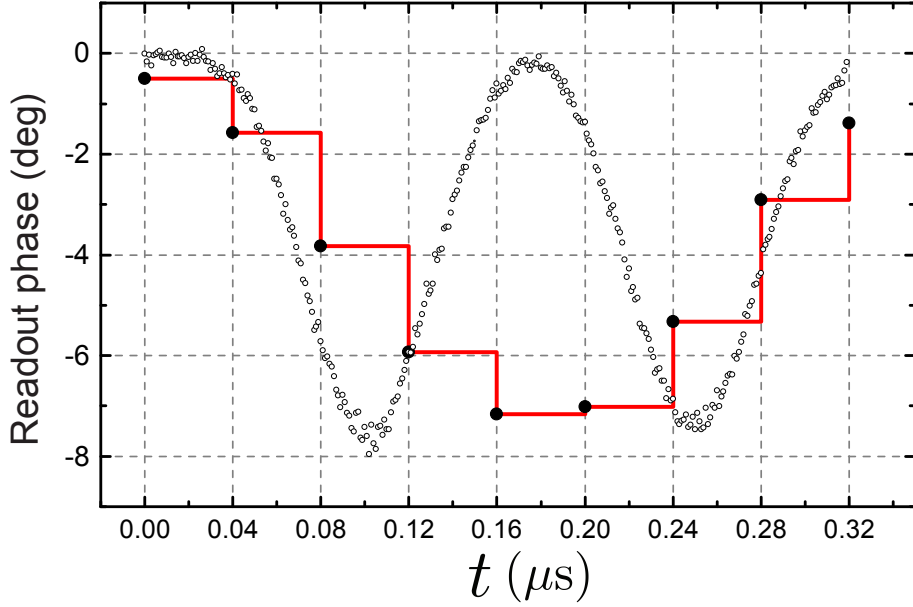


Figure 4.6: Discrete Rabi oscillations for the RO phase using Gaussian pulses with a length of 40 ns respectively. The black dots denote the measured data points. We extract a π -pulse length of $0.2 \mu\text{s}$. For comparison, a continuous Rabi measurement is performed (cf. Fig. 3.7, white dots).

decay during the pulses. We can realize this by calculating the corrected phase ratio

$$R = \frac{\varphi_1^{\text{dis}}}{\varphi_1^{\text{cont}}} \cdot e^{(t_\pi^{\text{dis}} - t_\pi^{\text{cont}})/T_1} \simeq 1.089. \quad (4.22)$$

Ideally, this ratio should be equal to one. Deviations in this quantity must be assigned to differences in the amount of pulse edges. We observe that the pulse pattern may indeed impact the RO phase, since the deviation is on the same order of magnitude. Nevertheless, we have to take into account that the corrected phase ratio also depends on statistical fluctuations in T_1 .

4.3 QST for the quantum memory

In this section, we apply QST to our memory protocol. We prepare the states $|g\rangle$, $|e\rangle$, $|+\rangle$, $|-\rangle$, $|\circ\rangle \equiv 1/\sqrt{2}(|g\rangle - |e\rangle)$ and $|\square\rangle \equiv 1/\sqrt{2}(|g\rangle - i|e\rangle)$, i.e., the pure states with Bloch vector in \hat{z} , $-\hat{z}$, \hat{x} , $-\hat{x}$, \hat{y} and $-\hat{y}$ direction and store them in the cavity mode. We retrieve the state immediately after the storage procedure, i.e. we have $t_s = 0$. After the state retrieval, we reconstruct the density matrix with QST and calculate the distance measures in Tab. 4.5. At first, we store the ground state $|g\rangle$. The results are shown in Fig. 4.7 a). We calculate a fidelity of $f_{|g\rangle} = 0.9035$.

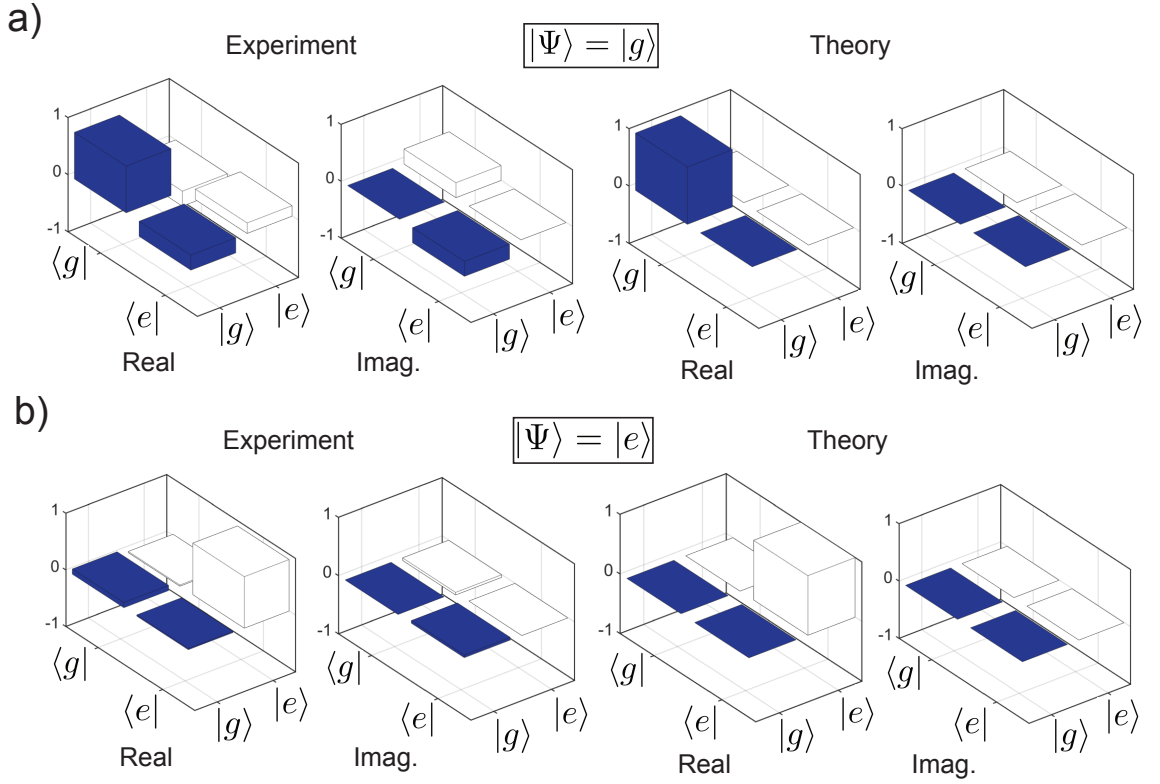


Figure 4.7: Reconstruction of a) the $|g\rangle$ -state and b) the $|e\rangle$ -state after retrieval from the memory

	$ g\rangle$	$ e\rangle$	$ +\rangle$	$ -\rangle$	$ \circ\rangle$	$ \square\rangle$
$D(\rho, \rho_t)$	0.4149	0.1034	0.3455	0.3542	0.3230	0.3190
$1 - f(\rho, \rho_t)$	0.0965	0.0466	0.1633	0.1267	0.1383	0.1442
$B(\rho, \rho_t)$	0.4393	0.3052	0.5714	0.5034	0.5260	0.5370
$C(\rho, \rho_t)$	0.4285	0.3016	0.5476	0.4872	0.5075	0.5173

Table 4.5: Distance measures for the reconstructed states $|g\rangle$, $|e\rangle$, $|+\rangle$, $|-\rangle$, $|\circ\rangle$ and $|\square\rangle$ after storage and retrieval.

After that, we reconstruct the state $|e\rangle$, and depict the results in Fig. 4.7 b). We obtain a fidelity $f_{|e\rangle} = 0.9534$. We observe that we have a significantly higher fidelity for $|e\rangle$, although we have shorter preparation pulse lengths for $|g\rangle$, resulting in a lower amount of depolarization. This can be explained by the fact that only the $|g\rangle$ -population is affected by the memory protocol. The BSB transitions as well as the additional qubit π -pulses of the memory protocol cause additional fidelity losses, which increase with the $|g\rangle$ population of the state.

In the next step, we reconstruct the $|+\rangle$ and the $|-\rangle$ state and show the result in Fig. 4.8 a) and Fig. 4.8 b). We detect $f_{|+\rangle} = 0.8367$ and $f_{|-\rangle} = 0.8733$. We observe fast decay for the off-diagonal elements (coherences) of the density matrices and attribute this either to the BSB transition or to dephasing processes which are probably caused by deexciting the qubit after the first BSB drive and reexciting it for state retrieval. The results for the reconstruction of the $|\circ\rangle$ state and the $|\square\rangle$ state are shown in Fig. 4.8 c) and in Fig. 4.8 d). We measure the fidelities $f_{|\circ\rangle} = 0.8617$ and $f_{|\square\rangle} = 0.8558$ and calculate the remaining distance measures. Again,

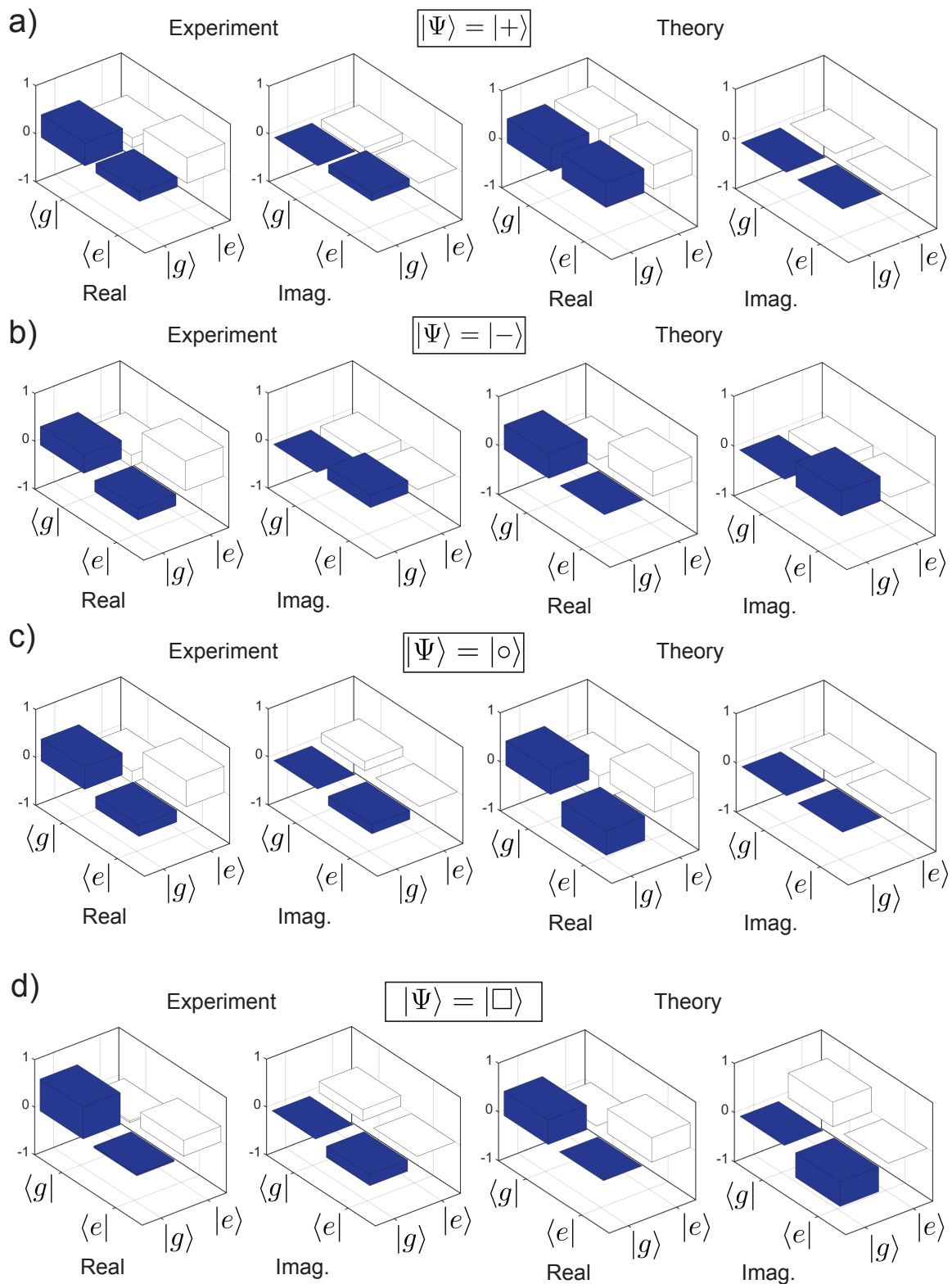


Figure 4.8: Reconstruction of a) the $|+\rangle$ -state and b) the $|-\rangle$ -state, c) the $|\circ\rangle$ -state and d) the $|\square\rangle$ -state after retrieval from the memory

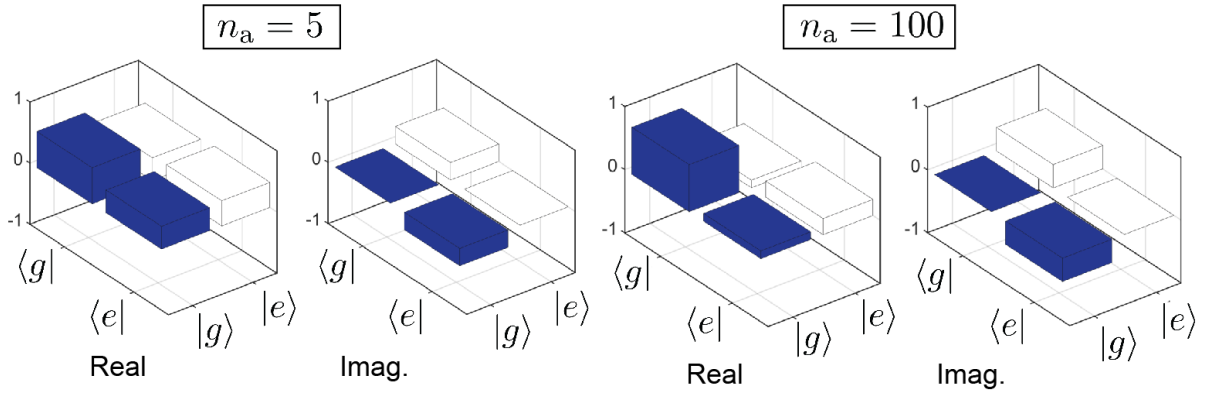


Figure 4.9: Reconstruction of the qubit part of the $|+_{\text{q}}, +_{\text{r}}\rangle$ -state for averaging over n_{a} data points recorded during the RO pulse. The real part of the off-diagonal elements vanishes with increasing n_{a} , indicating that the phase information is lost on short timescales.

we observe that the phase coherence is lost fast in comparison with the benchmarking cases in Sec. 4.1. One reason for this behavior can be found in the number of averages. For several cases, we detect an increase in phase coherence for significantly higher amounts of averages. This implies that it is possible that we have high noise contributions regarding the qubit phase, meaning a large number of averaged measurements is advantageous. Averaging is performed within the RO pulse length of $2.7 \mu\text{s}$, i.e., we take the average over a number of n_{a} data points during this RO time interval. We note, that more averaging results in higher contributions of T_1 -decay, thus decreasing the fidelities of the measurement.

Influence of the BSB transition In order to investigate the fidelity loss caused by the BSB π -pulse, we investigate the qubit when it is prepared with a BSB π -pulse ($|g0\rangle \leftrightarrow |e1\rangle$). We reconstruct the qubit part of $|g,0\rangle$ and $|+_{\text{q}}, +_{\text{r}}\rangle \equiv 1/2(|g,0\rangle + |e,1\rangle)$ and find $f_{|g\rangle}^{\text{BSB}} = 0.9657$ ($n_{\text{a}} = 100$) and $f_{|+\rangle}^{\text{BSB}} = 0.9340$ ($n_{\text{a}} = 5$). We choose this low number of averages for $|+_{\text{q}}, +_{\text{r}}\rangle$ because we observe systematic phase drifts for more averages. For $n_{\text{a}} = 100$, the fidelity reduces to 0.7883. The respective density matrices for $|+_{\text{q}}, +_{\text{r}}\rangle$ for $n_{\text{a}} = 5$ and $n_{\text{a}} = 100$ are depicted in Fig. 4.9. We conclude that the phase coherence is lost on short time scales. Additionally, we observe significant influence of the T_1 -decay, which is a result from the short T_1^{BSB} time. Thus, it is possible that the loss of phase information for the memory protocol is mainly a result from the BSB drive. We guess that it is possible that the enhanced dephasing is a result from noise contributions caused by the relatively high drive power. Alternatively, the dephasing can be a result from the linear phase trend detected in Fig. 3.14. This is plausible since we observe monotonic “swapping” of the coherences from the real to the imaginary part for increasing n_{a} . Furthermore, we observe that the excited resonator may cause dephasing. We state that we are able to reconstruct retrieved states from the memory mode with distance measures clearly below the theoretical limit, although we are limited by decoherence processes.

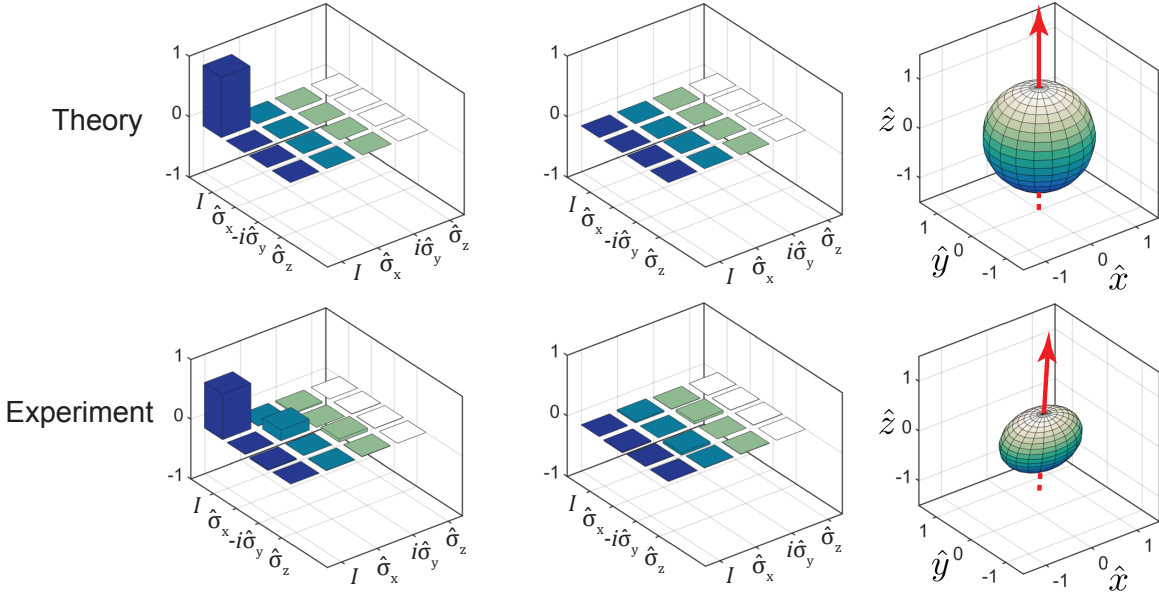


Figure 4.10: Expected and reconstructed process χ matrix for the quantum memory protocol. We observe that the only significant contribution except $I\rho I^\dagger$ is given by $\hat{\sigma}_x \rho \hat{\sigma}_x^\dagger$. The Bloch sphere contracts towards its center and we observe faster decay in z - and y -direction.

4.4 QPT for the quantum memory

Our QPT benchmarking procedure in Sec. 4.2 shows that we are able to accurately characterize single qubit processes. This enables us to reconstruct the χ -matrix for our quantum memory protocol. We store the four basis states $|g\rangle$, $|e\rangle$, $|+\rangle$ and $|-\rangle$ and immediately retrieve them back, implying $t_s = 0$. We then apply the QPT protocol and calculate χ as well as the Bloch sphere after the process. The results are shown in Fig. 4.10. We measure a process fidelity of $f_M \equiv f(\chi, \chi_{I,t}) = 0.8772$. The distance measures are listed in Tab. 4.6. For the purpose of investigating the influence of different pulse shapes, we repeat the same experiment with rectangular pulses with a 1 ns rise time. We observe that the distance measures get significantly worse for rectangular pulses. When evaluating the distance measures for the data in Fig. 4.10, we observe that we are well below the distance limits. In order to correct for the fidelity losses due to QPT pulses, we can reconstruct the identity χ_I directly before reconstructing the memory process χ and calculate the fidelity $f(\chi, \chi_I)$. In the ideal case, the difference to one is just caused by decoherence and errors induced by the memory protocol. We compare the principle of the procedure to a four point resistivity measurement, where we are interested in the resistance of the respective material without contact resistances and the resistances of the cables, respectively [128]. We compare the reconstructed process matrix χ for the memory with the result χ_I obtained in Fig. 4.4 a) and obtain $f(\chi, \chi_I) = 0.947$. This result may be not very accurate since the measurements are not performed in a directly consecutive manner.

	D	$1 - f$	B	\mathcal{C}	$\ \mathcal{E} - \mathcal{E}_{\text{id}}\ _{\diamond}$
Flat-top Gaussian	0.2344	0.1238	0.4956	0.4802	0.2099
Rectangular	0.6264	0.3883	0.8812	0.7911	0.5632
$\text{dist}(\chi, \chi_{*,t})$	0.5144	0.2366	0.6879	0.6460	—

Table 4.6: Distance measures for the reconstructed memory process. The first two rows show the results for two different pulse shapes. The distance measures with respect to the CDP are listed in the fourth row.

Estimation of uncertainties for the fidelity In order to estimate the uncertainty in fidelity for this measurement, we derive an explicit expression for $f(\{\varphi_i^{(j)}\})$, where $\varphi_i^{(j)}$ denotes the RO phase and $i \in \{|g\rangle\langle g|, |e\rangle\langle e|, |+\rangle\langle +|, |-\rangle\langle -|\}$, $j \in \{x, y, z\}$. The nomenclature is chosen in a way that $\varphi_i^{(j)}$ is the RO phase for the projection measurement onto the j -axis for the prepared input state i . We exploit that the ideal memory process is an identity, yielding $f(\chi, \chi_{I,t}) = \sqrt{\chi_{11}}$. We define $\varphi \equiv (\varphi_{|g\rangle\langle g|}^{(x)}, \varphi_{|g\rangle\langle g|}^{(y)}, \dots, \varphi_{|-\rangle\langle -|}^{(z)})^T \equiv (\varphi_1, \varphi_2, \dots, \varphi_{12})$ and obtain (cf. Sec. B.2 in the appendix)

$$f(\{\varphi_i^{(j)}\}) = \frac{1}{2} \sqrt{1 + \frac{\mathbf{a} \cdot \varphi}{\varphi_g - \varphi_e}} \quad (4.23)$$

with $\mathbf{a} \equiv (1, -1, 1, 1, -1, -1, -2, 0, 0, 0, 2, 0)^T$. Propagation of error then translates the error in RO phase to uncertainty in fidelity

$$\Delta f = \frac{1}{8(\varphi_g - \varphi_e)f(\{\varphi_i^{(j)}\})} \sqrt{\sum_k (a_k \Delta \varphi_k)^2 + \left(\frac{\mathbf{a} \cdot \varphi}{\varphi_g - \varphi_e} \Delta \varphi_e \right)^2} \quad (4.24)$$

where $\Delta \varphi_k$ denotes the uncertainty for the RO phase with index k and $\Delta \varphi_e$ labels the uncertainty for the φ_e phase obtained from the calibration measurements. For the measurement results depicted in Fig. 4.10, we obtain $\Delta f \simeq 0.025$. Equation (4.23) gives us the opportunity to estimate the corrected fidelity f^c from the uncorrected fidelity f . In the correction, we take into account losses resulting from depolarization, on a time scale T_1 . Our system is T_1 -limited, hence we only consider energy decay. We use the approximation that each RO phase φ_k decays with a factor $e^{-\tau/T_1}$, where τ is the length of the pulse. This yields

$$f^c \simeq \frac{1}{2} \sqrt{1 + \frac{\mathbf{a} \cdot \varphi}{\varphi_g - \varphi_e} e^{\frac{\tau}{T_1}}} = \frac{1}{2} \sqrt{1 + (4f^2 - 1)e^{\frac{\tau}{T_1}}}. \quad (4.25)$$

For a protocol consisting of N pulses, where each pulse has a length τ_i and a decay time $T^{(i)}$ for $1 \leq i \leq N$, we conclude via induction that

$$f^c = \frac{1}{2} \sqrt{1 + (4f^2 - 1) \prod_{i=1}^N e^{\frac{\tau_i}{T^{(i)}}}}. \quad (4.26)$$

For our memory protocol with $N = 4$, we obtain $\prod_{i=1}^N e^{\tau_i/T^{(i)}} = e^{t_{\text{BSB}}/T_1^{\text{BSB}}} \cdot e^{t_q/T_1^q}$ where t_{BSB} (t_q) is the total length of the two BSB (qubit) pulses. From Eq. (4.26), we estimate a corrected fidelity of $f^c \simeq 0.966$.

In Fig. 4.10, we observe that only χ_{11} and χ_{22} are significantly larger than 0. As a result, we can model the resulting process as $\mathcal{E}(\rho) \simeq (1-p)I\rho I^\dagger + p\hat{\sigma}_x\rho\hat{\sigma}_x^\dagger$ with the constant p [12]. We compare this with the CDP described by Eq. (2.33) and hence interpret the $\hat{\sigma}_x\rho\hat{\sigma}_x^\dagger$ term as depolarization towards x and p as the respective probability, where we assume Markovian behavior. Regarding the dephasing process (cf. Fig. 2.13), we can state that the term corresponds to dephasing in the yz -plane. Thus, we expect the Bloch sphere to contract towards the x -axis, which is consistent with the behavior of the Bloch sphere in Fig. 4.10. This is probably a technical artifact, resulting from differences in the I and Q channel. According to Eq. (3.1), a rotation about the x -axis corresponds to the RF quadratures $I = 0$ and $Q = A$ [cf. Eq. (3.1)]. A higher dephasing rate about x , compared to the y -axis, can then be a result from the Q -channel adding more noise to the system than the I channel. Especially, it is possible that I and Q show different on/off ratios, yielding asymmetries regarding the depolarization behavior. Another explanation for this behavior is the BSB drive, which is always performed with a fixed phase. It is possible that the RF source for the BSB pulses adds phase sensitive noise, disturbing the symmetry of the Bloch sphere. Possibly, this may be a result from the linear trend detected in Fig. 3.14.

In order to investigate whether the asymmetry with respect to dephasing is reproducible, we repeat the QPT experiment for the memory protocol for 25 times. From these results, we calculate an average corrected fidelity of $f^c = 0.886 \pm 0.065$. We measure deviations in the experimental outcomes, especially regarding the diagonal elements of χ . This implies that depolarization behaves different for each measurement and we may ask whether this yields well defined results. We are able to divide the reconstructed χ -matrices into three different categories, as depicted in Fig. 4.11. We introduce the parameter $n \in \{1,2,3\}$, which denotes the number of diagonal elements of χ which are significantly different from zero. n is a measure for the symmetry of the depolarization process, i.e., $n = 1$ means that we mainly lose coherence in one plane (xy , xz , yz) of the Bloch sphere, $n = 2$ implies a loss of coherence in two planes and $n = 3$ states that depolarization takes part for all directions. For the 25 QPT measurements, we obtain 16 times $n = 1$, seven times $n = 2$ and two times $n = 3$. We additionally observe that the measured fidelities are independent of n , implying that the total fidelity loss due to decoherence is the same for each measurement, whereas only the phase distribution of the decoherence process differs. A possible explanation for this behavior is that the RF source adds the same amount of noise for each QPT experiment, which is from measurement to measurement differently distributed to the I and Q channels. Furthermore, we observe that for a fixed n , each of the n diagonal elements different from 0 that correspond to $\hat{\sigma}_x$, $-i\hat{\sigma}_y$ or $\hat{\sigma}_z$ have approximately the same value, which we label δ . For example, for $n = 2$, we obtain $\delta = \chi_{22} \simeq \chi_{33}$.

In order to calculate the loyalty ξ of the protocol, we need to calculate the corrected fidelity with respect to the CDP. We use the previously described characterization by n to approximate this quantity. From the definition of the fidelity, Eq. (2.50), it follows that $f_* \equiv f(\chi, \chi_*) = 1/2 \cdot \text{Tr} \sqrt{\chi}$ [68]. We assume that χ is diagonal, which is consistent with the measurement data. For most of the reconstructed χ -matrices, we observe that the off diagonal elements are small compared to the diagonal elements which are significantly larger than zero. Thus, $f(\chi, \chi_*) \simeq 1/2 \cdot (\sqrt{\chi_{11}} + n \cdot \sqrt{\delta})$. From $\text{Tr}\chi = 1$, we conclude $\delta = (1 - \chi_{11})/n$. This allows us to calculate f_* as a function of the

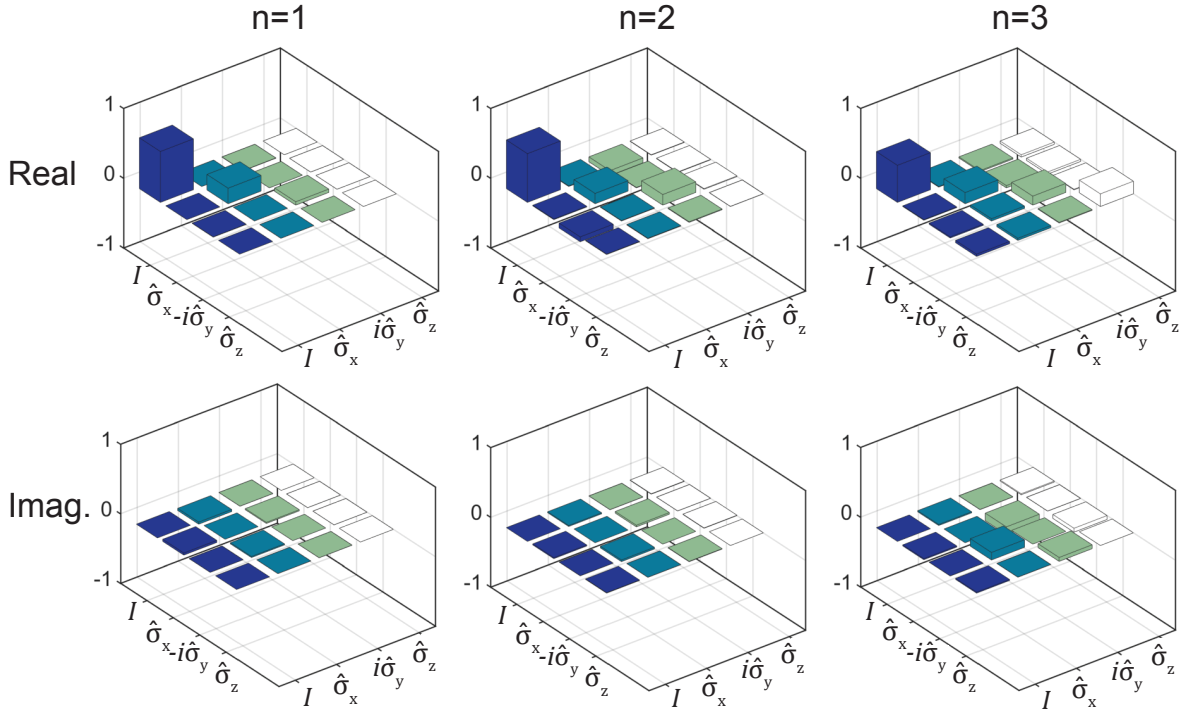


Figure 4.11: Three categories of measurement results for the χ -matrix of the memory protocol. We distinguish the categories by $n \in \{1,2,3\}$

process fidelity

$$f_* = \frac{1}{2}(f + \sqrt{n} \sqrt{1 - f^2}). \quad (4.27)$$

We use Eq. (4.26) to calculate the corrected fidelity f_*^c with respect to the CDP

$$f_*^c \simeq \frac{1}{4} \sqrt{1 + (4f^2 - 1) \prod_{i=1}^N e^{\frac{\tau_i}{T^{(i)}}}} + \frac{\sqrt{n}}{2} \sqrt{3 - (4f^2 - 1) \prod_{i=1}^N e^{\frac{\tau_i}{T^{(i)}}}}. \quad (4.28)$$

This allows us to calculate a loyalty of $\xi = 0.16 \pm 0.11$. We conclude that despite the direction of the depolarization is randomly distributed, the reconstructed process is well defined since ξ is significantly larger than 0 and larger than the threshold of 10% which we define in Sec. 2.4.3. In order to further characterize the quantum memory process, we repeat the characterization measurements for rotations that are performed in Sec. 4.2, but insert the memory protocol between the rotation pulse and the QST pulses, which means that the result from the rotation process is stored and regained before performing QST. In Fig. 4.12, we plot the result of the $\hat{R}_x(\pi/2)$ rotation. We measure a fidelity $f_{\hat{R}_x(\pi/2, M)} = 0.8310$. The distance measures are listed in Tab. 4.7

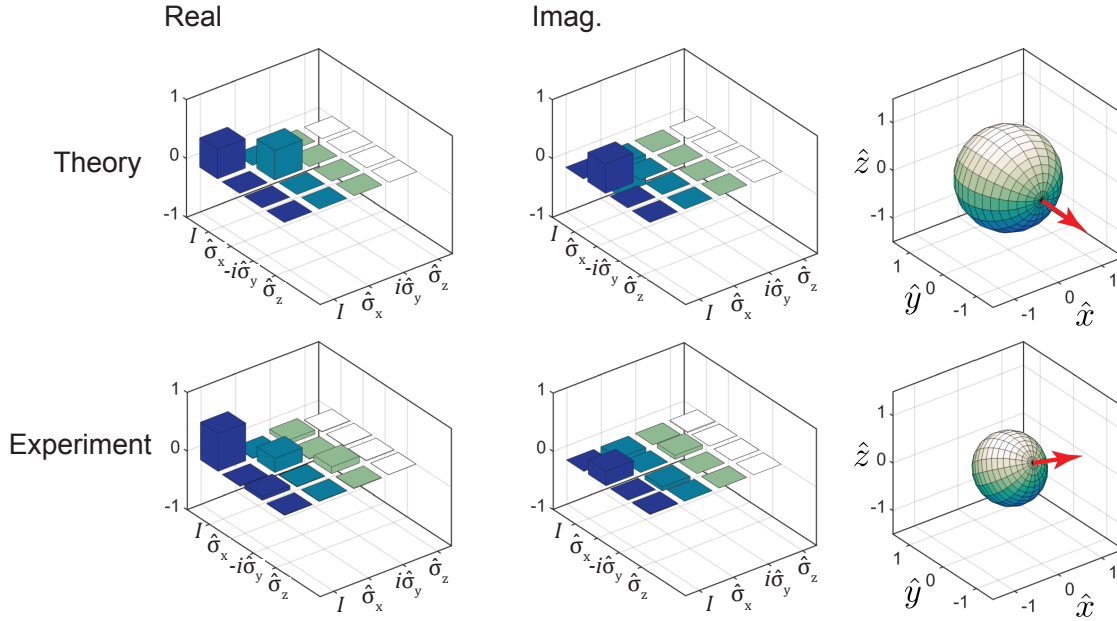


Figure 4.12: Rotation by $\pi/2$ about the x -axis. After the rotation process, the resulting state is stored in the memory mode and retrieved.

$D_{\hat{R}_x(\pi/2,M)}$	$1 - f_{\hat{R}_x(\pi/2,M)}$	$B_{\hat{R}_x(\pi/2,M)}$	$C_{\hat{R}_x(\pi/2,M)}$
0.3973	0.1690	0.5815	0.5563

Table 4.7: Distance measures for the reconstruction of a rotation by $\pi/2$ about the x -axis followed by the memory protocol.

We observe that the Bloch sphere rotates by an angle smaller than $\pi/2$. We explain this behavior with the enhanced dephasing about the x -axis, caused by the memory protocol. The χ -matrix displays this result with $|\chi_{11}| < |\chi_{22}|$. We repeat the experiment for a π -pulse about the y -axis [$\hat{R}_y(\pi)$] and for a $\pi/2$ -pulse about the y -axis [$\hat{R}_y(\pi/2)$] and obtain the fidelities $f_{\hat{R}_y(\pi),M} = 0.7060$ and $f_{\hat{R}_y(\pi/2),M} = 0.7095$. We observe that these values are worse than the fidelities obtained in the benchmarking procedure, which is again a result from increased decoherence due to longer pulse sequences and from the dephasing processes that occur during the memory protocol.

4.5 Time-resolved tomography of the memory

As shown in Sec. 4.4, we are able to completely characterize the quantum memory process with QST. However, as stated in Sec. 2.3.2, QPT has the disadvantage that the process is treated as a black box [14]. Within this section, we want to get access to the dynamical evolution of χ , which means that we want to obtain $\chi(t_s)$, where t_s is the time for which the respective state is stored in the storage mode. We thus vary t_s and reconstruct the resulting process matrix for a set of times $\{t_s^{(i)}\}$ with QPT. Intuitively, we expect that the fidelity $f(\chi(t_s), \chi_{I,t})$ decays exponentially with t_s . In order to enhance the performance of the procedure, we exploit this behavior and exponentially increase the spacing between the t_s for which we reconstruct the process [88, 96]. We choose a total time T , an initial time interval Δt and an amount of sample points N . We set $t_s^{(i)} = \Delta t \cdot 2^i$ and obtain a relation between T , Δt and N using

$$T = \Delta t \sum_{i=0}^{N-1} 2^i = \Delta t(2^N - 1). \quad (4.29)$$

In order to be able to compare the measured data with the predicted time evolution of χ during storage, we simulate the memory protocol using the Lindblad master equation Eq. (2.5). We solve the system of equations in Eq. (2.61) for the driven qubit, the BSB transition and for energy decay and dephasing for the non-driven system. For the driven qubit, we use Eq. (2.62) for the unitary part and Eq. (2.63) for the non-unitary evolution. Equation (2.63) additionally models the decay of the non-driven system. A more detailed discussion can be found in Chap. D in the appendix. The BSB transition for the qubit is modelled by using the Hamiltonian Eq. (2.17) in its matrix form, Eq. (2.18), and tracing out the resonator term. Similar to Eq. (2.62), we rewrite this contribution as

$$\hat{\mathcal{H}}_{\text{BSB}} = A \sqrt{n+1} \begin{pmatrix} 0 & -1 & 1 & 0 \\ -1 & 0 & 0 & 1 \\ 1 & 0 & 0 & -1 \\ 0 & 1 & -1 & 0 \end{pmatrix}. \quad (4.30)$$

³ Since we do not exactly know the attenuation caused by the RF source, the RF lines and the cryogenic setup, we choose the value for Ω_d in a way that the simulated Rabi oscillations show the same period as in experiment. This is the case for $\Omega_{d,q}^{\text{sim}}/2\pi \simeq 5.01$ MHz. A similar procedure is performed for the BSB transition, and we choose the constant A in a way that the Rabi frequency in simulation coincides with the measured Rabi frequency. This is the case for $A^{\text{sim}}/2\pi\hbar = 3.21$ MHz.

We check consistency by considering the definition of A in Eq. (2.17). For g , ω_q and ω_b , we take the values from the characterization experiments in Sec. 3.3. We use $\omega_m/2\pi = 8.708$ GHz [108]. The drive power $\Omega_{d,\text{BSB}}$ is calculated from the drive power Ω_d^{sim} . In experiment, the BSB transition is driven with $L_p^{\text{BSB}} = 21$ dBm and for the qubit, we have $L_p^q = -40$ dBm. We have

³We benchmark the simulations for the driven system with the initial condition $\rho_i = |g\rangle\langle g|$ and observe the expected damped Rabi oscillations, decaying on the timescale T_1 .

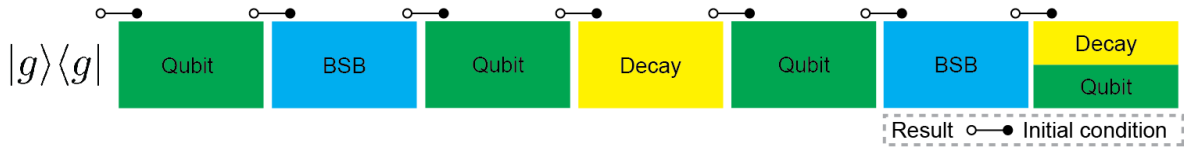


Figure 4.13: Schematic illustration of the simulation of the memory protocol. We use $|g\rangle\langle g|$ as initial input. The first qubit pulse serves for state preparation. The memory protocol is then simulated step by step. The last step is necessary for QST, which either consists of free decay or a qubit $\pi/2$ -pulse.

to take into account that the qubit RF line contains an additional combiner with an attenuation of 3 dBm (cf Fig. 3.3). Thus, we state that $\Omega_{d,\text{BSB}}^{\text{sim}} = \Omega_{d,q}^{\text{sim}} \cdot 10^{(L_p^{\text{BSB}} - L_p^q - 3 \text{ dBm})/20}$. Altogether, we calculate $A/2\pi\hbar = 2.71 \text{ MHz}$. We obtain $A^{\text{sim}}/A \simeq 1.6954$. We use this as an indicator that our results are consistent, since we make use of several approximations for estimating A^{sim}/A . Deviations in this ratio can be assigned to measurement uncertainties, especially in g , which may have high impact due to $A \propto g^3$. Furthermore, for the estimation of $\Omega_{d,\text{BSB}}$, we include all differences in the RF cabling and attenuation at room temperature as compared to the qubit drive line. However, we do not take into account that there may be additional deviations in the impedances of the BSB and the qubit RF lines. Furthermore, we assume that we have pure rectangular pulses in the simulation, whereas we use flat-top Gaussian pulses in the experiment.

We simulate the memory protocol by starting in $|g\rangle\langle g|$ and we solve the Lindblad equation step by step for the respective pulse sequence, i.e., we use the result from the i th pulse as initial condition for the $(i+1)$ th pulse, as illustrated in Fig. 4.13. For reconstructing the behavior of $\chi(t_s)$ for $0 \leq t_s \leq T_s$, we consider Eq. (4.29) and choose $\Delta t = 10 \text{ ns}$, $T = 5.12 \mu\text{s}$, yielding $N = 11$. In order to obtain more accurate results, we additionally reconstruct the $\chi(t_s)$ for $t_s \in \{1.7 \mu\text{s}, 2.2 \mu\text{s}, 3.5 \mu\text{s}, 4.0 \mu\text{s}\}$, however, we only estimate the errors for the data points corresponding to the exponentially increasing times t_s due to better performance. We plot the fidelities $f(\chi(t_s), \chi_{I,t})$ in Fig. 4.14 and adopt an exponential fit to the data (red curve). For comparison, we additionally plot the results of our simulation (blue curve). We observe that the simulated curve reproduces the behavior of the measurement and that the simulated values lie within the error bars for most of the data points. From the fit curve, we observe that the measured fidelities are worse than the ones obtained from the simulation. This behavior is expected, since there may be additional sources of decoherence which we do not take into account in our simulation. We observe that the difference of the fidelity curves is approximately equal to the value $\Delta f = 3\%$ measured in Sec. 4.1. Furthermore, discrepancies may also result from the fact that, in the simulation, we assume that our transmon qubit is an ideal TLS. Hence, we neglect effects resulting from the low anharmonicity and higher levels, such as state leakage [35]. This is probably the explanation why the simulated values for $t_s = 0$ are higher than the measured results. Another reason for the deviation is the fact that we use pure rectangular pulses for the simulation, neglecting that the pulse lengths may slightly differ from the ones used in experiment. Furthermore, decoherence during the RO pulse is not taken into account. From Sec. 3.3 and Sec. 3.4, we observe the existence of fluctuations in the decay times. We include this statistical effect into the simulation by assuming that the T_1 -times are normally distributed with

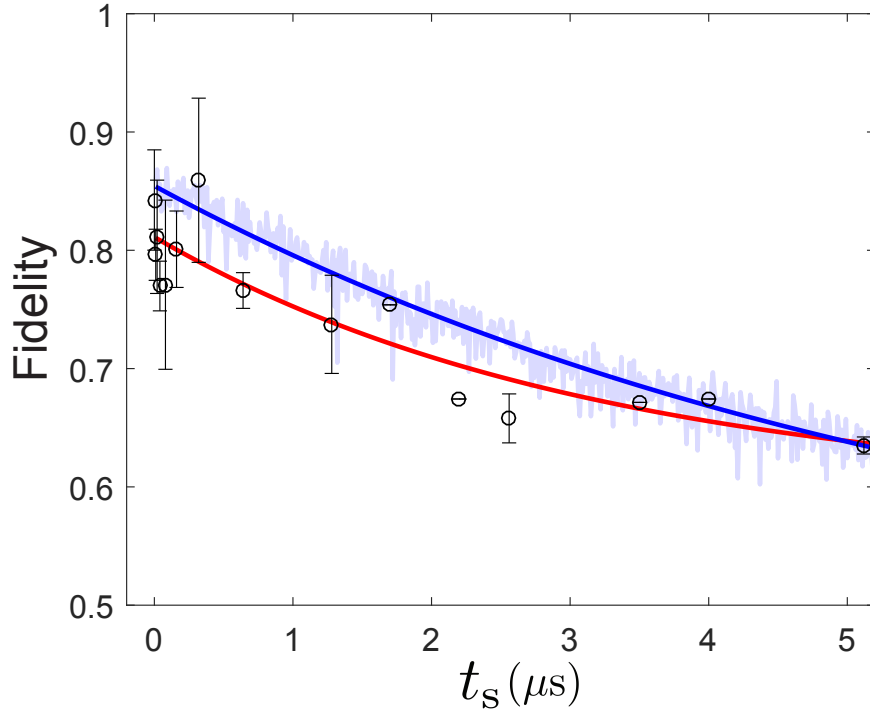


Figure 4.14: Exponential decay of the measured fidelity. The red curve is a fit to the experimental results, whereas the blue curve results from a master equation simulation of the system. We take into account that the decay times are normal distributed, which yields fluctuations of the fidelity (light blue).

a standard deviation given by the estimated statistical uncertainty. The resulting fluctuations of the fidelity are shown in Fig. 4.14, and we observe that these variations in the T_1 -times are a possible explanation for the divergence of the measurement points, especially regarding the measurement uncertainties in fidelity of up to ± 0.08 . Nevertheless, we observe that our measured data points are still below the theoretically expected values.

We compare the simulated χ -matrix for $t_s = 0 \mu\text{s}$ with the QPT result in Fig. 4.10 and calculate the fidelity $f(\chi_{\text{sim}}(0 \mu\text{s}), \chi_{\text{exp}}(0 \mu\text{s})) = 0.95$. We observe that for this case, the total degree of decoherence (i.e., the deviation of χ_{11} from one) is similar for the simulated and the reconstructed process. The fact that the asymmetric behavior of decoherence described in Sec. 4.4 is not reproduced by the simulation substantiates the hypothesis that this might be a result from asymmetries regarding the I and Q channel.

We compare the χ -matrices for the experimental and the simulated process for times similar to or larger than T_s . In order to interpret the results, we have to state that for $t_s \rightarrow \infty$, the memory protocol does not reproduce the CDP, but a contraction of the Bloch sphere towards its south pole, i.e. a reverted T_1 -decay. We understand this with the energy level scheme from Fig. 2.18 a). For $t_s \gg T_s$, every stored state ends up in $|g, 0\rangle$ before retrieval. The qubit π -pulse of the retrieval sequence then yields the state $|e, 0\rangle$, which is not affected by the second BSB pulse.

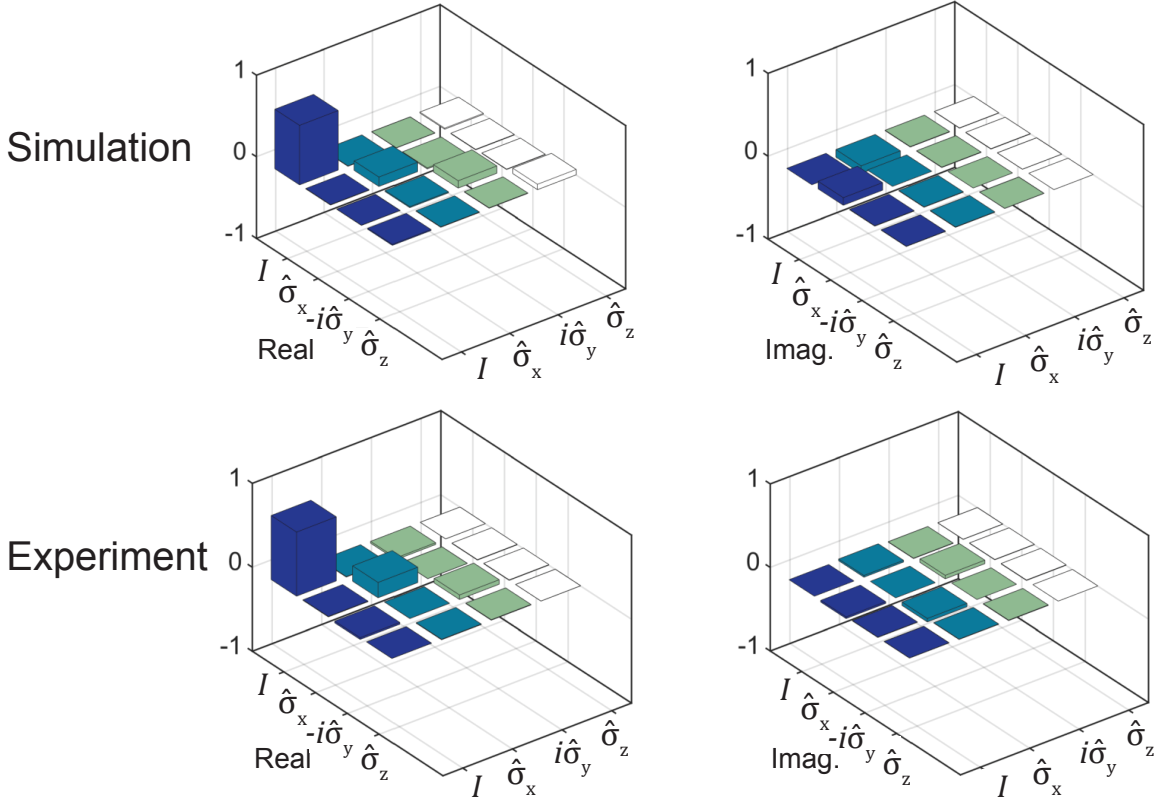


Figure 4.15: Comparison of the simulated and the measured process matrix for $t_s = 0$. In the simulation, the decoherence is similarly distributed to $\chi_{\text{sim},22}$, $\chi_{\text{sim},33}$ and $\chi_{\text{sim},44}$, whereas in the experiment, we observe that mainly $\chi_{\text{exp},22}$ is affected. The total degree of decoherence is similar for the simulated and the measured case.

Let χ_{sp} be the process matrix for the quantum process \mathcal{E}_{sp} that maps every quantum state ρ to the south pole $|e\rangle\langle e|$, i.e., $\mathcal{E}_{\text{sp}}(\rho) = |e\rangle\langle e|$ for arbitrary ρ . Inserting the process outcome into Eq. (2.41) and using Eq. (2.46) gives

$$\chi_{\text{sp}} = \frac{1}{4} \begin{pmatrix} 1 & 0 & 0 & -1 \\ 0 & 1 & 1 & 0 \\ 0 & 1 & 1 & 0 \\ -1 & 0 & 0 & 1 \end{pmatrix}. \quad (4.31)$$

We perform a similar calculation for the process \mathcal{E}_{np} that maps arbitrary states ρ to the north pole of the Bloch sphere [12], i.e., conventional T_1 -decay for times $t \rightarrow \infty$. The corresponding process matrix reads

$$\chi_{\text{np}} = \frac{1}{4} \begin{pmatrix} 1 & 0 & 0 & 1 \\ 0 & 1 & -1 & 0 \\ 0 & -1 & 1 & 0 \\ 1 & 0 & 0 & 1 \end{pmatrix}. \quad (4.32)$$

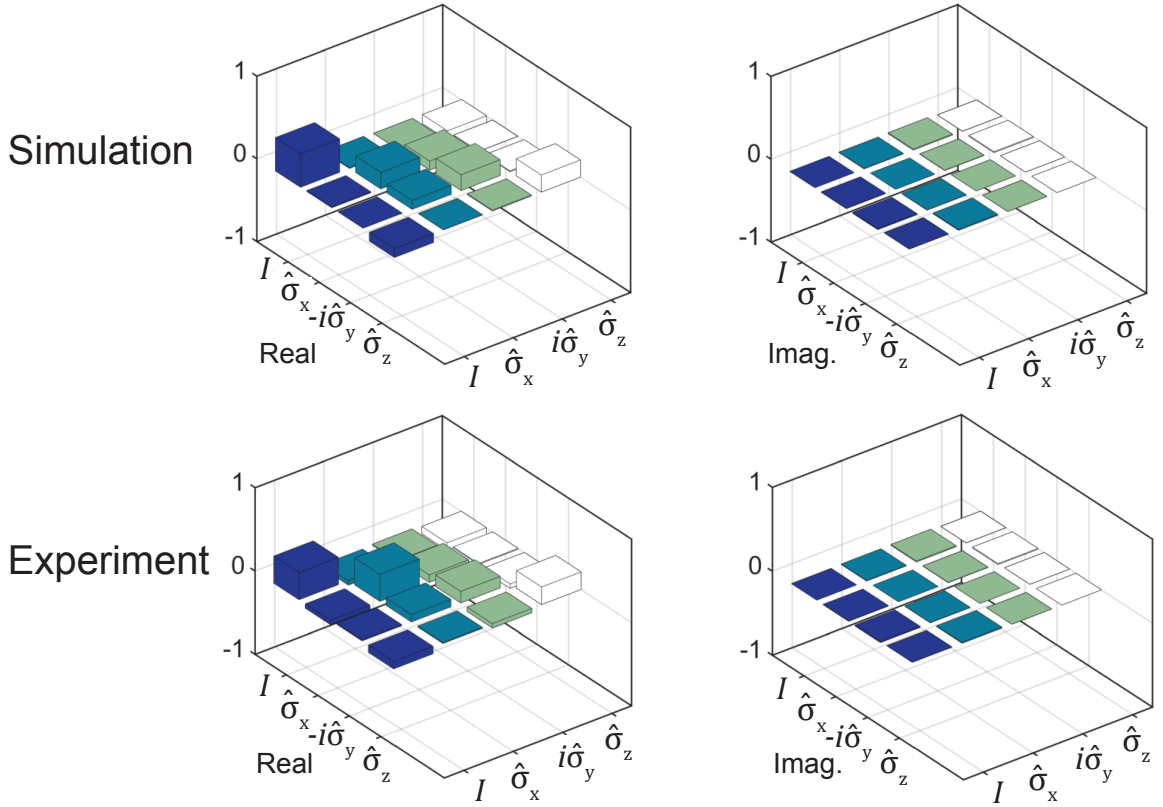


Figure 4.16: Simulated and reconstructed process matrix for $t_s = 5.12 \mu\text{s}$. The reverted T_1 decay during storage is observable for both cases.

We depict the simulated and one of the measured process matrices for $t_s = 5.12 \mu\text{s}$ in Fig. 4.16. For this measurement, we calculate a fidelity of $f[\chi_{\text{sim}}(5.12 \mu\text{s}), \chi_{\text{exp}}(5.12 \mu\text{s})] = 0.975$. We especially observe contributions of the reverted T_1 decay described by Eq. (4.31). The distance measures are listed in Tab. 4.8

D	$1 - f$	B	C
0.2006	0.025	0.2224	0.2210

Table 4.8: Distance measures for the comparison of the reconstructed and the simulated process matrix for $t_s = 5.12 \mu\text{s}$.

In Tab. 4.9, we compare the experimental result with the ideal process χ_I (first row). In order to interpret the distance measures for this process, we need to adopt the limits in a way that we do not compare the ideal memory protocol with the CDP but with Eq. (4.31) and Eq. (4.32). These limits correspond to a T_1 decay for $t \rightarrow \infty$ and we label them with subscript ∞ . We list the results in Tab. 4.9. For the theoretical limits, we only consider T_1 decay, neglecting different types of decoherence processes during the RF pulses.

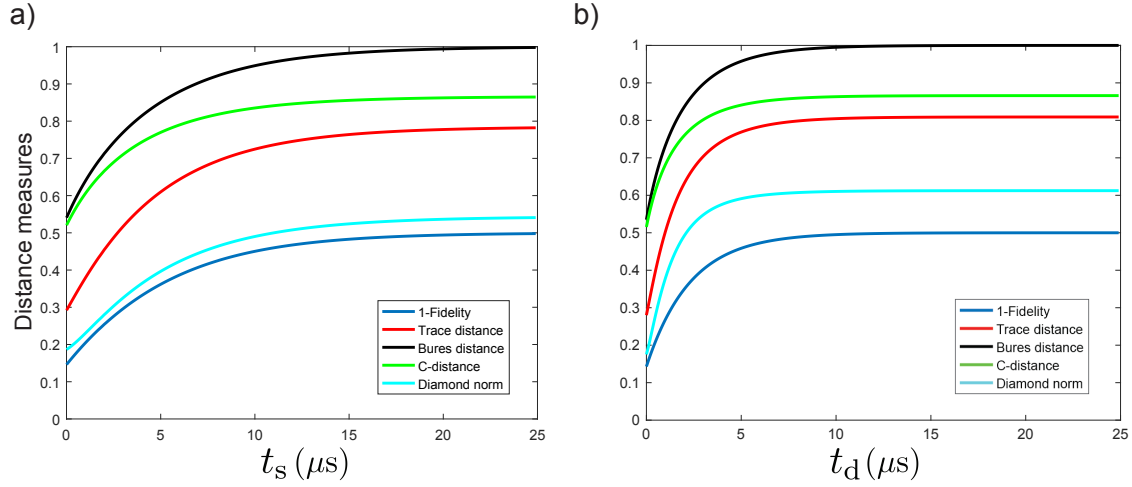


Figure 4.17: a) Simulated distance measures depending on the time t_s . The distance measures converge for $t_s \gg T_s$. b) Simulated distance measures as a function of the time t_d between the memory protocol and the QST pulse.

	D	$1 - f$	B	\mathcal{C}	$\ \cdot\ _{\diamond}$
$t_s = 5.12 \mu s$	0.6855	0.4285	0.9257	0.8206	0.4488
$t_s \rightarrow \infty$ (Theory)	$\Phi/2 \simeq 0.809$	1/2	1	$\sqrt{3}/2 \simeq 0.866$	$\sqrt{6}/4 \simeq 0.612$

Table 4.9: Distance limits for the comparison of the ideal memory process and T_1 decay for timescales $t \rightarrow \infty$.

Where $\Phi \simeq 1.618\dots$ denotes the golden ratio [115]. We verify these limits with our simulation. In Fig. 4.17 a), we plot the distance measures for increasing time t_s . Figure 4.17 b) shows the simulated distance limits depending on the time t_d between last BSB pulse of the memory protocol and the QST pulse, i.e. we apply the memory process, wait for a time t_d and then reconstruct the result. We state that for our conventions, we always have $1 - f \leq \|\cdot\|_{\diamond} \leq D \leq \mathcal{C} \leq B$, which is consistent with our measurement results. In Tab. 4.10, we summarize the distance measures for $t_d = t_s = 25 \mu s$.

	D	$1 - f$	B	\mathcal{C}	$\ \mathcal{E} - \mathcal{E}_{id}\ _{\diamond}$
$t_s = 25 \mu s$	0.7822	0.4979	0.9979	0.8648	0.5409
$t_d = 25 \mu s$	0.8090	0.500	1.000	0.8660	0.6124

Table 4.10: Distance measures for the simulated process matrices after $t_s = 25 \mu s$ and $t_d = 25 \mu s$ with respect to the ideal memory process.

We observe that the fidelity and the resulting Bures and \mathcal{C} -distance are close to the limit in Tab. 4.10 for both cases, whereas in the case of varying t_s , the trace distance and the diamond norm converge to values smaller than the predicted limit for T_1 -decay and larger than their limit for depolarization. An explanation is that the fidelity only depends on the height of χ_{11} , which implies that it does not differ between T_1 decay and depolarization towards the CMS and, hence, always converges to the same limit. The trace distance and the diamond norm are additionally affected by the off-diagonal elements, which is reflected by the fact that they have different

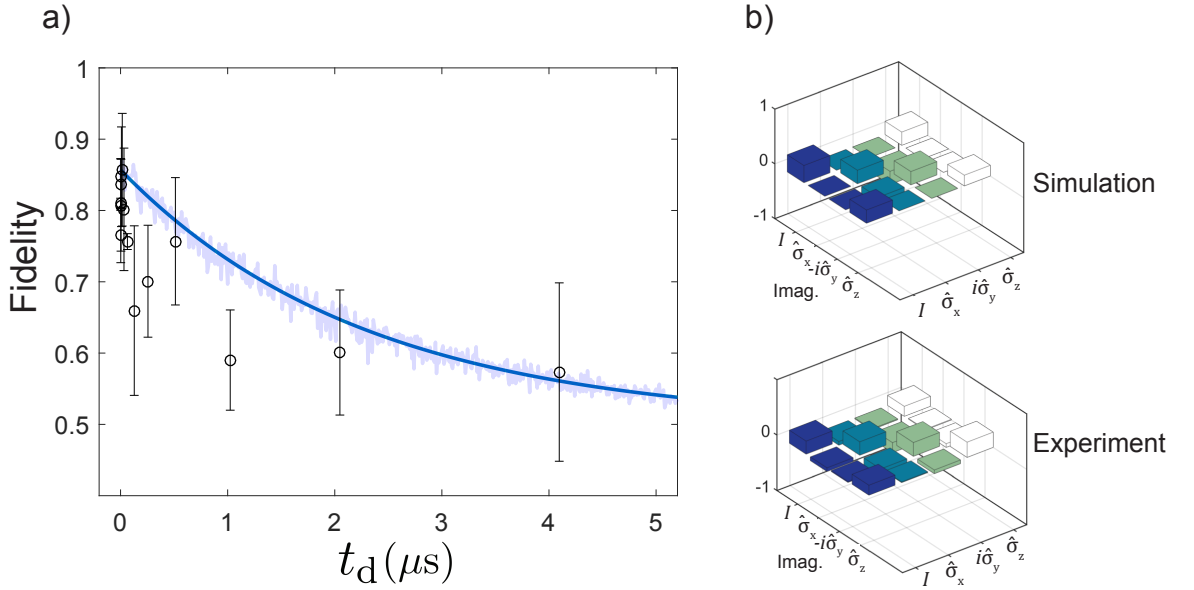


Figure 4.18: a) Fidelity of the reconstructed process, depending on the time t_d between the memory protocol and the QST pulses. The blue curve is a result of the master equation simulation. Fluctuations in fidelity resulting from statistical variations in the decay times are shown in light blue. b) Real part of the simulated and measured process matrix for $t_d = 4.096 \mu\text{s}$. All matrix elements of the imaginary part are negligibly small.

distance limits for energy relaxation and depolarization. Thus, the resulting limit consists of contributions from depolarization during the drive pulses as well as from pure energy decay. In the next step, we vary the time t_d between the memory protocol and the QST pulses. Starting from Eq. (4.29), we choose $\Delta t = 1 \text{ ns}$, $N = 14$, implying $T = 4.12 \mu\text{s}$. The result is depicted in Fig. 4.18 a), together with the simulated fidelities (blue curve). In Fig. 4.18 b), we depict the reconstructed process matrix with $t_d = 4.096 \mu\text{s}$ as well as the simulated result. For the two matrices in Fig. 4.18 b), we find the fidelity $f[\chi_{\text{sim}}(4.096 \mu\text{s}), \chi_{\text{exp}}(4.096 \mu\text{s})] = 0.9493$. Furthermore, we compare the experimental outcome for $t_d = 4.096 \mu\text{s}$ with the ideal process χ_I . We find the distances that are listed in Tab. 4.11

D	$1 - f$	B	\mathcal{C}	$\ \cdot\ _{\diamond}$
0.8009	0.5151	1.015	0.8746	0.5566

Table 4.11: Distance measures for the comparison of the reconstructed and the ideal process matrix for $t_d = 4.096 \mu\text{s}$.

We observe that we reach the predicted distance limits. Discrepancies regarding the trace distance and the diamond norm are again a result from depolarization during the QST pulses. Similar to Fig. 4.14 a), we observe that the fidelities for the reconstructed state are located below the simulated fidelity curve. We explain this again with the fact that there may be sources of decoherence in the experiment that are not included in the simulation.

Chapter 5

Summary and outlook

In this thesis, we use quantum state tomography (QST) and quantum process tomography (QPT) to characterize a quantum memory consisting of a transmon qubit placed in a 3D cavity resonator. The working principle of the quantum memory is based on the multimode structure of the cavity, and we use different electrical modes for readout and storage, respectively. In order to understand QPT, we introduce the relevant physical concepts as well as the theory of a quantum process, which can be interpreted as a displacement, followed by a deformation and a rotation of the Bloch sphere in the single qubit case. Furthermore, we discuss how we can compare quantum states and quantum processes mathematically.

Characterization measurements for the qubit and the quantum memory setup yield the coupling constants as well as the decay rates and the required pulse lengths. For the qubit, we obtain $T_1 = 1.21 \mu\text{s}$ and a dephasing time $T_\varphi \gg T_1$, implying that we are limited by energy decay. The memory decays with $T_1^{\text{s}} \approx 4.3T_1$, showing that we are able to significantly enhance the decay time. We realize a pulse protocol for QST and benchmark the routine by reconstructing pure and mixed single qubit states with fidelities close to one. We investigate the phase dependence of the quality of our QST protocol and prove that the *IQ* control works properly. After that, we implement a QPT protocol, which is successfully tested by reconstructing rotations on the Bloch sphere and the completely decohering process (CDP) with high fidelities. We discuss limitations of our realization of QPT.

QST is used for the reconstruction of states that have been stored in and retrieved from the memory mode, yielding fidelities higher than 0.84. We assign the loss in fidelity to a higher impact of energy decay and observe additional dephasing, which may be caused either by the resonator mode inheriting the qubit non-linearity or by the bluesideband (BSB) drive. We then characterize the memory process with QPT, which gives us a process fidelity of 0.877. We repeat the experiment for 25 times and observe deviations regarding the dephasing process and obtain an average corrected fidelity of 0.886. The asymmetric dephasing behavior can be possibly explained by phase sensitive noise, either resulting from the high drive power of the BSB pulses or by the *IQ* control for the qubit pulses. We develop an empiric model in order to categorize the measurement results.

We vary the time t_s for which the respective state is stored in the memory mode and perform QPT for various t_s , enabling us to determine the dynamical behavior of the process matrix χ . We compare the outcomes with the ideal memory process and observe the expected exponential decay of the process fidelity. The memory process is simulated with a master equation approach. Deviations between simulation and experiment are explained by simplified assumptions in the theoretical model as well as by technical artifacts that cannot be reproduced by the simulation. We conclude that we demonstrate that the proposed architecture for a quantum memory works in principle, although we observe limitations that require further, more detailed investigations.

To test whether the asymmetries in dephasing are a result from phase sensitive noise contributions from the IQ channels, we can exchange the vector RF source for the qubit and check if the observed results are reproducible. If this is the case, the microwave electronics can be exchanged device by device and we can repeat the experiment, respectively. We furthermore need to find methods to increase the process fidelity, since we need fidelities > 0.9999 [37] for applicable QIP devices. This can be achieved by further decreasing external loss channels, e.g., by lowering the external coupling of the cavity or by optimizing the drive pulses with bandpass filters to avoid excitations of higher energy levels and state leakage [108]. Another possibility is the implementation of advanced pulse shapes, such as DRAG (derivative removal by adiabatic gate) [129–131].

From the theoretical point of view, we need to advance our master equation simulation, which is yet based on empirical assumptions. Ideally, we want to be able to simulate the whole protocol, which includes the reproduction of e.g. the BSB transition, starting from the general Rabi Hamiltonian [52, 132]. Furthermore, we need to include the effect of different pulse shapes in the simulation. Time-resolved tomography can be performed for a bigger variety of times t_s , which allows us to investigate the long time behavior of the process fidelity and with advanced techniques, enhancing stability [88, 96].

Another interesting option is the realization of alternative protocols for process characterization, such as ancilla-assisted QPT (AAQPT) [133]. In order to substantiate our QPT results, we can additionally implement randomized benchmarking for the system [37]. This may especially become interesting if we extend our system to multiple qubits. These systems can be realized for example by using higher electrical modes of the cavity with additional nodes/antinodes. The qubits can then be positioned in a way that each qubit can be addressed individually, and we can use different modes to store the state of the respective qubit. In another approach, we can build a system of multiple qubits and cavities arranged in a way that they take the form of a Bose-Hubbard chain [134] for analog quantum simulation.

Appendix A

QST and QPT

A.1 Density matrix for QST

We consider Eq. (2.10) and use the Born-rule [66] to interpret the evolution coefficients as expectation values

$$\text{Tr}(\rho\hat{\sigma}_x) = \langle\hat{\sigma}_x\rangle \quad (\text{A.1})$$

$$\text{Tr}(\rho\hat{\sigma}_y) = \langle\hat{\sigma}_y\rangle \quad (\text{A.2})$$

$$\text{Tr}(\rho\hat{\sigma}_z) = \langle\hat{\sigma}_z\rangle \quad (\text{A.3})$$

we assume that the projection to the quantization axis, which is a measurement of $\hat{\sigma}_z$ with the outcome $\langle\hat{\sigma}_z\rangle$, depends linearly on the respective RO phase φ_z . The reason for this is the small dispersive shift. Hence, we make the ansatz

$$\langle\hat{\sigma}_z\rangle(\varphi_z) = a\varphi_z + b \quad (\text{A.4})$$

and determine the coefficients a and b using the conditions

$$\langle\hat{\sigma}_z\rangle(\varphi_g) \stackrel{!}{=} 1 \quad (\text{A.5})$$

$$\langle\hat{\sigma}_z\rangle(\varphi_e) \stackrel{!}{=} -1 \quad (\text{A.6})$$

which yields

$$\langle\hat{\sigma}_z\rangle(\varphi_z) = \frac{2\varphi_z - \varphi_g - \varphi_e}{\varphi_g - \varphi_e}. \quad (\text{A.7})$$

We obtain similar results for $\langle\hat{\sigma}_x\rangle$ and for $\langle\hat{\sigma}_y\rangle$. Inserting the outcomes into Eq. (2.10) gives

$$\rho = \frac{1}{2} \left(I + \frac{2\varphi_z - \varphi_g - \varphi_e}{\varphi_g - \varphi_e} \hat{\sigma}_z + \frac{2\varphi_y - \varphi_g - \varphi_e}{\varphi_g - \varphi_e} \hat{\sigma}_y + \frac{2\varphi_x - \varphi_g - \varphi_e}{\varphi_g - \varphi_e} \hat{\sigma}_x \right), \quad (\text{A.8})$$

which directly yields Eq. (4.1).

A.2 Maximum likelihood estimation for QST

The probability $P(t_1, t_2, t_3, t_4)$ in Eq. 2.20 takes its maximal value if the exponent is minimized [81]. We write

$$P(t_1, t_2, t_3, t_4) = \mathcal{N} \prod_{i=x,y,z} \prod_{j=1}^N e^{-\frac{(\mu_i^{(j)} - \tilde{\mu}_i)^2}{2\sigma_i^2}} = \mathcal{N} e^{-\sum_{i=x,y,z} \sum_{j=1}^N \frac{(\mu_i^{(j)} - \tilde{\mu}_i)^2}{2\sigma_i^2}} \quad (\text{A.9})$$

We thus search for parameters t_i that minimize

$$\mathfrak{Q}(\{t_i\}) \equiv \sum_{i=x,y,z} \sum_{j=1}^N \frac{(\mu_i^{(j)} - \tilde{\mu}_i)^2}{2\sigma_i^2} \quad (\text{A.10})$$

And need to show that the resulting t_i also minimize Eq. (2.21). We calculate

$$\begin{aligned} \mathfrak{Q}(\{t_i\}) &\equiv \sum_{i=x,y,z} \sum_{j=1}^N \frac{(\mu_i^{(j)} - \tilde{\mu}_i)^2}{2\sigma_i^2} = \sum_{i=x,y,z} \frac{1}{2\sigma_i^2} \sum_{j=1}^N (\mu_i^{(j)})^2 - 2\mu_i^{(j)} \tilde{\mu}_i + \tilde{\mu}_i^2 \\ &= \sum_{i=x,y,z} \frac{1}{2\sigma_i^2} N(\bar{\mu}_i^2 - 2\bar{\mu}_i \tilde{\mu}_i + \tilde{\mu}_i^2) = \sum_{i=x,y,z} \frac{1}{2\sigma_i^2} N[\sigma_i^2 + (\mu_i - \tilde{\mu}_i)^2] \\ &= \frac{3}{2}N + N\mathcal{L}(\{t_i\}) \end{aligned}$$

where $\mathcal{L}(\{t_i\})$ is the likelihood-functional Eq. (2.21). We conclude that if the set $\{t_i\}$ minimizes \mathfrak{Q} , it simultaneously minimizes \mathcal{L} .

A.3 Basis change for QPT

We expand \mathcal{E} in the $\{B_m\}$ and in the $\{A_m\}$ basis.

$$\mathcal{E}(\rho) = \sum_{m,n} B_m \rho B_n^\dagger \chi_{mn} = \sum_{m,n} A_m \rho A_n^\dagger \chi'_{mn}. \quad (\text{A.11})$$

Since this holds for arbitrary states ρ , it follows that

$$\chi_{mn} B_m B_n^\dagger = \chi'_{mn} A_m A_n^\dagger \Leftrightarrow \chi'_{mn} \cdot I = \chi_{mn} M_m M_n^\dagger \quad (\text{A.12})$$

The result is obtained by either taking the trace:

$$\chi'_{mn} \cdot d = \chi_{mn} \text{Tr}(M_m M_n^\dagger) = \chi_{mn} \sum_{i=1}^d \lambda_{mn}^{(i)} \Leftrightarrow \chi'_{mn} = \bar{\lambda}_{mn} \chi_{mn} \quad (\text{A.13})$$

where $\bar{\lambda}_{mn}$ denotes the arithmetic mean of the eigenvalues, or by taking the determinant

$$(\chi'_{mn})^d = \chi_{mn}^d \det(M_m M_n^\dagger) = \chi_{mn}^d \prod_{i=1}^d \lambda_{mn}^{(i)} \Leftrightarrow \chi'_{mn} = \bar{\lambda}_{mn} \chi_{mn} \quad (\text{A.14})$$

where this time, $\bar{\lambda}_{mn}$ is the geometric mean. In the application, the result Eq. (A.13) is implemented due to simplicity.

A.4 Maximum likelihood estimation for QPT

We parametrize a physically valid process matrix $\tilde{\chi}(t)$ [88].

$$\tilde{\chi}(t) = T(t)^\dagger T(t) \quad (\text{A.15})$$

with a lower triangular matrix T that depends on d^4 parameters $t_i \in \mathbb{R}$ and $t = (t_1, \dots, t_{d^4})$. For the single qubit case, we set

$$T = \begin{pmatrix} t_1 & 0 & 0 & 0 \\ t_5 + it_6 & t_2 & 0 & 0 \\ t_{11} + it_{12} & t_7 + it_8 & t_3 & 0 \\ t_{15} + it_{16} & t_{13} + it_{14} & t_9 + it_{10} & t_4 \end{pmatrix} \quad (\text{A.16})$$

We minimize the distance Δ of χ and $\tilde{\chi}$ under the constraint that the trace is preserved [88]

$$\Delta(t) = \sum_{m,n} |\tilde{\chi}_{mn}(t) - \chi_{mn}|^2 + \lambda \left| \sum_{m,n} B_m^\dagger \tilde{\chi}_{mn}(t) B_n - I \right|^2. \quad (\text{A.17})$$

λ is introduced as a Lagrangian multiplier. For better practical implementation, a $(d \times d^3)$ block matrix \mathcal{B} that contains all basis matrices is defined

$$\mathcal{B} \equiv (B_1^\dagger \dots B_{d^2}^\dagger) \quad (\text{A.18})$$

therefore, the problem can be reformulated as

$$\Delta(t) = \|\tilde{\chi}(t) - \chi\|_F^2 + \lambda \|\mathcal{B} \cdot (\tilde{\chi}(t) \otimes I) \cdot \mathcal{B}^\dagger - I\|_F^2 \quad (\text{A.19})$$

where $\|\cdot\|_F$ denotes the Frobenius norm and \otimes is the Kronecker product. This optimization is performed using the `fminsearch()` [135] function in Matlab[®], but the trace-preserving condition is not fulfilled very well after convergence. As a result, trace-preserving is enforced before the minimization procedure. Again for practical reasons, this condition is written in the form

$$M^\dagger(t)M(t) = I \quad (\text{A.20})$$

with

$$M \equiv (T(t) \otimes I) \cdot \mathcal{B} \quad (\text{A.21})$$

The optimization problem is then solved by minimizing

$$\Delta(t) = \|T^\dagger(t)T(t) - \chi\|_F^2 \quad (\text{A.22})$$

under the constraint Eq. (A.20) using the `fmincon()` [136] function in Matlab[®]. It is an important issue that the optimization problem for $\Delta(t)$ is not convex in general, which means that many local minima may exist. The problem that the solving algorithm converges towards such a local minimum has to be avoided [88]. This can be achieved by assuming that the physical process matrix $\tilde{\chi}$ does not differ too much from the measured unphysical matrix χ . Let χ_0 denote the initial guess matrix for the minimization algorithm. Physicality of χ_0 enforces the matrix can be decomposed in the way described in A.15:

$$\chi_0 = T_0(t)^\dagger T_0(t) \quad (\text{A.23})$$

This can be achieved via Cholesky decomposition [137]. In order to realize this, χ_0 needs to be constructed as a positive definite matrix, which means that all eigenvalues have to be larger than 0. Let $\{q_i\}$ be the set of the eigenvalues of the experimentally determined χ . A diagonal matrix $D_0 = \text{diag}(p_1, \dots, p_{d^2})$ is constructed in the way [138]

$$p_i = \begin{cases} q_i & \text{if } q_i > 0 \\ \varepsilon & \text{else} \end{cases} \quad (\text{A.24})$$

where $\varepsilon > 0$ is a tolerance limit which is set to single type machine precision ($\simeq 10^{-7}$). We obtain an expression for χ_0 that is positive definite by construction and in some sense “close” to the measured χ -matrix

$$\chi_0 = U D_0 U^\dagger \quad (\text{A.25})$$

Appendix B

Distance measures

B.1 Diamond norm for the identity process

We write $\chi = (\chi)_{mn}$, $m, n \in \{0, 1, 2, 3\}$ and expand the reconstructed process \mathcal{E}_{exp} in the Pauli basis. We obtain

$$\begin{aligned}
\|\mathcal{E}_{\text{id}} - \mathcal{E}_{\text{exp}}\|_{\diamond} &= \sup_{\rho} (\|(\mathcal{E}_{\text{id}} \otimes I)(\rho) - (\mathcal{E}_{\text{exp}} \otimes I)(\rho)\|_1) \\
&= \sup_{\rho} \text{Tr} \sqrt{(\mathcal{E}_{\text{id}}(\rho_1) \otimes \rho_2 - \mathcal{E}_{\text{exp}}(\rho_1) \otimes \rho_2)^{\dagger} (\mathcal{E}_{\text{id}}(\rho_1) \otimes \rho_2 - \mathcal{E}_{\text{exp}}(\rho_1) \otimes \rho_2)} \\
&= \sup_{\rho} \text{Tr} \sqrt{\left[\left(\sum_{j,k=1}^3 \chi_{jk} \hat{\sigma}_j \rho_1 \hat{\sigma}_k^{\dagger} \right) \otimes \rho_2 \right]^{\dagger} \left[\left(\sum_{l,m=1}^3 \chi_{lm} \hat{\sigma}_l \rho_1 \hat{\sigma}_m^{\dagger} \right) \otimes \rho_2 \right]} \\
&= \sup_{\rho} \text{Tr} \sqrt{\sum_{j,k,l,m=1}^3 \chi_{jk}^* \hat{\sigma}_k \rho_1^{\dagger} \hat{\sigma}_j^{\dagger} \chi_{lm} \hat{\sigma}_l \rho_1 \hat{\sigma}_m^{\dagger} \otimes \rho_2^{\dagger} \rho_2} \\
&= \sup_{\rho} \text{Tr} \sqrt{\sum_{j,k,l,m=1}^3 \chi_{jk}^* \chi_{lm} \hat{\sigma}_k \rho_1^{\dagger} (\delta_{jl} I + i \sum_{n=1}^3 \epsilon_{jln} \hat{\sigma}_n) \rho_1 \hat{\sigma}_m^{\dagger} \otimes \rho_2^{\dagger} \rho_2} \\
&= \sup_{\rho} \text{Tr} \sqrt{\sum_{j,k,m=1}^3 \chi_{jk}^* \chi_{jm} \hat{\sigma}_k \hat{\sigma}_m \rho_1^{\dagger} \rho_1 \otimes \rho_2^{\dagger} \rho_2} \\
&= \sup_{\rho} \text{Tr} \sqrt{\sum_{j,k,m=1}^3 \chi_{jk}^* \chi_{jm} (\delta_{km} I + \sum_{n=1}^3 \epsilon_{kmn} \hat{\sigma}_n) \rho_1^{\dagger} \rho_1 \otimes \rho_2^{\dagger} \rho_2} \\
&= \sup_{\rho} \text{Tr} \sqrt{\sum_{j,k=1}^3 \chi_{kj} \chi_{jk} \rho_1^2 \otimes \rho_2^2} = \sqrt{\sum_{k=1}^3 (\chi^2)_{kk}} \cdot \sup_{\rho} \text{Tr} \sqrt{\rho^2} \\
&= \sqrt{\text{Tr}(\chi^2) - (\chi^2)_{00}} = \sqrt{\text{Tr}(P \cdot \chi^2)} = \sqrt{\text{Tr}(P \chi \chi^{\dagger} P^{\dagger})} = \|P \chi\|_F.
\end{aligned}$$

with $P \equiv \text{diag}(0, 1, 1, 1)$.

B.2 Quantum memory fidelity

We expect

$$\chi_{I,t} = \begin{pmatrix} 1 & 0 & 0 & 0 \\ 0 & 0 & 0 & 0 \\ 0 & 0 & 0 & 0 \\ 0 & 0 & 0 & 0 \end{pmatrix} \quad (\text{B.1})$$

and hence $f(\chi_I, \chi_{I,t}) = \sqrt{\chi_{11}}$, which means it is sufficient to calculate χ_{11} as a function of the raw measurement data (i.e. the resonator RO phase). We then use the following nomenclature introduced in Tab. B.1.

Input state	φ_x	φ_y	φ_z
$\mathcal{E}(g\rangle\langle g)$	φ_1	φ_2	φ_3
$\mathcal{E}(e\rangle\langle e)$	φ_4	φ_5	φ_6
$\mathcal{E}(+\rangle\langle +)$	φ_7	φ_8	φ_9
$\mathcal{E}(-\rangle\langle -)$	φ_{10}	φ_{11}	φ_{12}

Table B.1: Nomenclature for the RO phases for the respective input states

Equation (4.1) then yields

$$\mathcal{E}(|g\rangle\langle g|) = \frac{1}{\varphi_g - \varphi_e} \begin{pmatrix} \varphi_3 - \varphi_e & \bar{\varphi} - \varphi_1 - i(\bar{\varphi} - \varphi_2) \\ \bar{\varphi} - \varphi_1 + i(\bar{\varphi} - \varphi_2) & \varphi_g - \varphi_3 \end{pmatrix} \quad (\text{B.2})$$

. Analogous results are obtained for $\mathcal{E}(|1\rangle\langle 1|)$, $\mathcal{E}(|+\rangle\langle +|)$ and $\mathcal{E}(|-\rangle\langle -|)$. We calculate ρ'_1 , ρ'_2 , ρ'_3 and ρ'_4 using Eq. (2.41). We obtain

$$\begin{aligned} (\rho'_2)_{11} &= \frac{1}{\varphi_g - \varphi_e} \left\{ \varphi_9 - \frac{1}{2}(\varphi_3 + \varphi_6) + i[\varphi_{12} - \frac{1}{2}(\varphi_3 + \varphi_6)] \right\} \\ (\rho'_2)_{12} &= \frac{1}{\varphi_g - \varphi_e} \left\{ -\varphi_7 - \varphi_{11} + \frac{1}{2}(\varphi_1 + \varphi_4) + \frac{1}{2}(\varphi_2 + \varphi_5) + i[\varphi_8 - \varphi_{10} + \frac{1}{2}(\varphi_1 + \varphi_4) - \frac{1}{2}(\varphi_2 + \varphi_5)] \right\} \\ (\rho'_2)_{21} &= \frac{1}{\varphi_g - \varphi_e} \left\{ -\varphi_7 + \varphi_{11} + \frac{1}{2}(\varphi_1 + \varphi_4) - \frac{1}{2}(\varphi_2 + \varphi_5) + i[-\varphi_{10} - \varphi_8 + \frac{1}{2}(\varphi_1 + \varphi_4) + \frac{1}{2}(\varphi_2 + \varphi_5)] \right\} \\ (\rho'_2)_{22} &= \frac{1}{\varphi_g - \varphi_e} \left\{ -\varphi_9 + \frac{1}{2}(\varphi_3 + \varphi_6) - i[\varphi_{12} - \frac{1}{2}(\varphi_3 + \varphi_6)] \right\} \\ (\rho'_3)_{11} &= \frac{1}{\varphi_g - \varphi_e} \left\{ \varphi_9 - \frac{1}{2}(\varphi_3 + \varphi_6) + i[-\varphi_{12} + \frac{1}{2}(\varphi_3 + \varphi_6)] \right\} \\ (\rho'_3)_{12} &= \frac{1}{\varphi_g - \varphi_e} \left\{ -\varphi_7 + \varphi_{11} + \frac{1}{2}(\varphi_1 + \varphi_4) - \frac{1}{2}(\varphi_2 + \varphi_5) + i[\varphi_8 + \varphi_{10} - \frac{1}{2}(\varphi_1 + \varphi_4) - \frac{1}{2}(\varphi_2 + \varphi_5)] \right\} \\ (\rho'_3)_{21} &= \frac{1}{\varphi_g - \varphi_e} \left\{ -\varphi_7 - \varphi_{11} - \frac{1}{2}(\varphi_1 + \varphi_4) + \frac{1}{2}(\varphi_2 + \varphi_5) + i[\varphi_{10} - \varphi_8 - \frac{1}{2}(\varphi_1 + \varphi_4) + \frac{1}{2}(\varphi_2 + \varphi_5)] \right\} \\ (\rho'_3)_{22} &= \frac{1}{\varphi_g - \varphi_e} \left\{ -\varphi_9 + \frac{1}{2}(\varphi_3 + \varphi_6) + i[\varphi_{12} - \frac{1}{2}(\varphi_3 + \varphi_6)] \right\} \end{aligned}$$

We use Eq. (2.46) which gives

$$\chi = \frac{1}{4} \begin{pmatrix} \rho'_1 + \hat{\sigma}_x \rho'_3 + \rho'_2 \hat{\sigma}_x + \hat{\sigma}_x \rho'_4 \hat{\sigma}_x & \rho'_1 \hat{\sigma}_x + \hat{\sigma}_x \rho'_3 \hat{\sigma}_x - \rho'_2 - \hat{\sigma}_x \rho'_4 \\ \hat{\sigma}_x \rho'_1 - \rho'_3 + \hat{\sigma}_x \rho'_2 \hat{\sigma}_x - \rho'_4 \hat{\sigma}_x & \hat{\sigma}_x \rho'_1 \hat{\sigma}_x - \rho'_3 \hat{\sigma}_x - \hat{\sigma}_x \rho'_2 + \rho'_4 \end{pmatrix} \quad (\text{B.3})$$

it is sufficient to calculate

$$\chi_{11} = \frac{1}{4} (\rho'_1 + \hat{\sigma}_x \rho'_3 + \rho'_2 \hat{\sigma}_x + \hat{\sigma}_x \rho'_4 \hat{\sigma}_x)_{11}. \quad (\text{B.4})$$

A lengthy, but straightforward calculation gives

$$\begin{aligned} \chi_{11} &= \frac{1}{4(\varphi_g - \varphi_e)} (\varphi_3 - \varphi_e - \varphi_2 + \varphi_{11} + \frac{1}{2}(\varphi_1 + \varphi_4) - \frac{1}{2}(\varphi_2 + \varphi_5) + i[-\varphi_8 - \varphi_{10} + \frac{1}{2}(\varphi_1 + \varphi_4) \\ &\quad + \frac{1}{2}(\varphi_2 + \varphi_5)] - \varphi_7 + \varphi_{11} + \frac{1}{2}(\varphi_1 + \varphi_4) - \frac{1}{2}(\varphi_2 + \varphi_5) \\ &\quad + i(\varphi_8 + \varphi_{10} - \frac{1}{2}(\varphi_1 + \varphi_4) - \frac{1}{2}(\varphi_2 + \varphi_5) + \varphi_g - \varphi_6) \\ &= \frac{1}{4} [1 + \frac{1}{(\varphi_g - \varphi_e)} (\varphi_1 - \varphi_2 + \varphi_3 + \varphi_4 - \varphi_5 - \varphi_6 - 2\varphi_7 + 2\varphi_{11})] \end{aligned}$$

we conclude that $f(\{x_i\}, \varphi_e) = \sqrt{\chi_{11}}$ is equivalent to Eq. (4.23).

We define $\boldsymbol{\varphi} \equiv (\varphi_1, \varphi_2, \varphi_3, \varphi_4, \varphi_5, \varphi_6, \varphi_7, \varphi_8, \varphi_9, \varphi_{10}, \varphi_{11}, \varphi_{12})^T$ and $\Delta\varphi_i$ as the uncertainty of φ_i . Propagation of error [121] then yields

$$\Delta f = \sqrt{\sum_{i=1}^{12} \left(\frac{\partial f(\boldsymbol{\varphi}, \varphi_e)}{\partial \varphi_i} \cdot \Delta\varphi_i \right)^2 + \left(\frac{\partial f(\boldsymbol{\varphi}, \varphi_e)}{\partial \varphi_e} \Delta\varphi_e \right)^2} \quad (\text{B.5})$$

$$\frac{\partial f(\boldsymbol{\varphi}, \varphi_e)}{\partial \varphi_e} = \frac{1}{4} \frac{1}{\sqrt{1 + \frac{\mathbf{a} \cdot \boldsymbol{\varphi}}{\varphi_g - \varphi_e}}} \frac{\mathbf{a} \cdot \boldsymbol{\varphi}}{(\varphi_g - \varphi_e)^2} \quad (\text{B.6})$$

$$\frac{\partial f(\boldsymbol{\varphi}, \varphi_e)}{\partial x_i} = \frac{1}{4} \frac{1}{\sqrt{1 + \frac{\mathbf{a} \cdot \boldsymbol{\varphi}}{\varphi_g - \varphi_e}}} \frac{a_i}{(\varphi_g - \varphi_e)} \quad (\text{B.7})$$

We obtain the result Eq. (4.24) by inserting Eq. (B.6) and Eq. (B.7) into Eq. (B.5).

Appendix C

RO phase fluctuations

C.1 Thermal photons in the cavity

We calculate the number of thermal photons N_{th} in the cavity [123]

$$N_{\text{th}} = \int_{\text{cavity}} dV \int_0^\infty d\omega n(\omega, T) \cdot D(\omega) \quad (\text{C.1})$$

with the Bose-Einstein distribution $n(\omega, T)$ and the density of states $D(\omega)$. For photons, we have [123]

$$n(\omega, T) = \frac{1}{e^{\frac{\hbar\omega}{k_{\text{B}}T}} - 1} \quad (\text{C.2})$$

$$D(\omega) = \frac{\omega^2}{c^3\pi^2}. \quad (\text{C.3})$$

Thus

$$N_{\text{th}} = V \int_0^\infty d\omega \frac{1}{e^{\frac{\hbar\omega}{k_{\text{B}}T}} - 1} \frac{\omega^2}{c^3\pi^2} \quad (\text{C.4})$$

We substitute $x = \hbar\omega/k_{\text{B}}T$ and obtain [115]

$$N_{\text{th}} = V \left(\frac{k_{\text{B}}T}{\hbar} \right)^2 \frac{1}{\pi^2 c^3} \frac{kT}{\hbar} \underbrace{\int_0^\infty dx \frac{x^2}{e^x - 1}}_{=\Gamma(3)\zeta(3)} = V \left(\frac{k_{\text{B}}T}{\hbar c} \right)^3 \frac{2\zeta(3)}{\pi^2}. \quad (\text{C.5})$$

For the difference in thermal photons, we obtain

$$\Delta N_{\text{th}} = N_{\text{th}}(t + \Delta T) - N_{\text{th}}(T) = \frac{6\zeta(3)V}{\pi^2} \left(\frac{k}{\hbar c} \right)^3 T^2 \Delta(T) + \mathcal{O}(\Delta T^2). \quad (\text{C.6})$$

This yields a shift

$$\Delta\omega = 2\chi\Delta N_{\text{th}} \quad (\text{C.7})$$

and a readout phase

$$\varphi = \arctan \frac{2(\omega - \omega_m)}{\kappa} = \frac{2}{\kappa}(\omega - \omega_m) + \mathcal{O}((\omega - \omega_m)^3). \quad (\text{C.8})$$

In the linear regime, the shift in the readout phase φ_g and φ_e is induced by a frequency shift of 2χ

$$\varphi_g - \varphi_e = \frac{2}{\kappa} \cdot 2\chi \quad (\text{C.9})$$

Thus

$$\frac{\Delta\varphi}{\varphi_g - \varphi_e} = \Delta N_{\text{th}}. \quad (\text{C.10})$$

C.2 Thermal expansion of the cavity

We calculate the frequency for the TE_{mnl} mode, where we use $f = \omega/2\pi$

$$f_{mnl} = \frac{c}{2\pi\sqrt{\varepsilon_r\mu_r}} \sqrt{\left(\frac{m\pi}{a'}\right)^2 + \left(\frac{n\pi}{b}\right)^2 + \left(\frac{l\pi}{d}\right)^2} \quad (\text{C.11})$$

where d is the height of the cavity, b the width and a' is an effective length which takes the curvature of the cavity ends into account [108, 109]

$$a' = a - b + \frac{\pi}{4}b \quad (\text{C.12})$$

where a is the length of the rectangular part of the cavity without the semicircles. For readout, TE_{101} is used and we obtain the resonance frequency

$$f_p = f_{101} = \frac{c}{2\sqrt{\varepsilon_r\mu_r}} \sqrt{\left(\frac{1}{a'}\right)^2 + \left(\frac{1}{d}\right)^2} \quad (\text{C.13})$$

a change in the effective length and the height translates into

$$\Delta f_p = \frac{\partial f_p}{\partial a'} \Delta a' + \frac{\partial f_p}{\partial d} \Delta d \quad (\text{C.14})$$

Where higher order terms are neglected. This calculation gives

$$\Delta f_p = -\frac{f_p}{a'^2 + d^2} \left(\frac{d^2 \Delta a'}{a'} + \frac{a'^2 \Delta d}{d} \right) \quad (\text{C.15})$$

Again, we assume that we are in the linear regime for the readout phase

$$\varphi_g - \varphi_e = \frac{2}{\kappa} \cdot 2\chi \quad (\text{C.16})$$

We also assume linear dependence of thermal expansion [124]

$$\Delta a' = \alpha a' \Delta T \quad (\text{C.17})$$

$$\Delta d = \alpha d \Delta T \quad (\text{C.18})$$

With the expansion coefficient α . We then obtain

$$\frac{\Delta\varphi}{\varphi_g - \varphi_e} = \frac{f_p}{\chi/2\pi} \alpha \Delta T \quad (\text{C.19})$$

Since the expansion coefficient usually decreases with decreasing temperature [49], we obtain an upper bound if we take α at room temperature.

C.3 Thermal radiation by the antennas

Consider that the antenna absorbs the energy E . This leads to emission of photons into the cavity, which yields an AC Stark shift and a shift in the readout phase. In a simplified assumption, we obtain N photons with an average wavelength $\bar{\lambda}$

$$E = N \cdot \frac{hc}{\bar{\lambda}} \quad (\text{C.20})$$

The average wavelength can be calculated from the Planck curve [139] and obeys a Wien-like displacement law [126, 127]

$$\bar{\lambda} = \frac{b}{T}. \quad (\text{C.21})$$

The antennas heat up by ΔT , which can be calculated by $E = c_a m \Delta T$ where c_a [124] is the specific heat. If d is the antenna diameter, l the length and ρ the density, we have $m = \rho \pi d^2 l / 4$. c_a can be calculated by $c_{\text{mol}} = \gamma T + \alpha T^3$ [49] and we neglect the phononic contribution because we operate at mK temperatures. The specific heat per volume is then given by $c_a = \rho \gamma T / M_{\text{mol}}$ with the mol mass M_{mol} . We obtain a relation

$$\frac{\Delta\varphi}{\varphi_g - \varphi_e} = \Delta N = \Delta E \frac{\bar{\lambda}}{hc} = \underbrace{\frac{\rho^2 \gamma d^2 \pi l b}{4 M_{\text{mol}} hc}}_{\equiv \beta} \cdot \Delta T \quad (\text{C.22})$$

Appendix D

Master equation

We start with the Lindblad equation

$$\frac{d\rho}{dt} = -\frac{i}{\hbar}[\hat{H}, \rho] + \gamma_1(2\hat{\sigma}^- \rho \hat{\sigma}^+ - \hat{\sigma}^+ \hat{\sigma}^- \rho - \rho \hat{\sigma}^+ \hat{\sigma}^-) + \gamma_\varphi(2\hat{\sigma}_z \rho \hat{\sigma}_z - \underbrace{\hat{\sigma}_z \hat{\sigma}_z}_{=I} \rho - \rho \underbrace{\hat{\sigma}_z \hat{\sigma}_z}_{=I}). \quad (\text{D.1})$$

We analyze the unitary part for the driven qubit. We start with the Hamiltonian in Eq. 2.16

$$\hat{H}_d = \frac{\hbar}{2} \begin{pmatrix} \delta & \Omega_d \cos \varphi_d - i\Omega_d \sin \varphi_d \\ \Omega_d \cos \varphi_d + i\Omega_d \sin \varphi_d & -\delta \end{pmatrix}. \quad (\text{D.2})$$

We parametrize ρ as

$$\rho = \begin{pmatrix} \rho_{11} & \rho_{12} \\ \rho_{21} & \rho_{22} \end{pmatrix} \quad (\text{D.3})$$

and calculate the commutator $[\hat{H}_d, \rho]$ and finally obtain

$$\begin{aligned} [\hat{H}_d, \rho]_{11} &= \frac{\hbar}{2}(\rho_{12}(-\Omega_d \cos \varphi_d - i\Omega_d \sin \varphi_d) + \rho_{21}(\Omega_d \cos \varphi_d - i\Omega_d \sin \varphi_d)) \\ [\hat{H}_d, \rho]_{12} &= \frac{\hbar}{2}(\rho_{11}(-\Omega_d \cos \varphi_d + i\Omega_d \sin \varphi_d) + \rho_{22}(\Omega_d \cos \varphi_d - i\Omega_d \sin \varphi_d) + 2\delta\rho_{12}) \\ [\hat{H}_d, \rho]_{21} &= \frac{\hbar}{2}(\rho_{11}(\Omega_d \cos \varphi_d + i\Omega_d \sin \varphi_d) + \rho_{22}(-\Omega_d \cos \varphi_d - i\Omega_d \sin \varphi_d) - 2\delta\rho_{12}) \\ [\hat{H}_d, \rho]_{22} &= \frac{\hbar}{2}(\rho_{12}(\Omega_d \cos \varphi_d + i\Omega_d \sin \varphi_d) + \rho_{21}(-\Omega_d \cos \varphi_d + i\Omega_d \sin \varphi_d)). \end{aligned}$$

We define $\boldsymbol{\rho} = (\rho_{11}, \rho_{12}, \rho_{21}, \rho_{22})^T$ and rewrite the commutator as a system of linear equations $\hat{\mathcal{H}} \cdot \boldsymbol{\rho}$, which directly yields Eq. 2.62. We perform a similar calculation for the energy relaxation term

$$\begin{aligned} &2\gamma_1 \begin{pmatrix} 0 & 1 \\ 0 & 0 \end{pmatrix} \begin{pmatrix} \rho_{11} & \rho_{12} \\ \rho_{21} & \rho_{22} \end{pmatrix} \begin{pmatrix} 0 & 0 \\ 1 & 0 \end{pmatrix} - \gamma_1 \begin{pmatrix} 0 & 0 \\ 1 & 0 \end{pmatrix} \begin{pmatrix} 0 & 1 \\ 0 & 0 \end{pmatrix} \begin{pmatrix} \rho_{11} & \rho_{12} \\ \rho_{21} & \rho_{22} \end{pmatrix} - \gamma_1 \begin{pmatrix} \rho_{11} & \rho_{12} \\ \rho_{21} & \rho_{22} \end{pmatrix} \begin{pmatrix} 0 & 0 \\ 1 & 0 \end{pmatrix} \begin{pmatrix} 0 & 1 \\ 0 & 0 \end{pmatrix} \\ &= \begin{pmatrix} 2\rho_{22} & -\rho_{12} \\ -\rho_{21} & -2\rho_{22} \end{pmatrix} \end{aligned}$$

We again rewrite this as a system of linear equations

$$\hat{\mathcal{L}}_1 \cdot \boldsymbol{\rho} = \gamma_1 \begin{pmatrix} 0 & 0 & 0 & 2 \\ 0 & -1 & 0 & 0 \\ 0 & 0 & -1 & 0 \\ 0 & 0 & 0 & -2 \end{pmatrix} \cdot \begin{pmatrix} \rho_{11} \\ \rho_{12} \\ \rho_{21} \\ \rho_{22} \end{pmatrix}. \quad (\text{D.4})$$

We perform the same procedure for the dephasing term

$$2\gamma_\varphi \begin{pmatrix} 1 & 0 \\ 0 & -1 \end{pmatrix} \begin{pmatrix} \rho_{11} & \rho_{12} \\ \rho_{21} & \rho_{22} \end{pmatrix} \begin{pmatrix} 1 & 0 \\ 0 & -1 \end{pmatrix} - 2\gamma_\varphi \begin{pmatrix} \rho_{11} & \rho_{12} \\ \rho_{21} & \rho_{22} \end{pmatrix} = -4\gamma_\varphi \begin{pmatrix} 0 & \rho_{12} \\ \rho_{21} & 0 \end{pmatrix}$$

which yields

$$\hat{\mathcal{L}}_\varphi \cdot \boldsymbol{\rho} = \gamma_\varphi \begin{pmatrix} 0 & 0 & 0 & 0 \\ 0 & -4 & 0 & 0 \\ 0 & 0 & -4 & 0 \\ 0 & 0 & 0 & 0 \end{pmatrix} \cdot \begin{pmatrix} \rho_{11} \\ \rho_{12} \\ \rho_{21} \\ \rho_{22} \end{pmatrix}. \quad (\text{D.5})$$

We set $\hat{\mathcal{L}} = \hat{\mathcal{L}}_1 + \hat{\mathcal{L}}_\varphi$, which leads to Eq. 2.63. Energy decay and dephasing of the free qubit and the memory mode are modelled with $\hat{\mathcal{L}}$ and $\hat{\mathcal{H}} = \mathbf{0}$. For the memory mode, the population is reverted before solving the equation and finally reverted again, since the decaying Fock state $|1\rangle$ corresponds to the $|g\rangle$ state and not to $|e\rangle$. The excitation and deexcitation of the BSB is modelled using Eq. (4.30). The systems of ordinary differential equations are then solved in Matlab[®] using the `ode45`-function [140], which is based on the Runge-Kutta (4,5)-formula [141]. We recognize that the solver only works for real valued systems. Hence, we map the complex (4×4) -systems to auxiliary real valued (8×8) -systems, solve the equations, and revert the mapping. Consider an arbitrary linear system of equations with a squared matrix A , i.e. $\dot{\mathbf{x}} = A \cdot \mathbf{x}$. We decompose $\mathbf{x} = \mathbf{r} + i\mathbf{j}$ and $A = R + iJ$. Reordering the terms gives

$$\begin{pmatrix} \dot{\mathbf{r}} \\ \dot{\mathbf{j}} \end{pmatrix} = \begin{pmatrix} R & -J \\ J & R \end{pmatrix} \cdot \begin{pmatrix} \mathbf{r} \\ \mathbf{j} \end{pmatrix} \quad (\text{D.6})$$

We reshape $\boldsymbol{\rho}$ into a column vector with eight real entries. The system matrix can then be written as

$$\begin{pmatrix} 0 & -\Omega_d \sin \varphi_d & -\Omega_d \sin \varphi_d & -2\gamma_1 & 0 & -\Omega_d \cos \varphi_d & \Omega_d \cos \varphi_d & 0 \\ \Omega_d \sin \varphi_d & -\gamma_1 - 4\gamma_\varphi & 0 & -\Omega_d \sin \varphi_d & -\Omega_d \cos \varphi_d & 2\delta & 0 & \Omega_d \cos \varphi_d \\ \Omega_d \sin \varphi_d & 0 & -\gamma_1 - 4\gamma_\varphi & -\Omega_d \sin \varphi_d & \Omega_d \cos \varphi_d & 0 & -2\delta & -\Omega_d \cos \varphi_d \\ 0 & \Omega_d \sin \varphi_d & \Omega_d \sin \varphi_d & -2\gamma_1 & 0 & \Omega_d \cos \varphi_d & -\Omega_d \cos \varphi_d & 0 \\ 0 & \Omega_d \cos \varphi_d & -\Omega_d \cos \varphi_d & 0 & 0 & -\Omega_d \sin \varphi_d & -\Omega_d \sin \varphi_d & 2\gamma_1 \\ \Omega_d \cos \varphi_d & -2\delta & 0 & -\Omega_d \cos \varphi_d & \Omega_d \sin \varphi_d & -\gamma_1 - 4\gamma_\varphi & 0 & -\Omega_d \sin \varphi_d \\ -\Omega_d \cos \varphi_d & 0 & 2\delta & \Omega_d \cos \varphi_d & \Omega_d \sin \varphi_d & 0 & -\gamma_1 - 4\gamma_\varphi & -\Omega_d \sin \varphi_d \\ 0 & -\Omega_d \cos \varphi_d & \Omega_d \cos \varphi_d & 0 & 0 & \Omega_d \sin \varphi_d & \Omega_d \sin \varphi_d & -2\gamma_1 \end{pmatrix}$$

which can be solved with `ode45`

Bibliography

- [1] F. Simões, M. Almeida, M. Pinheiro, R. D. Anjos, A. D. Santos, R. Roberto, V. Teichrieb, C. Suetsugo, and A. Pelinson, in *2012 14th Symposium on Virtual and Augmented Reality* (2012), pp. 74–83.
- [2] M. K. Agoston, *Computer Graphics and Geometric Modelling: Implementation & Algorithms* (Springer-Verlag, Berlin, Heidelberg, 2004), ISBN 1852338180.
- [3] A. P. Witkin”, “Recovering surface shape and orientation from texture”, *Artificial Intelligence* **17**, 17 (1981).
- [4] R. Dörner, *Virtual und Augmented Reality (VR/AR) - Grundlagen und Methoden der Virtuellen und Augmentierten Realität* (2014), ISBN 978-3-642-28902-6.
- [5] D. Samak, A. Fischer, and D. Rittel, “3D Reconstruction and Visualization of Microstructure Surfaces from 2D Images”, *CIRP Annals* **56**, 149 (2007).
- [6] D. Raneri, “Enhancing forensic investigation through the use of modern three-dimensional (3D) imaging technologies for crime scene reconstruction”, *Australian Journal of Forensic Sciences* **50**, 697 (2018).
- [7] R. Smith-Bindman, D. L. Miglioretti, E. Johnson, C. Lee, H. S. Feigelson, M. Flynn, R. T. Greenlee, R. L. Kruger, M. C. Hornbrook, D. Roblin, L. I. Solberg, N. Vanneman, S. Weinmann, and A. E. Williams, “Use of Diagnostic Imaging Studies and Associated Radiation Exposure For Patients Enrolled in Large Integrated Healthcare Systems, 1996-2010”, *JAMA* **307**, 10.1001/jama.2012.5960 (2012).
- [8] J. V. Frangioni, “New Technologies for Human Cancer Imaging”, *J Clin Oncol* **26**, 4012 (2008).
- [9] T. Buzug, *Einführung in die Computertomographie. Mathematisch-physikalische Grundlagen der Bildrekonstruktion* (2008).
- [10] V. Vedral, *Introduction to Quantum Information Science (Oxford Graduate Texts)* (Oxford University Press, Inc., New York, NY, USA, 2006), ISBN 0199215707.

- [11] D. Griffiths, *Introduction to Quantum Mechanics*, Pearson international edition (Pearson Prentice Hall, 2005), ISBN 9780131118928, URL <https://books.google.de/books?id=z4fwAAAAAAAJ>.
- [12] M. A. Nielsen and I. L. Chuang, *Quantum Computation and Quantum Information: 10th Anniversary Edition* (Cambridge University Press, New York, NY, USA, 2011), 10th ed., ISBN 1107002176, 9781107002173.
- [13] J. B. Altepeter, D. F. V. James, and P. G. Kwiat, in *Quantum State Estimation*, edited by M. G. A. Paris and J. Řeháček (2004), vol. 649 of *Lecture Notes in Physics, Berlin Springer Verlag*, pp. 113–145.
- [14] I. L. Chuang and M. A. Nielsen, “Prescription for experimental determination of the dynamics of a quantum black box”, *Journal of Modern Optics* **44**, 2455 (1997).
- [15] T. Hogg, D. Fattal, K.-Y. Chen, and S. Guha, *Economic Applications of Quantum Information Processing*, vol. 8 of *New Economic Windows* (2010).
- [16] P. W. Shor, “Polynomial-Time Algorithms for Prime Factorization and Discrete Logarithms on a Quantum Computer”, *SIAM J. Comput.* **26**, 1484 (1997).
- [17] A. Montanaro, “Quantum algorithms: an overview”, *Npj Quantum Information* **2**, 15023 EP (2016).
- [18] J. Preskill, “Quantum Computing in the NISQ era and beyond”, *Quantum* **2**, 79 (2018).
- [19] A. A. Houck, J. Koch, M. H. Devoret, S. M. Girvin, and R. J. Schoelkopf, “Life after charge noise: recent results with transmon qubits”, *Quantum Information Processing* **8**, 105 (2009).
- [20] R. Barends, J. Kelly, A. Megrant, D. Sank, E. Jeffrey, Y. Chen, Y. Yin, B. Chiaro, J. Mutus, C. Neill, P. O’Malley, P. Roushan, J. Wenner, T. C. White, A. N. Cleland, and J. M. Martinis, “Coherent Josephson Qubit Suitable for Scalable Quantum Integrated Circuits”, *Phys. Rev. Lett.* **111**, 080502 (2013).
- [21] Z.-L. Xiang, S. Ashhab, J. Q. You, and F. Nori, “Hybrid quantum circuits: Superconducting circuits interacting with other quantum systems”, *Reviews of Modern Physics* **85**, 623 (2013).
- [22] H. Walther, B. T. H. Varcoe, B.-G. Englert, and T. Becker, “Cavity quantum electrodynamics”, *Reports on Progress in Physics* **69**, 1325 (2006).
- [23] A. Imamoglu, D. D. Awschalom, G. Burkard, D. P. DiVincenzo, D. Loss, M. Sherwin, and A. Small, “Quantum Information Processing Using Quantum Dot Spins and Cavity QED”, *Phys. Rev. Lett.* **83**, 4204 (1999).
- [24] A. Blais, R.-S. Huang, A. Wallraff, S. M. Girvin, and R. J. Schoelkopf, “Cavity quantum electrodynamics for superconducting electrical circuits: An architecture for quantum computation”, *Phys. Rev. A* **69**, 062320 (2004).

- [25] P. Roushan, C. Neill, Y. Chen, M. Kolodrubetz, C. Quintana, N. Leung, M. Fang, R. Barends, B. Campbell, Z. Chen, B. Chiaro, A. Dunsworth, E. Jeffrey, J. Kelly, A. Megrant, J. Mutus, P. J. J. O’Malley, D. Sank, A. Vainsencher, J. Wenner, T. White, A. Polkovnikov, A. N. Cleland, and J. M. Martinis, “Observation of topological transitions in interacting quantum circuits”, *Nature* **515**, 241 EP (2014).
- [26] A. Potocnik, A. Bargerbos, F. A. Y. N. Schröder, S. A. Khan, M. C. Collodo, S. Gasparinetti, Y. Salathé, C. Creatore, C. Eichler, H. E. Türeci, A. W. Chin, and A. Wallraff, “Studying light-harvesting models with superconducting circuits”, *Nature Communications* **9**, 904 (2018).
- [27] H. Paik, D. I. Schuster, L. S. Bishop, G. Kirchmair, G. Catelani, A. P. Sears, B. R. Johnson, M. J. Reagor, L. Frunzio, L. I. Glazman, S. M. Girvin, M. H. Devoret, and R. J. Schoelkopf, “Observation of High Coherence in Josephson Junction Qubits Measured in a Three-Dimensional Circuit QED Architecture”, *Phys. Rev. Lett.* **107**, 240501 (2011).
- [28] M. Reagor, W. Pfaff, C. Axline, R. W. Heeres, N. Ofek, K. Sliwa, E. Holland, C. Wang, J. Blumoff, K. Chou, M. J. Hatridge, L. Frunzio, M. H. Devoret, L. Jiang, and R. J. Schoelkopf, “Quantum memory with millisecond coherence in circuit QED”, *Phys. Rev. B* **94**, 014506 (2016).
- [29] C. Rigetti, J. M. Gambetta, S. Poletto, B. L. T. Plourde, J. M. Chow, A. D. Córcoles, J. A. Smolin, S. T. Merkel, J. R. Rozen, G. A. Keefe, M. B. Rothwell, M. B. Ketchen, and M. Steffen, “Superconducting qubit in a waveguide cavity with a coherence time approaching 0.1 ms”, *Phys. Rev. B* **86**, 100506 (2012).
- [30] C. J. Axline, L. D. Burkhardt, W. Pfaff, M. Zhang, K. Chou, P. Campagne-Ibarcq, P. Reinhold, L. Frunzio, S. M. Girvin, L. Jiang, M. H. Devoret, and R. J. Schoelkopf, “On-demand quantum state transfer and entanglement between remote microwave cavity memories”, *Nature Physics* **14**, 705 (2018).
- [31] S. Hacoen-Gourgy, L. P. García-Pintos, L. S. Martin, J. Dressel, and I. Siddiqi, “Incoherent Qubit Control Using the Quantum Zeno Effect”, *Phys. Rev. Lett.* **120**, 020505 (2018).
- [32] A. Narla, K. M. Sliwa, M. Hatridge, S. Shankar, L. Frunzio, R. J. Schoelkopf, and M. H. Devoret, “Wireless Josephson amplifier”, *Applied Physics Letters* **104**, 232605 (2014).
- [33] B. Vlastakis, G. Kirchmair, Z. Leghtas, S. Nigg, L. Frunzio, S. Girvin, M. Mirrahimi, M. H. Devoret, and R. J. Schoelkopf, *Deterministically Encoding Quantum Information Using 100-Photon Schrodinger Cat States*, vol. 342 of *Science (New York, N.Y.)* (2013).
- [34] D. P. DiVincenzo, “The Physical Implementation of Quantum Computation”, *Fortschritte der Physik* **48**, 771 (2000).
- [35] E. Xie, F. Deppe, M. Renger, D. Repp, P. Eder, M. Fischer, J. Goetz, S. Pogorzalek, K. G. Fedorov, A. Marx, and R. Gross, “Compact 3D quantum memory”, *Applied Physics Letters* **112**, 202601 (2018).

- [36] P. J. Leek, M. Baur, J. M. Fink, R. Bianchetti, L. Steffen, S. Filipp, and A. Wallraff, “Cavity Quantum Electrodynamics with Separate Photon Storage and Qubit Readout Modes”, *Phys. Rev. Lett.* **104**, 100504 (2010).
- [37] E. Knill, D. Leibfried, R. Reichle, J. Britton, R. B. Blakestad, J. D. Jost, C. Langer, R. Ozeri, S. Seidelin, and D. J. Wineland, “Randomized benchmarking of quantum gates”, *Phys. Rev. A* **77**, 012307 (2008).
- [38] J. M. Chow, J. M. Gambetta, L. Tornberg, J. Koch, L. S. Bishop, A. A. Houck, B. R. Johnson, L. Frunzio, S. M. Girvin, and R. J. Schoelkopf, “Randomized Benchmarking and Process Tomography for Gate Errors in a Solid-State Qubit”, *Phys. Rev. Lett.* **102**, 090502 (2009).
- [39] D. P. DiVincenzo, “The Physical Implementation of Quantum Computation”, *Fortschritte der Physik* **48** (2000).
- [40] C. E. Shannon, “A Mathematical Theory of Communication”, *Bell System Technical Journal* **27** (1994).
- [41] R. Blatt and D. Wineland, “Entangled states of trapped atomic ions”, *Nature* **453**, 1008 EP (2008).
- [42] R. Blatt and C. F. Roos, “Quantum simulations with trapped ions”, *Nature Physics* **8**, 277 EP (2012).
- [43] X. Zhu, S. Saito, A. Kemp, K. Kakuyanagi, S.-i. Karimoto, H. Nakano, W. J. Munro, Y. Tokura, M. S. Everitt, K. Nemoto, M. Kasu, N. Mizuochi, and K. Semba, “Coherent coupling of a superconducting flux qubit to an electron spin ensemble in diamond”, *Nature* **478**, 221 EP (2011).
- [44] F. Jelezko and J. Wrachtrup, “Single defect centres in diamond: A review”, *physica status solidi (a)* **203**, 3207 (2006).
- [45] P. Vernaz-Gris, K. Huang, M. Cao, A. S. Sheremet, and J. Laurat, “Highly-efficient quantum memory for polarization qubits in a spatially-multiplexed cold atomic ensemble”, *Nature Communications* **9**, 363 (2018).
- [46] A. C. Johnson, J. R. Petta, J. M. Taylor, A. Yacoby, M. D. Lukin, C. M. Marcus, M. P. Hanson, and A. C. Gossard, “Triplet-singlet spin relaxation via nuclei in a double quantum dot”, *Nature* **435**, 925 EP (2005).
- [47] A. Blais, J. Gambetta, A. Wallraff, D. I. Schuster, S. M. Girvin, M. H. Devoret, and R. J. Schoelkopf, “Quantum-information processing with circuit quantum electrodynamics”, *Phys. Rev. A* **75**, 032329 (2007).
- [48] G. Wendin, “Quantum information processing with superconducting circuits: a review”, *Reports on Progress in Physics* **80**, 106001 (2017).
- [49] R. Gross and A. Marx, “Festkörperphysik”, *Physik in unserer Zeit* **44**, 204 (2012).

- [50] Y. Bruynseraede, C. Vlekken, C. Van Haesendonck, and V. V. Moshchalkov, *The New Superconducting Electronics* (Springer Netherlands, Dordrecht, 1993), chap. Fundamentals of Giaever and Josephson Tunneling, pp. 1–28, ISBN 978-94-011-1918-4, URL https://doi.org/10.1007/978-94-011-1918-4_1.
- [51] B. Josephson, “Possible new effects in superconductive tunnelling”, *Physics Letters* **1**, 251 (1962).
- [52] R. Gross and A. Marx, “Applied Superconductivity: Josephson Effect and Superconducting Electronics”, WMI (2011).
- [53] J. Koch, T. M. Yu, J. Gambetta, A. A. Houck, D. I. Schuster, J. Majer, A. Blais, M. H. Devoret, S. M. Girvin, and R. J. Schoelkopf, “Charge-insensitive qubit design derived from the Cooper pair box”, *Phys. Rev. A* **76**, 042319 (2007).
- [54] Y. Nakamura, Y. A. Pashkin, and J. S. Tsai, “Coherent control of macroscopic quantum states in a single-Cooper-pair box”, *Nature* **398**, 786 EP (1999).
- [55] V. Bouchiat, D. Vion, P. Joyez, D. Esteve, and M. H. Devoret, “Quantum coherence with a single Cooper pair”, *Physica Scripta* **1998**, 165 (1998).
- [56] J. Kelly, “A Preview of Bristlecone, Google’s New Quantum Processor”, (2018), URL <https://ai.googleblog.com/2018/03/a-preview-of-bristlecone-googles-new.html>.
- [57] M. H. devoret and J. M. Martinis, “Implementing Qubits with Superconducting Integrated Circuits”, *Quantum Information Processing* **3**, 163 (2004).
- [58] N. McLachlan, *Theory and Application of Mathieu Functions* (Clarendon Press, 1947), URL <https://books.google.de/books?id=ZGC4AAAAIAAJ>.
- [59] M. H. Devoret, A. Wallraff, and J. M. Martinis, *Superconducting Qubits: A Short Review* (2004).
- [60] J. N. L. Connor, T. Uzer, R. A. Marcus, and A. D. Smith, “Eigenvalues of the Schrödinger equation for a periodic potential with nonperiodic boundary conditions: A uniform semiclassical analysis”, *The Journal of Chemical Physics* **80**, 5095 (1984).
- [61] Hamel, “Georg Duffing, Ingenieur: Erzwungene Schwingungen bei veränderlicher Eigenfrequenz und ihre technische Bedeutung. Sammlung Vieweg. Heft 41/42, Braunschweig 1918. VI+134 S”, *ZAMM - Journal of Applied Mathematics and Mechanics / Zeitschrift für Angewandte Mathematik und Mechanik* **1**, 72 (1921).
- [62] F. Bloch, “Nuclear induction”, *Physica* **17**, 272 (1951).
- [63] E. M. Purcell, H. C. Torrey, and R. V. Pound, “Resonance Absorption by Nuclear Magnetic Moments in a Solid”, *Phys. Rev.* **69**, 37 (1946).
- [64] H. Haken and W. Hans Chr., *Atom- und Quantenphysik* (Springer, 1996).

- [65] U. Fano, “Description of States in Quantum Mechanics by Density Matrix and Operator Techniques”, *Rev. Mod. Phys.* **29**, 74 (1957).
- [66] W. Nolting, *Grundkurs Theoretische Physik 5/1: Quantenmechanik - Grundlagen* (Springer, 2013).
- [67] W. Pauli, “Zur Quantenmechanik des magnetischen Elektrons”, *Zeitschrift für Physik* **43**, 601 (1927).
- [68] K. Życzkowski and H.-J. Sommers, “Average fidelity between random quantum states”, *Phys. Rev. A* **71**, 032313 (2005).
- [69] D. I. Schuster, “Circuit Quantum Electrodynamics”, Ph.D. thesis, Yale University (2007).
- [70] D. M. Pozar, *Microwave engineering* (Fourth edition. Hoboken, NJ : Wiley, [2012] ©2012, [2012]), URL <https://search.library.wisc.edu/catalog/9910153599402121>.
- [71] W.-M. Zhang, D. H. Feng, and R. Gilmore, “Coherent states: Theory and some applications”, *Rev. Mod. Phys.* **62**, 867 (1990).
- [72] M. Basler, P. Tipler, G. Mosca, R. Dohmen, C. Heinisch, A. Schleitner, and M. Zillgitt, *Physik: für Wissenschaftler und Ingenieure* (Spektrum Akademischer Verlag, 2009), ISBN 9783827419453, URL <https://books.google.de/books?id=60HtPgAACAAJ>.
- [73] E. T. Jaynes and F. W. Cummings, “Comparison of quantum and semiclassical radiation theories with application to the beam maser”, *Proceedings of the IEEE* **51**, 89 (1963).
- [74] T. Liu, Y. Zhang, B.-Q. Guo, C.-S. Yu, and W.-N. Zhang, “Circuit QED: cross-Kerr effect induced by a superconducting qutrit without classical pulses”, *Quantum Information Processing*, **16**, 209 (2017).
- [75] S. E. Nigg, H. Paik, B. Vlastakis, G. Kirchmair, S. Shankar, L. Frunzio, M. H. Devoret, R. J. Schoelkopf, and S. M. Girvin, “Black-Box Superconducting Circuit Quantization”, *Phys. Rev. Lett.* **108**, 240502 (2012).
- [76] P. Tekely, “Malcolm H. Levitt. Spin dynamics: basics of nuclear magnetic resonance. John Wiley & Sons, Chichester, UK, 2001, 686 pp. Price £34.95. ISBN 0-471-48921-2”, *Magnetic Resonance in Chemistry* **40**, 800 (2002).
- [77] R. B. Bird, “The Feynman lectures on physics, Richard P. Feynman, Robert B. Leighton, and Matthew Sands, Addison-Wesley, Reading, Mass, Volume III”, *AICHE Journal* **10**, 794 (1965).
- [78] A. Wallraff, D. I. Schuster, A. Blais, J. M. Gambetta, J. Schreier, L. Frunzio, M. H. Devoret, S. M. Girvin, and R. J. Schoelkopf, “Sideband Transitions and Two-Tone Spectroscopy of a Superconducting Qubit Strongly Coupled to an On-Chip Cavity”, *Phys. Rev. Lett.* **99**, 050501 (2007).

- [79] R. Juarez Amaro, A. Zúñiga Segundo, and H. Moya-Cessa, “Several Ways to Solve the Jaynes-Cummings Model”, **9**, 299 (2015).
- [80] R. Schmied, “Quantum state tomography of a single qubit: comparison of methods”, *Journal of Modern Optics* **63**, 1744 (2016).
- [81] A. M. Brańczyk, D. H. Mahler, L. A. Rozema, A. Darabi, A. M. Steinberg, and D. F. V. James, “Self-calibrating quantum state tomography”, *New Journal of Physics* **14**, 085003 (2012).
- [82] K. Bffeynmananaszek, G. M. D’Ariano, M. G. A. Paris, and M. F. Sacchi, “Maximum-likelihood estimation of the density matrix”, *Phys. Rev. A* **61**, 010304 (1999).
- [83] A. A. Markov, “An Example of Statistical Investigation of the Text Eugene Onegin Concerning the Connection of Samples in Chains”, *Science in Context* **19**, 591â600 (2006).
- [84] K. Kraus, A. Böhm, J. D. Dollard, and W. H. Wootters, “States, Effects, and Operations Fundamental Notions of Quantum Theory”, **190** (1983).
- [85] A. Jamiołkowski, “Linear transformations which preserve trace and positive semidefiniteness of operators”, *Reports on Mathematical Physics* **3**, 275 (1972).
- [86] K. S. Ranade and M. Ali, “The Jamiołkowski Isomorphism and a Simplified Proof for the Correspondence Between Vectors Having Schmidt Number k and k -Positive Maps”, *Open Systems and Information Dynamics* **14**, 371 (2007).
- [87] A. Gilchrist, N. K. Langford, and M. A. Nielsen, “Distance measures to compare real and ideal quantum processes”, *Phys. Rev. A* **71**, 062310 (2005).
- [88] M. Howard, J. Twamley, C. Wittmann, T. Gaebel, F. Jelezko, and J. Wrachtrup, “Quantum process tomography and Linblad estimation of a solid-state qubit”, *New Journal of Physics* **8**, 33 (2006).
- [89] F. Deppe, “Superconducting flux quantum circuits: characterization, quantum coherence, and controlled symmetry breaking”, Ph.D. thesis, TU München (2009).
- [90] M. Neeley, M. Ansmann, R. C. Bialczak, M. Hofheinz, N. Katz, E. Lucero, A. O’Connell, H. Wang, A. N. Cleland, and J. M. Martinis, “Process tomography of quantum memory in a Josephson-phase qubit coupled to a two-level state”, *Nature Physics* **4**, 523 EP (2008).
- [91] R. C. Bialczak, M. Ansmann, M. Hofheinz, E. Lucero, M. Neeley, A. D. O’Connell, D. Sank, H. Wang, J. Wenner, M. Steffen, A. N. Cleland, and J. M. Martinis, “Quantum process tomography of a universal entangling gate implemented with Josephson phase qubits”, *Nature Physics* **6**, 409 EP (2010).
- [92] J. L. O’Brien, G. J. Pryde, A. Gilchrist, D. F. V. James, N. K. Langford, T. C. Ralph, and A. G. White, “Quantum Process Tomography of a Controlled-NOT Gate”, *Phys. Rev. Lett.* **93**, 080502 (2004).

- [93] M. Ježek, J. Fiurášek, and Z. c. v. Hradil, “Quantum inference of states and processes”, *Phys. Rev. A* **68**, 012305 (2003).
- [94] G. Gutoski and N. Johnston, “Process tomography for unitary quantum channels”, *Journal of Mathematical Physics* **55**, 032201 (2014).
- [95] G. Lindblad, “On the generators of quantum dynamical semigroups”, *Comm. Math. Phys.* **48**, 119 (1976).
- [96] N. Boulant, T. F. Havel, M. A. Pravia, and D. G. Cory, “Robust method for estimating the Lindblad operators of a dissipative quantum process from measurements of the density operator at multiple time points”, *Phys. Rev. A* **67**, 042322 (2003).
- [97] A. Uhlmann, “The ”transition probability” in the state space of a *-algebra”, *Reports on Mathematical Physics* **9**, 273 (1976).
- [98] A. Y. Kitaev, “Quantum computations: algorithms and error correction”, *Russian Mathematical Surveys* **52**, 1191 (1997).
- [99] D. H. Mahler, L. A. Rozema, A. Darabi, C. Ferrie, R. Blume-Kohout, and A. M. Steinberg, “Adaptive Quantum State Tomography Improves Accuracy Quadratically”, *Phys. Rev. Lett.* **111**, 183601 (2013).
- [100] D. Bures, “An Extension of Kakutani’s Theorem on Infinite Product Measures to the Tensor Product of Semifinite w^* -Algebras”, **135**, 199 (1969).
- [101] A. Ben-Aroya and A. Ta-Shma, “On the Complexity of Approximating the Diamond Norm”, *Quantum Info. Comput.* **10**, 77 (2010).
- [102] K. Z. Sommers and Hans-Jürgen, “Induced measures in the space of mixed quantum states”, *Journal of Physics A: Mathematical and General* **34**, 7111 (2001).
- [103] H.-J. S. Zyczkowski and Karol, “Statistical properties of random density matrices”, *Journal of Physics A: Mathematical and General* **37**, 8457 (2004).
- [104] M. J. W. Hall, “Random quantum correlations and density operator distributions”, *Physics Letters A* **242**, 123 (1998).
- [105] E. M. Purcell, in *Physical Review* (1946), vol. 69, p. 681, URL http://prola.aps.org/pdf/PR/v69/i11-12/p674_2.
- [106] D. F. Walls and G. J. Milburn, “Effect of dissipation on quantum coherence”, *Phys. Rev. A* **31**, 2403 (1985).
- [107] F. Marquardt and A. Püttmann, *Introduction to dissipation and decoherence in quantum systems* (2008).
- [108] E. Xie, “A scalable 3D quantum memory”, Ph.D. thesis, TU München (2018).

- [109] J. Müller, “3D Cavities for Circuit Quantum Electrodynamics”, Bachelor’s Thesis, TU München (2014).
- [110] C. Enss and S. Hunklinger, *Low-Temperature Physics*, SpringerLink: Springer e-Books (Springer Berlin Heidelberg, 2005), ISBN 9783540266198, URL <https://books.google.de/books?id=ufM7sPMTGdAC>.
- [111] J. Götz, “The Interplay of Superconducting Quantum Circuits and Propagating Microwave States”, Ph.D. thesis, TU München (2017).
- [112] R. Dorf, *The Electrical Engineering Handbook, Second Edition*, Electrical Engineering Handbook (Taylor & Francis, 1997), ISBN 9781420049763, URL <https://books.google.de/books?id=qP7HvuakLgEC>.
- [113] M. Reed, *Entanglement and Quantum Error Correction with Superconducting Qubits* (Yale University, 2013), ISBN 9781304084866, URL <https://books.google.de/books?id=7mORBQAAQBAJ>.
- [114] S. Gantner, “Vector Modulation of Microwaves for Circuit QED Experiments”, Bachelor’s Thesis, TU München (2013).
- [115] I. Bronštejn, H. Mühlig, K. Semendjajew, and G. Musiol, *Taschenbuch der Mathematik (Bronstein)*, Edition Harri Deutsch (Europa Lehrmittel Verlag, 2016), ISBN 9783808557891, URL <https://books.google.de/books?id=Kh9qjwEACAAJ>.
- [116] W. Zinth and U. Zinth, *Optik: Lichtstrahlen - Wellen - Photonen* (Oldenbourg Wissenschaftsverlag, 2013), ISBN 9783486721362, URL <https://books.google.de/books?id=FDb179jp31QC>.
- [117] M. Hiebel, *Fundamentals of Vector Network Analysis* (Rohde & Schwarz, 2007), ISBN 9783939837060, URL <https://books.google.de/books?id=jYG2PQAACAAJ>.
- [118] J. G. Gross, F. Deppe, P. Eder, M. Fischer, M. Müting, J. P. Martínez, S. Pogorzalek, F. Wulschner, E. Xie, K. G. Fedorov, A. Marx, and R., “Second-order decoherence mechanisms of a transmon qubit probed with thermal microwave states”, *Quantum Science and Technology* **2**, 025002 (2017).
- [119] C. Müller, J. Lisenfeld, A. Shnirman, and S. Poletto, “Interacting two-level defects as sources of fluctuating high-frequency noise in superconducting circuits”, *Phys. Rev. B* **92**, 035442 (2015).
- [120] N. F. Ramsey, “A Molecular Beam Resonance Method with Separated Oscillating Fields”, *Phys. Rev.* **78**, 695 (1950).
- [121] P. R. Bevington, D. K. Robinson, J. M. Blair, A. J. Mallinckrodt, and S. McKay, “Data Reduction and Error Analysis for the Physical Sciences”, *Computers in Physics* **7**, 415 (1993).

- [122] U. Schollwoeck, *The density-matrix renormalization group in the age of matrix product states*, vol. 326 of *Annals of Physics - ANN PHYS N Y* (2010).
- [123] W. Nolting, *Grundkurs Theoretische Physik 6: Statistische Physik*, Springer-Lehrbuch (Springer Berlin Heidelberg, 2006), ISBN 9783540350842, URL <https://books.google.de/books?id=oqAfBAAAQBAJ>.
- [124] W. Demtröder, *Experimentalphysik 1: Mechanik und Wärme*, Springer-Lehrbuch (Springer Berlin Heidelberg, 2012), ISBN 9783642254666, URL <https://books.google.de/books?id=nUUeBAAAQBAJ>.
- [125] W. Demtröder, *Technisches Taschenbuch* (Schaeffler Technologies AG Co. KG, 2017), ISBN 9783642254666.
- [126] J. Tatum, “Stellar Atmospheres. Chapter2: Blackbody Radiation”, (2018), URL <http://orca.phys.uvic.ca/~tatum/stellatm.html>.
- [127] W. Wien, *Eine neue Beziehung der Strahlung schwarzer Körper zum zweiten Hauptsatz der Wärmetheorie*, Berl. Ber. (1978).
- [128] L. B. Valdes, “Resistivity Measurements on Germanium for Transistors”, *Proceedings of the IRE* **42**, 420 (1954).
- [129] F. Motzoi and F. K. Wilhelm, “Improving frequency selection of driven pulses using derivative-based transition suppression”, *Phys. Rev. A* **88**, 062318 (2013).
- [130] J. M. Gambetta, F. Motzoi, S. T. Merkel, and F. K. Wilhelm, “Analytic control methods for high-fidelity unitary operations in a weakly nonlinear oscillator”, *Phys. Rev. A* **83**, 012308 (2011).
- [131] F. Motzoi, J. M. Gambetta, P. Rebentrost, and F. K. Wilhelm, “Simple Pulses for Elimination of Leakage in Weakly Nonlinear Qubits”, *Phys. Rev. Lett.* **103**, 110501 (2009).
- [132] Q. Xie, H. Zhong, M. T. Batchelor, and C. Lee, “The quantum Rabi model: solution and dynamics”, *Journal of Physics A: Mathematical and Theoretical* **50**, 113001 (2017).
- [133] J. B. Altepeter, D. Branning, E. Jeffrey, T. C. Wei, P. G. Kwiat, R. T. Thew, J. L. O’Brien, M. A. Nielsen, and A. G. White, “Ancilla-Assisted Quantum Process Tomography”, *Physical Review Letters* **90**, 193601 (2003).
- [134] M. L. Hartmann and M. J., “Bose-Hubbard dynamics of polaritons in a chain of circuit quantum electrodynamics cavities”, *New Journal of Physics* **12**, 093031 (2010).
- [135] (2018), URL <https://www.mathworks.com/help/matlab/ref/fminsearch.html>.
- [136] (2018), URL <https://www.mathworks.com/help/optim/ug/fmincon.html>.
- [137] H. R. Schwarz and N. Köckler, *Numerische Mathematik*, Lehrbuch Mathematik (Teubner, 2004), ISBN 9783519429609, URL <https://books.google.de/books?id=jKEdlfyFZ5AC>.

- [138] T. F. Havel, “Robust procedures for converting among Lindblad, Kraus and matrix representations of quantum dynamical semigroups”, *Journal of Mathematical Physics* **44**, 534 (2003).
- [139] M. Planck, “Ueber das Gesetz der Energieverteilung im Normalspectrum”, *Annalen der Physik* **309**, 553 (1901).
- [140] (2018), URL <https://www.mathworks.com/help/matlab/ref/ode45.html>.
- [141] J. R. Dormand and P. J. Prince, “A family of embedded Runge-Kutta formulae”, *Journal of Computational and Applied Mathematics* **6**, 19 (1980).

Acknowledgement

Within the last year, I got to know applied quantum information processing as a fascinating and interdisciplinary field of modern physics, especially due to the combination of practical lab work and complex theory. I am very glad that I got the opportunity to write my master's thesis within this field at the WMI, a venerable institute for low temperature research. This would not have been possible without the support of many people, and I want to thank them all very much.

I want to thank Prof. Dr. Rudolf Gross, since he gave me the opportunity to join the group for superconducting quantum circuits at the WMI. His scientific commitment and reputation, as well as his book about solid state physics, which helped me a lot when I was an undergraduate student, are significant reasons why I wished to work at the WMI.

I thank Edwar Xie for his support as my direct supervisor and my contact person regarding physical problems as well as problems in the lab. I know that it takes a lot of time to introduce a new master student to serious scientific work, and I admire his patience with me. Even during his vacation, he gave me valuable technical and physical advice. Furthermore, I want to thank him very much for giving helpful and constructive feedback for my work as well as for multiple abstracts and test talks. This thesis would not have been possible without him.

I thank Dr. Frank Deppe for his advice, his support and his mentoring. He was my first direct contact of the qubit group at the WMI, and he convinced me that joining his group is the right choice. He helped me a lot with my lab issues, especially when the cryostat was down, and I admire his practical skills in the lab. His office door was always open when I had problems and issues, and I thank him for many helpful discussions about physics. I furthermore thank him for taking me to the DPG conference in Berlin with his car and for his helpful and constructive feedback, including my work in general, but also for abstracts and test talks.

I thank Dr. Kirill Fedorov for his valuable physical advice and for discussing technical and physical problems, especially during lunch time at the Mensa, and I am very unhappy that I was not able to join more often. His lecture about applied superconductivity inspired me and is one of the reasons why I wanted to become a member of the WMI qubit group. Furthermore, I want to thank him for his helpful and constructive feedback for my test talks. I am looking very forward to our collaboration when I start working on my PhD in November 2018.

I thank Dr. Achim Marx for his technical support in the Circus lab. He especially helped

me multiple times with my cryostat problems, and I am grateful since this sometimes took more time than expected. I want to thank him for his great job regarding the construction works, especially concerning the air conditioner in the Circus lab and the elevator. I am furthermore thankful for his helpful and constructive feedback regarding my work and my test talks.

I thank Dr. Matthias Althammer for motivating me to write my thesis at the WMI, especially since he offered me a job at the WMI where I was able to program an electronic setup which helped me to improve my LabView skills.

I thank Dr. Hans Hübl for administratively introducing me to the WMI. His lectures about superconductivity and low temperature physics substantiated my wish to join the WMI.

Thanks to the PhD students, they always helped me when I had questions. I especially want to thank Stefan Pogorzalek, since he invested time to discuss physical problems as well as issues regarding LabView programming. Additionally, I want to thank the master students, especially my office colleagues Birte Cöster, Luis Flacke and Ulrike Zweck.

I thank Jan Naundorf, Peter Binkert and Harald Schwaiger from the Heliumhalle for their support and the weekly craning of the liquid helium and the liquid nitrogen cans to the basement when the elevator was broken. I especially thank Jan for the introduction to the proper handling of the liquid helium cans. I want to thank Dr. Matthias Opel and Michael Fischer for organizing my cans when I was not available. Furthermore, I want to thank Sebastian Kammerer for his help in the lab, especially for the exchange of the compressed helium bottles. He was always able to give valuable answers to my technical questions. I thank Dieter Guratzsch, Dr. Matthias Opel and Daniel Schwienbacher for their IT support.

I thank Maria and Sybilla for keeping the lab and the office clean.

Furthermore, I want to thank Emel Dönertas and Ludwig Ossiander for their administrative work, especially regarding organizational issues for conferences and for my future employment at the WMI.

I want to thank our collaboration partners Dr. Shai Machnes and Nicolas Wittler.

I thank my parents Uwe and Petra and my grandparents Helga and Adolf for their unlimited support regarding my future plans. Without them, I would never have had the possibility to study physics in Munich. I am very thankful, not just regarding their support during my studies, but also for making me proud of what I am doing. An additional thanks goes to my sister Rebekka, who always gave me mental support. Furthermore, I want to thank my friends for their support, also for the understanding that it was not always possible to spend time with them since I had to work on my thesis.

Finally, I thank my girlfriend Eva-Maria, who always kept my options open. She was always able to motivate me and cheer me up when I was down or when things did not work as expected. Without her support during the years of my studies, I would not be where I am now. I am very glad to have her on my side!

Eidesstattliche Erklärung

Hiermit erkläre ich, dass ich die vorliegende Arbeit eigenständig und ohne fremde Hilfe angefertigt habe. Textpassagen, die wörtlich oder dem Sinn nach auf Publikationen oder Vorträgen anderer Autoren beruhen, sind als solche gekennzeichnet.

Michael Renger

Garching, den 16. Oktober 2018